CHALMERS

MASTER THESIS PROJECT

DUAL POLARIZED DIELECTRIC RESONATOR ANTENNAS

UBAID MAHMOOD KHAN
ubaidexquisite@gmail.com

MLADEN MILUTINOVIC
f04mm@student.lth.se

Supervisors:

Anders Derneryd, Ericsson anders.derneryd@ericsson.com
Patrik Persson, Ericsson patrik.c.persson@ericsson.com
Ahmed Kishk, Chalmers University ahmed@olemiss.edu

Examiners:

Per-Simon Kildal, Chalmers University per-simon.kildal@chalmers.se

Chalmers University of Technology
Department of Computer Science and Engineering
Göteborg, Sweden, June 2010

Dual Polarized Dielectric Resonator Antenna

Ubaid Mahmood Khan and Mladen Milutinovic

Examiner: Prof. Per-Simon Kildal

Chalmers University of Technology
Department of Signal and System
SE-412 96 Göteborg
Sweden
Telephone + 46 (0)31-772 17 18

Department of Signal and System

Göteborg, Sweden, October 2010

Abstract

Dielectric resonators have been widely used as narrowband shielded circuit components. The dielectric resonator antenna is an employment of the idea of using an unshielded dielectric structure in order to extract the radiation of electric fields. Dielectric materials can have low dielectric loss and the absence of metallic surfaces also reduces conduction losses. A dielectric resonator antenna can have efficiencies above *95%* for several hundred megahertz. The versatility in choice of shape, relative permittivity and size enables a whole spectrum of operating frequency ranges (*1GHz-40GHz*), sizes, radiation patterns and bandwidths. The far field radiation pattern is a characteristic of the resonating modes. In this project the investigation of dielectric resonator antennas was quantitatively realized by the design and evaluation of one omni-directional dual polarized dielectric resonator antenna with operating frequency range *2.4GHz* to *2.7GHz* and one dual polarized broadside antenna element in the frequency range *3.8GHz* to *4.2GHz*. For an omni-directional radiation pattern, transverse modes with rotational symmetry are preferred. For a broadside radiation pattern, a hybrid mode is suitable. The modes can be excited by feeding from microstrip lines and coaxial probes. The location of the excitation determines what mode is excited. The resonant frequency is controlled by size, shape and permittivity. Dual polarization is achieved by exciting two orthogonal modes simultaneously in the resonator. The cross coupling between the feeding networks and the matching of these becomes a crucial step in the design of a dielectric resonator antenna. Several broadside antenna elements have been arranged in a linear array for increased directivity.

Acknowledgement

This project was initiated and led by *Anders Derneryd and Patrik Persson at the antenna department of Ericsson Research* at Lindholmen, Gothenburg. We owe much gratitude to these two men who have wholeheartedly been active in providing large resources, supervision, advising and encouragement.

Very special thanks also go to Professor Ahmed A. Kishk, for his supervision regarding theory and design of the antennas. It has been a delight and an honor to work with one of the pioneers and leaders of the research in this field, who is also a very good educationalist.

We are thankful to Professor Per-Simon Kildal for taking time out from his busy schedule to evaluate the work as an examiner for the master thesis work.

Furthermore, with the design ready, none of the evaluations of our antennas would have been possible without the sample sheets of the antenna material that we got for free from Rogers Corporation. Involved in the manufacturing were also Håkan Svensson and his crew at MAX-LAB of Lund University who very precisely shaped the antenna elements in record time. In this context a thanks also goes to Professor Ove Edfors and his colleague Martin Andersson at Lund University.

We also want to thank Professor Jian Yang for giving us access and help to use the antenna measurement range at Chalmers University. Mr. Lars Torstensson from Ericsson also deserves the biggest thanks for sacrificing many hours on our measurements.

Finally, we like to thank the pillars that kept us believing in ourselves and supported us unconditionally during the past six months, *our families*.

Table of Contents

List of Figures

List of Symbols

β	propagation constant
ε_r	dielectric constant
μ	permeability
μ_o	Permeability of free space
λ_o	wavelength of free space
ω	radian frequency
$\Delta\omega$	bandwidth
AR	axial ratio
BW	bandwidth
c	speed of light
DRA	dielectric resonator antenna
e_{r}	radiation efficiency
f	frequency
f_o	resonant frequency
G	gain
H	magnetic field intensity
$H_n^m(x)$	nth order Hankel function of the mth kind
HE	hybrid mode (E_z field dominant)
$J_n(x)$	nth order Basel function of first kind
k	wave number
k_o	wave number in free space
Q	quality factor
TE	transverse electric
TM	transverse magnetic
VSWR	voltage standing wave ratio
Z	impedance
Z_o	characteristic impedance

CHAPTER 1

INTROUDUCTION

The use of mobile communication is increasing, more and more applications for communication are being launched commercially. This development has put more demand for compact size and low energy consumption for the equipment. Base stations powered by solar cells are a reality, for example. Low loss in the antenna is also crucial for the operation of such a network. High energy efficiency is a key for obtaining higher signal strengths and increasing the capacity of existing networks. Today's patch antennas have compact size but drawbacks such as conduction losses due to the skin effect and narrow operating frequency bandwidth.

In the last two decades, much research has been done on the dielectric resonator antenna (DRA) which also has regained a wider interest in recent years. Its small volume and low profile, together with its lack of metallic surfaces makes it interesting for low conduction losses. The fact that it can be designed for high bandwidths makes it an interesting alternative. The dielectric resonator is widely used in microwave circuits for filters and oscillators but where its resonant modes are confined and narrowband. Now the ambition is to see what this device can achieve as an antenna element.

This project was initiated by Ericsson Research in order to investigate the possibilities with the dielectric resonator antenna in a way suitable for a thesis work and with the ambition to evaluate a physical antenna by analysis and measurements.

The concrete goals are to design two antennas with dual polarization. One should have an omni-directional radiation pattern suitable for indoor use, e.g. at a ceiling-mounted indoor access point for wireless networks. The other antenna element should have broadside beam and port isolation better than *15dB*. The broadside antenna should be designed in a linear array with four of the latter elements for operation between *3.8GHz* and *4.2GHz* and the omni-directional antenna should operate at frequencies between *2.4GHz* and *2.7GHz*. The return loss should be more than *15dB* and the required efficiency is at least *90%*. This should be achieved by the excitation of proper modes and the use of a proper material and shape, adjusted for the frequencies of interest.

Since this is a study of the possibilities and limitations with dielectric resonator antennas, and is only intended as a guideline, the main objective is a proof of concept and the evaluation of a manufactured physical antenna is highly desired.

The measurements are to be of both scattering parameters and radiation pattern. The project starts by a review of the literature on the subject and experiments in the software, which is Ansoft HFSS version 12.1.

All work is being performed at the antenna department of Ericsson Research (EAB/TUA/A) at Lindholmen in Gothenburg, Sweden. All resources, software and hardware as well as supervising is provided by Ericsson. The technical knowledge for questions regarding theory and design is given by Prof. Ahmed A. Kishk, a guest professor at Chalmers University during the spring of 2010.

In the Background section, a review of the research and knowledge is made. First a historical overview of the birth and development of DRA research is given and the pioneers are mentioned. Both theoretical mathematical descriptions with focus on describing resonances are given as well as numerous examples of different antennas, modes and excitation techniques. In this part, a short general discussion about the benefits of the DRA takes place.

In the Method part, a chronological description of the experimenting, testing and verification of different properties from the literature are given. These are followed by a thorough description of the design process, dealing with the problems and obstacles on the way. Important decisions are explained and motivated. The outcome, i.e. the manufactured antenna is presented here.

The third part consists of Results, conclusion (Summary) and Discussion. In Results, the measurements performed are presented. In Summary, the results are evaluated and compared with theory. Suggestions for future investigation on the subject are made here.

CHAPTER 2

OVERVIEW

2.1 History of Dielectric Resonator Antennas

Resonance cavities of simple shapes with a metallic coating have been analyzed for a long time as a special case of waveguides. There exist explicit expressions for calculating the resonant frequencies and electromagnetic fields in a resonance cavity [1]. In 1939, Richtmeyer at Stanford University showed that dielectric objects shaped like toroids could be used as microwave resonators [2]. This is where the term dielectric resonator first appeared [3]. It was not until a practical resonator was reported in the early 1960s by Okaya and Barash at Columbia University that the interest regained [3]. This first ever dielectric resonator was made from a single crystal TiO_2. The first extensive theoretical and experimental evaluation of the dielectric resonator was carried out by Cohn with colleagues at Rantec Corporation in the mid-1960s [3]. A breakthrough came in 1971 when Masse et al presented the first temperature-stable low loss ceramic of barium tetratitanate [4]. A report from 1975 by van Bladel from the University of Gent, Belgium showed a detailed analysis of various modes in the dielectric resonator of arbitrary shape [5]. The usage of narrow-band dielectric resonators and resonance cavities with high Q-factors exploded in microwave applications as oscillators and filters, especially as low-loss dielectric materials were developed. In these circuits, oscillators are made of high-permittivity materials and are usually shielded to avoid radiation and maintain high Q-factors.

The idea of using dielectric resonators as antennas first came from Long as a way of creating a microstrip antenna by replacing the leaky conducting patch and substrate by a dielectric resonator in order to take advantage of the leakage from the resonator [6]. This investigation took place at the US Army Harry Diamond Laboratories during the summer of 1981. The theory was based on perfectly conducting magnetic wall boundary approximations. The investigated shape was a cylinder. The first results showed that it was possible to achieve a radiation pattern similar to that of an electric dipole parallel to the ground plane, originating from the HE_{11} mode. Also, the impedance bandwidth was better compared to the microstrip antenna. A sketch of this single polarized antenna and feeding is shown in Figure 1. The following autumn Long, together with McAllister and Shen systematically investigated different shapes and sizes, as well as materials, at the University of Houston, which resulted in the first publications [7-9] starting from 1983 and the term dielectric resonator antenna was used for the first time. In these papers the feeding was made by coaxial lines with probes extending into the resonators through drilled holes.

In the second half of the 1980s several publications were made by different research groups, the first from outside of Houston being a paper by Haneishi et al at the Saitama University of Japan

[10]. Pioneers in the area were three research groups situated in the University of Mississippi, the Communications Research Center in Ottawa and the City University of Hong Kong. The first group contained among others Kishk, Junker, Glisson and Kajfez. The second group contained Petosa, Ittpiboon, Mongia and Barthia among others [11] and the third group mentioned was led by Luk and Leung [11].

In the mid-1990s more emphasis was laid on dielectric resonator antenna arrays, both linear and planar with as many as *300* elements with beam control. Also ferrite resonator antennas came to day during this period, together with antennas operating in the millimeter frequency band and wideband antennas [11]. Today, the interest from the industry has grown, much thanks to a wish for wideband techniques and efficiency improvement.

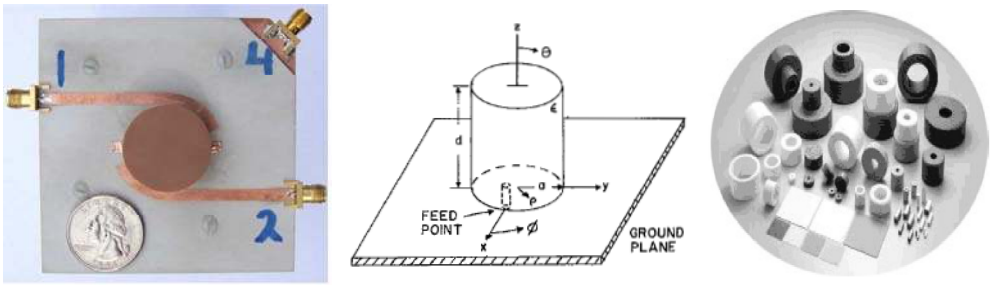

Figure 1: A dielectric resonator antenna (left) [12]; Illustration of the first dielectric resonator antenna (center); Sample of different shapes of dielectric resonator antennas (right) [3].

2.2 Characteristics of the Dielectric Resonator Antennas

The dielectric resonator has been studied extensively in recent years for different applications from low frequencies to high frequencies. The dielectric resonator antenna has a high flexibility and versatility in adopting a shape over a wide frequency range, which allows the designer to achieve the desired requirement. Some of the major advantages or characteristics of the dielectric resonator antenna are as follows:

i. The size of the dielectric resonator antenna is proportional to $\lambda_o/{\varepsilon_r}^{1/2}$, where λ_o is the free space wavelength of the resonant frequency and ε_r is the dielectric constant of the dielectric resonator. This means that the size of the dielectric resonator antenna can be reduced by just increasing the dielectric constant [3].
ii. The dielectric constant ε_r can be from a range of below 3 up to 100, which allows for a great deal of flexibility when controlling the size and bandwidth [11].
iii. A millimeter-wave frequency operation can be achieved by choosing a low-loss characteristic dielectric material due to an absence of surface waves and minimal conductor losses associated with the dielectric resonator antenna. At these frequencies high radiation efficiency can be achieved [11].

iv. Many modes can be excited within the dielectric resonator antenna element depending on the shape of the resonator. Different modes give different radiation patterns for various coverage requirements [3].
v. The radiation *Q*-factor of the above mentioned modes depends on the aspect ratio; the aspect ratio is an important parameter in designing a dielectric resonator antenna because it gives one more degree of freedom for the design [11].
vi. Different methods can be used to excite the dielectric resonator antenna (slot, probe, coplanar, microstrip, waveguide, dielectric image guide, etcetera.) which make them easy to integrate with the existing technologies [3].
vii. Dielectric resonator antennas are designed to operate over a wide frequency range of *1.3* to *40GHz* [11].
viii. Dielectric resonator antennas have high dielectric strength which makes them capable to handle high power. This also helps them to work in a wide temperature range due to the temperature-stable ceramic materials [3].
ix. The dielectric resonator antenna has much wider impedance bandwidth compared to the microstrip antenna. It is because the dielectric resonator antenna radiates through the whole antenna surface except for the ground whereas the microstrip antenna radiates only through the narrow slots [3].

The problem with dielectric resonator antennas is typically that ceramic materials which are machined to shape from a large block are used. To feed the antenna excitations from e.g. probes, the antenna needs to be drilled since it is bounded to a ground plane or a substrate. The fabrication of dielectric resonator antennas is more complex and more costly compared to printed circuit antennas, especially for array applications. Maybe for high-volume of production the cost reduces but the economic scale is not that important. There are applications where performance is more important than cost and the dielectric resonator can antenna provide the solution.

2.3 Materials for dielectric resonators

Depending on the application of the dielectric resonator, different requirements are specified for the material to be used. The dielectric properties depend on the material, crystal structure, porosity and imperfections in the crystal lattice as well as on the preparation conditions. Dielectric resonators generally consist of a puck-formed cylinder of ceramic material of high permittivity and low dissipation factor. Traditional passive devices have been desired to have a high *Q*-factor (up to *20,000* between *2* and *20GHz* [3]), high permittivity and near zero temperature coefficients for the resonant frequency which has been difficult to achieve simultaneously. The low-permittivity ceramics have so far been used for millimeter-wave applications and also as substrates for microwave integrated circuits. Ceramics with permittivity in the range between 25 and 50 have been used for satellite communication and in cell phone base stations. High permittivity materials are used in mobile telephones, were the compact size sets narrow limits. In all the mentioned cases the use has been for circuit components.

There are about *2300* low-loss dielectric materials reported in the literature [13]. About *60%* of the dielectric resonator materials are based on alkaline earth metals such as *Ba*, *Mg*, *Sr* and *Ca*. About *46%* of the materials are titanates. Rare earth materials appear in *40%* of the cases.

2.3.1 Losses and quality factor

The total dielectric loss is the sum of intrinsic and extrinsic losses. Intrinsic dielectric losses are the losses in the perfect crystals which depend on the crystal structure. They can be described as interactions between phonons and an electric field. The electric field changes the equilibrium of the phonon systems and the subsequent relaxation is associated with energy dissipation. As a result the relaxation dissipates heat energy and the material gets heated. The intrinsic losses depend on the crystal symmetry, electric field frequency and temperature. The intrinsic losses fix the lower limit of losses in crystals free from defects. Extrinsic losses are due to imperfections in the crystal lattice such as impurities, dopant atoms, vacancies etcetera. Crystals from different symmetry groups have different temperature and frequency dependence for the dielectric loss. A measure of the dielectric loss is given by the dielectric loss tangent, defined as

$$tan\,\delta = \varepsilon''_r/\varepsilon'_r \tag{2.1}$$

where $\varepsilon_r = \varepsilon_r' - j\varepsilon_r''$ is the complex frequency dependent permittivity. For lossless materials, ε_r' is zero [14]. The inverse of the dielectric loss tangent is sometimes referred to as the quality factor by manufacturers [13]. The other measure of energy dissipation, namely the *Q*-factor, gives all the energy losses, not only the material losses.

The *Q*-factor is defined by

$$Q = 2\pi \left(\frac{E_{\max stored}}{E_{avg\ diss}}\right) \tag{2.2}$$

where $E_{\max\ stored}$ is the maximum energy stored in one cycle and $E_{\text{avg }diss}$ is the average energy dissipated during one cycle. The total loss in a dielectric resonator is the sum of dielectric, conduction, radiation and external losses which, in terms of Q, can be written as:

$$\frac{1}{Q_L} = \frac{1}{Q_d} + \frac{1}{Q_c} + \frac{1}{Q_r} + \frac{1}{Q_{cpi}} \tag{2.3}$$

where Q_L is the loaded *Q*-factor, taking into account coupling effects that arise when an electric field is induced in the dielectric resonator. The field lines induce currents on objects in their way which is represented by the term $\frac{1}{\mathrm{Q_{cpi}}}$. The dielectric loss, the conduction and the radiation *Q*-factor are given by $Q_d = \frac{\omega_o W}{P_d}$, $Q_c = \frac{\omega_o W}{P_c}$ and $Q_r = \frac{\omega_o W}{P_r}$. Here, W is the total electric energy stored in the resonator and $P_{d,}\, P_c$ and P_r are the dissipated power in the dielectric, conduction and radiation, respectively. The metallic coating around the dielectric resonator is removed so that the

fields can leave the object. The radiation is to be maximized and the lack of metallic surfaces implies that no ohmic losses appear. This is one of the main advantages of the dielectric resonator antenna.

Q_L is experimentally determined from the shape of the resonance peak in the reflection versus frequency diagram. The curve is drawn for a resonator coupled with an external circuit. The transmitted signal amplitude peaks at the resonant frequency. The 3dB-bandwidth is the frequency bandwidth at half power from the peak. The loaded *Q*-factor, Q_L is the resonant frequency divided by the *3dB*-bandwidth.

The quality factor of the microwave frequency materials is very sensitive to the structure of the material and the processing. The dielectric loss, which determines Q_d, can vary from one sample to another due to variations in the intrinsic crystal structure, density, concentration of impurities etcetera.

2.3.2 Barium-titanates

The barium-titanates $BaO\text{-}TiO_2$ have been used for a long time in the ceramic capacitor industry. The *Ti*-rich compounds are few but exhibit good temperature compensation and high relative permittivity between *25* and *40*. It was Masse et al [4] who first pointed out that $BaTi_4O_9$ is suitable for dielectric resonator applications at microwave frequencies. Doping with *Mn*, *Sn* and *Pb* lowers the *Q*-factor while doping with *Zr*, *Sr* and *Ca* raises the *Q*-factor and depending on the doping the relative permittivity is between *33* and *37*.

2.3.3 Zirconium – titanates

For the microwave frequency region, $Zr_xTi_ySn_zO_4$ have been reported as temperature-stable low loss dielectric materials [13]. The composition $Zr_{0.8}TiSn_{0.2}O_4$ gives the best microwave dielectric properties because of low porosity and its property as a highly homogeneous material.

2.3.4 Pseudo-tungsten bronze-type

The materials in this category have high ε_r , low loss and are often used in the cell-phone industry. The ceramics $Ba_{6-3x}Ln_{8+2x}Ti_{18}O_{54}$ with *Ln* substituted by *Nd*, *Sm*, or *Eu* have high quality factors up to *14,000*. With *Ln* replaced by *La*, the highest ε_r can be obtained.

2.3.5 Low Temperature Cofired Ceramics

Low temperature cofired ceramics (LTCC) are tapes of flexible ceramic glass. In this technology, several thin layers of low-permittivity ceramic composites and conductors are combined. A

variety of components can be made from this material, including microstrips, striplines, antennas, filters, resonators, capacitors, inductors and phase shifters making possible a design on a substrate of these components. The latest materials from this family show a low dielectric loss and a temperature compensated relative permittivity. The low thermal expansion, high mechanical strength and high thermal conductivity of these materials make them interesting for low-loss, high-frequency circuits for high-speed data communication. The main drawback of these materials is that they are complicated and sensitive to manufacture. The permittivity is in the range *4* to *100*. Materials of low relative permittivity with $\varepsilon_r=4$ to *12* are used as substrate layers while materials with higher permittivity are used mostly as capacitor layers.

2.3.6 Alumina

Alumina materials have a relative permittivity around *10*, relatively high thermal conductivity and low dielectric loss and are frequently used as packaging material for ceramics. The dielectric loss is highly variable and has oscillations within several orders of magnitude. Since the material is in powder form, the powder purity is very important. In polycrystalline alumina, the quality factor decreases rapidly by the presence of alkali ions and atoms from other metals, such as *Fe*. A small amount of TiO_2 can improve the quality factor considerably [13]. The purity does not have as high an impact on the dielectric loss tangent, which is more dependent on the sintering temperature and the humidity in the powder. The dryer the powder, the lower the dielectric loss tangent will be.

2.3.7 Titania

Titanium dioxide crystallizes in three forms. One of them is rutile which has properties suitable for microwave applications, and this form was also used by Okaya and Barash in their discovery [13] as mentioned in the History section. By hot pressing the rutile in a graphite die, a high quality factor ($Q>10,000$) can be obtained. The dielectric loss increases with the percentage of porosity of TiO_2 rutile. The tan δ of TiO_2 also increases with temperature and rises from *0 to* $5\cdot10^{-4}$ between *0* and *100K*, whereafter the increase is slower and reaches $6\cdot10^{-4}$ at room temperature. The dependence can be minimized by doping with AlO_3.

2.3.8 Cerium Oxide

Cerium oxide (CeO_2) has a good lattice match with silicon, high chemical stability and high relative permittivity and is suited as an insulating material. Both Q and ε_r decrease when doping with $CaCO_3$. Depending on the concentration of doping (with either $CaCO_3$ or $CaTiO_3$) the relative permittivity is between *24* and *29*.

2.3.9 Silicates

For substrates, materials with low dielectric loss and low permittivity are sought after. The silicates, with their covalent bindings keep their atoms relatively tight bonded and cannot vibrate or move around. This leads to low dielectric loss. The low dielectric polarizer of silicon and the strong bonds also lead to low ε_r in silicates.

Silicates have been used for dielectric waveguides but have turned out to be good as substrates at millimeter wave frequencies. One useful silicate-based dielectric ceramic is Cordierite ($2MgO$-$2Al_2O_3$- $CaCO_3$- $5SiO_2$). The relative permittivities of these materials are in the interval between *6* and *11*.

2.3.10 Bismuth based low-firing ceramics

For cylindrical and rectangular dielectric resonator antennas, with dimensions between *5* and *10mm*, operating at frequencies between *2* and *4GHz*, a bismuth based ceramic has been used with low reported return loss [13]: $Bi_{(3x)}Zn_{(2-3x-y)}A_y(Zn_xNb_{(2-x-z)}B_z)O_7$ where, ($A=Ca^{2+}$, $B=Sb^{5+}$, Ti^{4+}; $x=0.5–0.67$, $y=0.2–0.3$, $z=0.2–1.4$) was investigated by [15].

Manufacturers of dielectric resonators produce similar components for a certain application but there are small differences in circuit design, construction and packaging. The unique composition of materials implies a unique frequency drift as a function of temperature which in turn means that the temperature compensation needs to be unique as well. It is difficult to control the dimensions of the dielectric resonator and slight variations will result in different resonance frequencies.

2.3.11 Antenna applications

Papers reporting about dielectric resonator antennas often use elements of high relative permittivity. This is due to the availability of such elements that are intended as circuit elements. Dielectric resonators used as both antennas and filters around *2.4GHz* have been reported with a radius of about *13mm* and a relative permittivity of *36.6* [12]. These materials are hard ceramics difficult to machine. One provider is Trans-Tech Incorporated [16].

Permittivity variations due to frequency and temperature changes are given in terms of tolerances, which usually can be custom defined if necessary. The advantage of ceramics is that they do not age or absorb moisture, although condensation on the resonator surface may alter the *Q*-factor. Ceramic materials are also sensitive to the use of adhesives when assembling more complex structures.

Materials of lower dielectric constant, with values of between *3* and *25*, are provided by Cumming Microwave [17]. These materials consist of plastic stock filled with ceramic materials.

The main drawback with the ceramic and other high-permittivity materials is the more narrowband resonator behavior compared to materials with lower ε_r. This is due to the fact that Q is proportional to ε_r which for unshielded dielectric resonators is given by numerical formulas similar to equation 2.17 and related to the bandwidth by the relation

$$Q = \omega_0/\Delta\omega, \tag{2.4}$$

where ω_0 is the resonant frequency and $\Delta\omega$ is the bandwidth. For high permittivities, the relationship between Q and ε_r is analytically given by equation 2.15. Thus, for antenna elements the materials of lower permittivity should be used whereas for filters higher permittivities and therefore higher Q-factors should be used.

- Plastic materials:

  Materials of lower relative permittivity are Teflon based plastic materials. One provider of these materials is the Rogers Corporation [18], with sheets of materials with permittivity from around *2* to *10.2*. These materials are easier to machine as they are softer. A typical Rogers laminate is made up from PTFE/ceramic sheets combined with PTFE/woven glass for increased rigidity [18]. Another construction of these materials is to use a ceramic-filled, glass reinforced hydrocarbon based material. The control of the relative permittivity and dielectric losses is what restricts the frequency range. The RT/duroid series can for lower permittivities have a copper clad with planar resistor properties. The RT/duroid 6010^{TM} laminate with permittivity 10.2 is suitable for operation below the X-band (*8-12GHz*). The dielectric loss tangent for this material is low and little affected by moisture. The thickness control is within small margins. The lower permittivity RO3000-series are suitable for frequencies up to *40GHz*. Examples of applications of the lower-permittivity materials are patch antennas, band-pass filters and voltage controlled oscillators [18].

- Ceramic Materials:

  Trans Tech Incorporated [16] has two types of materials. Custom permittivities between *4* and *270* can be obtained by compounds of dielectric powders. The compounds can be used to make polymers or sintered ceramic elements. The powder is supplied in milled form or in dried granules. Examples of these powders are Silicates, Barium Titanates, Calcium Titanate, alumina based ceramics and others. The other type are the standard dielectric materials. These are also ceramic materials (Magnesium Titanate, Forsterite, Cordierite) which have permittivities of *15*, *6.3* and *4.5*, and a dielectric loss below $2 \cdot 10^{-4}$. The remaining standard dielectrics have permittivities of *37-100*.

2.4 Types of modes

The analysis of an isolated dielectric resonator with no scattering objects in its vicinity for determining the natural frequencies shows that these are complex valued [19]:

$$s_{mnp} = \sigma + j\omega, \tag{2.5}$$

where σ is the real part and ω the imaginary part of the complex frequency. As for all passive devices, these frequencies lie in the left half of the complex plane. In, particular, one certain mode would oscillate in an exponentially decreasing manner as a function of time if excited abruptly by an external source.

According to [5], a dielectric resonator of arbitrary shape can have confined modes, with a magnetic field distribution with no normal component to the boundary surface, and non-confined modes. The fields in and around the resonator peak to high values for high relative permittivity of the resonator at resonant frequencies and the sharpness of resonance increases with relative permittivity. Exact solutions for arbitrary shapes and permittivities exist only in special cases with particular symmetry. In the general case, all modes exist outside the boundary surface as well [2]. For the confined modes, the boundary surface acts as a magnetic wall as the magnetic field vanishes outside the resonator. The confined modes satisfy, from [5]

$$-\nabla \times \left(\nabla \times \vec{H}_{0m}\right) + {k_m}^2 \cdot \vec{H}_{0m} = 0\ ;\ x \in V \tag{2.6}$$

and

$$\vec{H}_{0m} = 0\ ; x \in S. \tag{2.7}$$

Here, V is the volume of the resonator and S is its boundary surface. The magnetic field vector comes from the expansion given in equation 2.9 and k_m is the wave number of the *m:th* mode.

$$\vec{H} = \overrightarrow{H_0} + \frac{\overrightarrow{H_2}}{\varepsilon_r} + \frac{\vec{H}_4}{\varepsilon_r} + \ \ldots \tag{2.8}$$

These modes are identical to the electric eigenvectors of modes for empty cavities of volume V bounded by metallic walls. Since the mode is confined, the normal component of the magnetic field vector is zero. This requires special symmetry for the shape (since there are no magnetic walls in the real world) and implies that for the general dielectric resonator, there are no confined modes. The explicit expressions for the rectangular parallelepiped have, for example, no confined modes. The most general shape for confined modes is the cylindrical body of revolution, see Figure 2.

These modes are not azimuthally dependent. The general form is:

$$\overrightarrow{H_{0m}} = \beta_m(r,z)\overrightarrow{u_\phi}, \qquad x \in V \tag{2.9}$$

where β_m satisfies, from equation 2.6 in cylindrical coordinates,

$$\frac{\partial^2 \beta}{\partial r^2} + \frac{1}{r}\frac{\partial \beta}{\partial r} + \frac{\partial^2 \beta}{\partial z^2} - \frac{\beta}{r^2} + k_m^2 \beta = 0, \tag{2.10}$$

and,

$$\beta_m = 0. \qquad \boldsymbol{x} \in S. \tag{2.11}$$

The function β_m also vanishes on the axis of revolution. For example, for a circular cavity of radius *a*

$$\beta_{ps} = \sin\frac{p\pi z}{L} J_1\left(x_s \frac{r}{a}\right); \qquad J_1(x_s) = 0 \tag{2.12}$$

$$k_{ps}^2 = \left(\frac{p\pi}{L}\right)^2 + \left(\frac{x_s}{a}\right)^2, \tag{2.13}$$

where *p* and *s* are the longitudinal and radial eigenvalue parameters and J_1 is the Bessel function of order *1*.

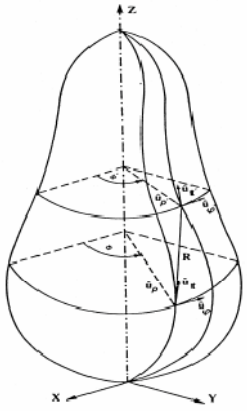

Figure 2: Example of a body of revolution with the *z*-axis as the axis of symmetry. A cross section of the shape in the *xz*- or *yz*-plane is rotated around the axis of symmetry. All cross sections parallel to the *xy* plane are circular [20].

The sphere is an exception from the requirement of azimuthal independence. The sphere has special symmetry and supports a large number of confined modes. They have no radial component and their ϕ dependence is of the form $cos(m\varphi)$ or $sin(m\varphi)$.

For traditional dielectric resonators used as filters and oscillators, a high relative permittivity is used in order to confine as many modes as possible [21], and thus most dielectric resonator microwave circuit components available on the market and in applications are of high permittivity materials. For a dielectric resonator antenna, on the other hand, a low *Q*-factor, high radiation and non-confined modes are required.

When ε_r is infinite, the electric field vanishes outside the resonator. No energy is radiated and the Q-factor is infinite. The Q-factor is the ratio between the reactive energy inserted in the resonator and the average dissipated energy per cycle. Only losses due to radiation will be considered below, i.e. Q_r is of interest. For high values of ε_r, the dielectric resonator radiates like a magnetic dipole of moment [5]

$$\overrightarrow{p_m} = \frac{1}{2}\iiint_V \vec{r} \times \left(\nabla \times \overrightarrow{H_{0m}}\right) dV. \tag{2.14}$$

This dipole moment comes from the magnetic field outside the dielectric resonator as well. The high-permittivity Q-factor is ultimately given by [5]

$$Q = \frac{6\pi\left(\sqrt{\varepsilon_r}\right)^3}{k_m^3} \frac{\iiint_{V+V'} \left|\overrightarrow{H_{0m}}\right|^2 dV}{\left[\iiint_V \overrightarrow{H_{0m}} dV - \iint_S \psi_{0m} \vec{u}_n dS\right]^2}. \tag{2.15}$$

Here V' is the volume outside the dielectric resonator, $\vec{u}_n$ is the unit normal vector to S and ψ_{0m} is the scalar potential to $\overrightarrow{H_{0m}}$ outside the dielectric resonator, i.e.

$$\overrightarrow{H_{0m}} = \nabla \psi_{0m} \qquad \text{x} \notin \text{V}. \tag{2.16}$$

A numerical formula for the $TE_{01\delta}$ mode Q-factor of a cylindrical dielectric resonator is as follows [11]:

$$Q = 0.078192\varepsilon_r^{1.27}\left[1 + 17.31\left(\frac{h}{a}\right) - 21.57\left(\frac{h}{a}\right)^2 + 10.86\left(\frac{h}{a}\right)^3 - 1.98\left(\frac{h}{a}\right)^4\right]. \tag{2.17}$$

This indicates that the Q-factor grows as power function of ε_r. A plot of Q versus aspect ratio is shown in Figure 3.

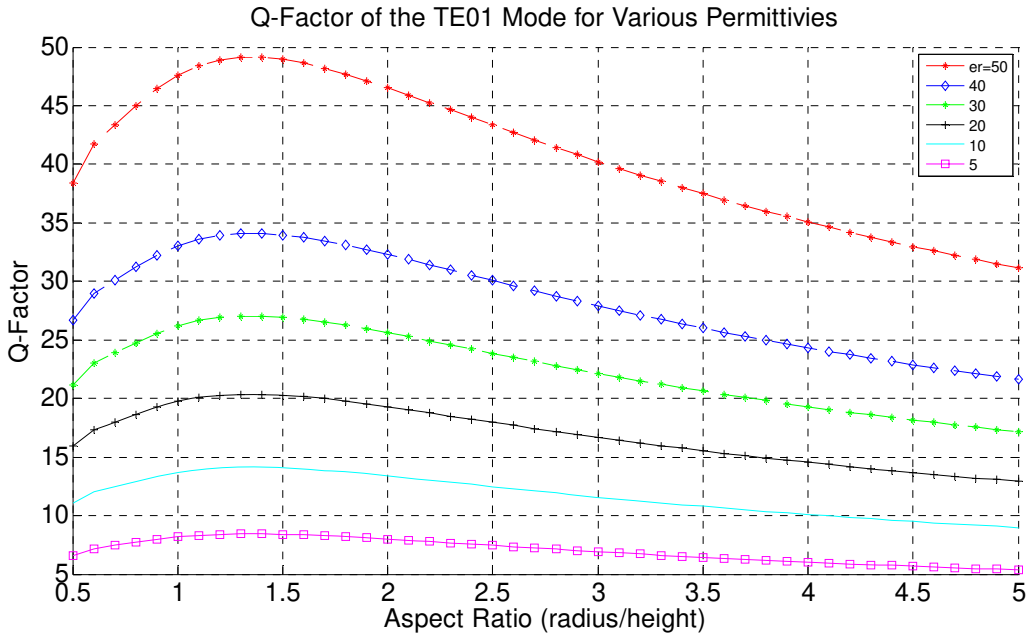

Figure 3: The $TE_{01\delta}$ mode Q-factor shows a clear dependence on the relative permittivity of the cylindrical dielectric resonator.

The statements above indicate that a low relative permittivity is desired for a dielectric resonator used as an antenna. This must, on the other hand, be weighed to the dimensions required for resonance in a piece of material at a certain frequency. For a frequency "f", the dielectric wavelength is given as:

$$\lambda_d = \frac{\lambda_0}{\sqrt{\varepsilon_r}} = \frac{c_0}{f\sqrt{\varepsilon_r}}, \tag{2.18}$$

where c_0 is the speed of light in vacuum and λ_0 and λ_d are the wavelengths in free space and the dielectric, respectively. For a cylindrical dielectric resonator, the minimum required dimensions are a diameter of $\lambda_d/2$ and a height of $\lambda_d/4$. The conclusion from equation 2.18 is that the higher the relative permittivity, the more compact the dielectric resonator antenna element can be.

2.5 Shapes of Dielectric Resonator Antennas

The dielectric resonator antenna can be formed in many different shapes but we can divide them into four main groups which are as follows:

i. Cylindrical
ii. Hemispherical
iii. Parallelepiped
iv. Other shapes

Most reports found from the literature are about cylindrical, parallelepiped and half-cylindrical shapes.

2.5.1 The Cylindrical Dielectric Resonator

The cylindrical dielectric resonator antenna is characterized by a radius a, a height h and a relative permittivity ε_r. The aspect ratio and its inverse determine the resonant frequency and Q-factor respectively. Two dielectric resonators of different shape may have the same resonant frequency but not the same Q-factor, which allows for two degrees of freedom (radius and aspect ratio) compared to the hemispherical dielectric resonator which only has the radius as a degree of freedom, see Figure 4.

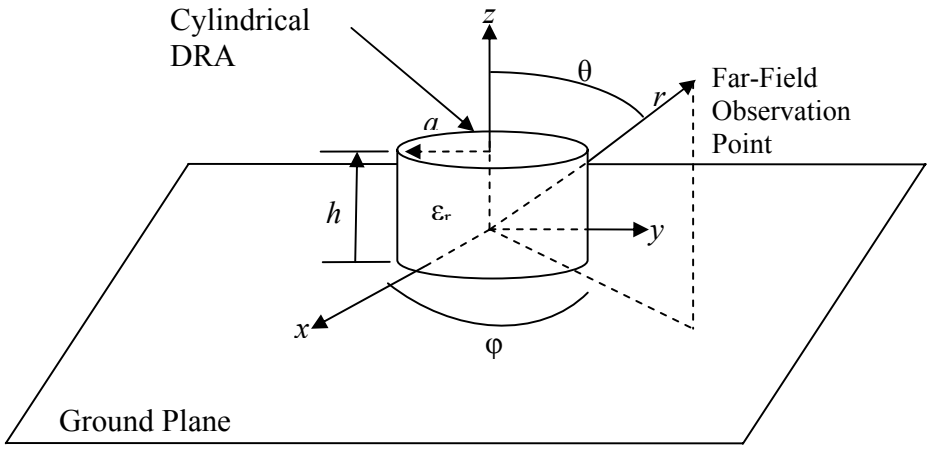

Figure 4: Geometry of the cylindrical dielectric resonator mounted on a ground plane in a spherical coordinate system [11].

2.5.1.1 Field Distribution

For the dielectric resonator of cylindrical shape, the three first common modes are $TE_{01\delta}$, $TM_{01\delta}$ and $HE_{11\delta}$. The *TE* (transverse electric) and *TM* (transverse magnetic) modes have no longitudinal electric and magnetic field components respectively, whereas the hybrid modes do and are called *HE* or *EH* if the $\overrightarrow{E_z}$ or the $\overrightarrow{H_z}$ component respectively is dominant [11].

The field distributions inside the cylinder for the first three common modes are shown in Figure 5. The lowest resonant frequency is for the $TM_{01\delta}$ mode. The radiation patterns of the $TE_{01\delta}$ and $TM_{01\delta}$ modes are omnidirectional donut shaped.

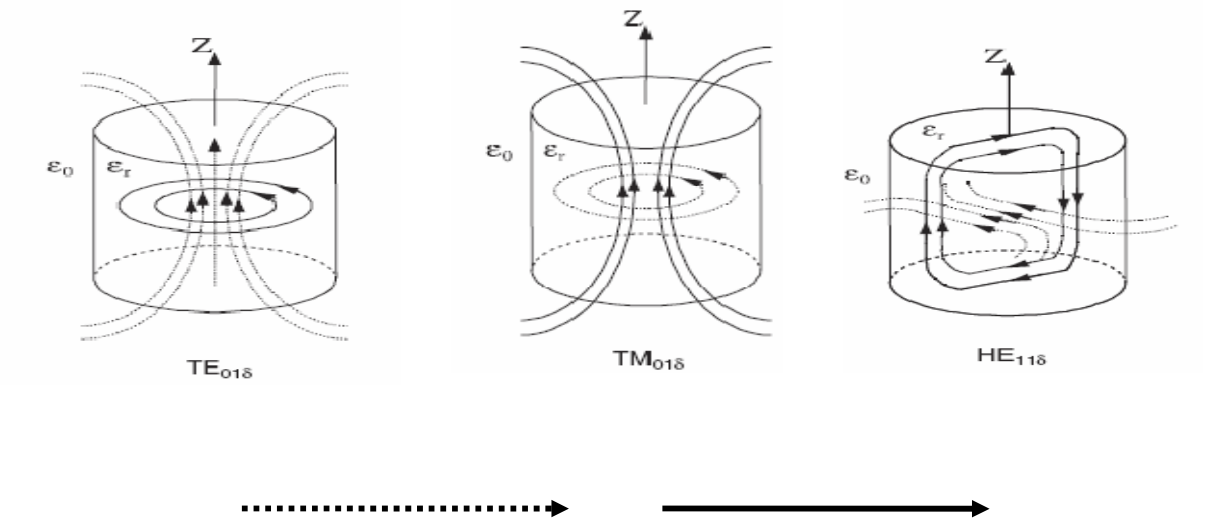

Figure 5: Field distribution inside the dielectric cylinder for the three first common resonant modes. The pictures are from [3].

The far field radiation patterns for the $TE_{01\delta}$ and $TM_{01\delta}$ modes are shown in Figures 6-7 and 8-9, respectively. It is clear that the electric field is donut-shaped with different polarization, horizontal (azimuthal) and vertical (elevational) respectively.

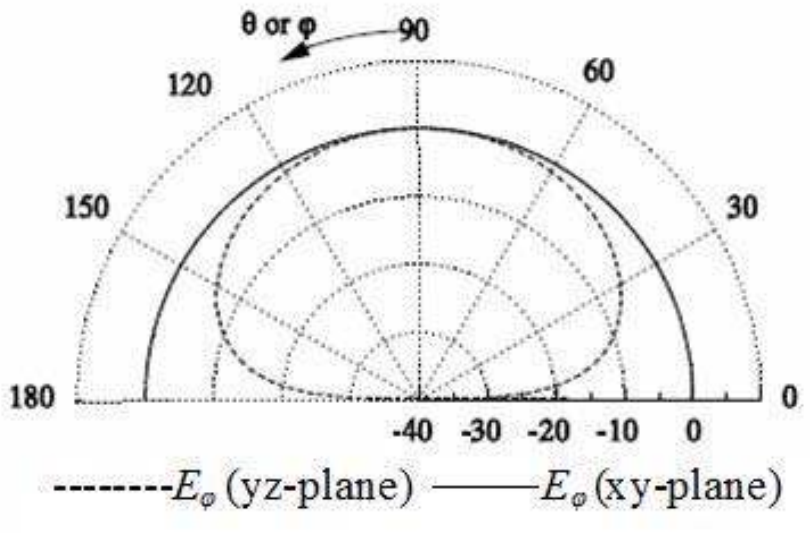

Figure 6: Far field radiation pattern for the $TE_{01\delta}$ mode of a cylindrical dielectric resonator antenna. It resembles a donut around the z-axis with electric field polarization in the azimuthal direction [3].

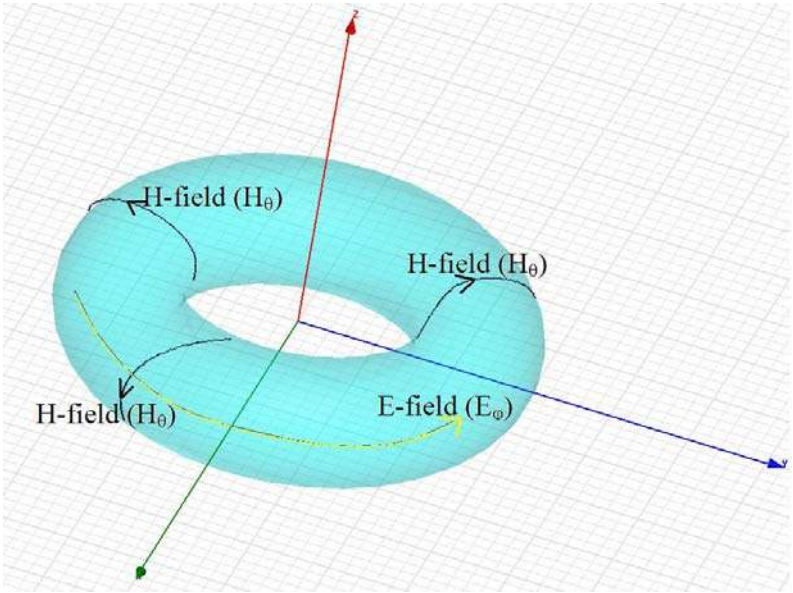

Figure 7: 3D Radiation pattern of the TE_{01} mode described in Figure 6.

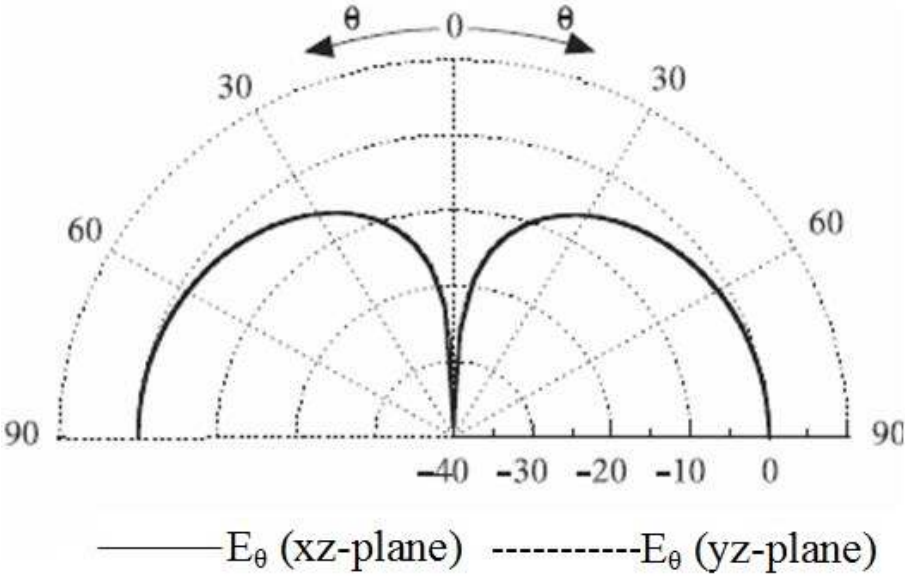

Figure 8: Far field radiation pattern for the $TM_{01\delta}$ mode of a cylindrical dielectric resonator antenna. It resembles a donut around the z-axis with electric field polarization in the direction of elevation [3].

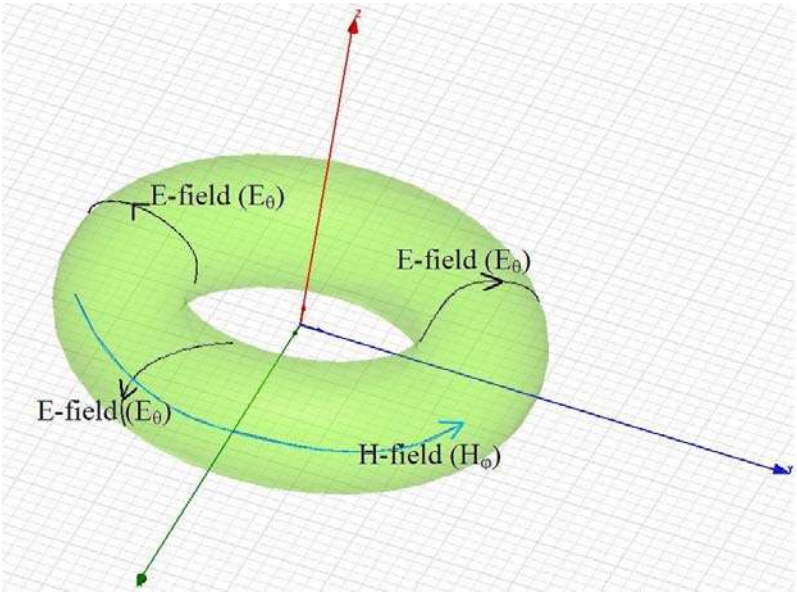

Figure 9: 3D Radiation pattern of the TM_{01} mode described in Figure 8.

The radiation pattern of the $TM_{01\delta}$ mode looks like a *z*-directed half-wavelength electric dipole. a the $TE_{01\delta}$ mode looks like a *z*-directed half-wavelength magnetic dipole. The radiation pattern of the $HE_{11\delta}$ mode resembles the radiation pattern of a half-wavelength electric dipole along the *y*-axis and is shown in Figures 10 and 11.

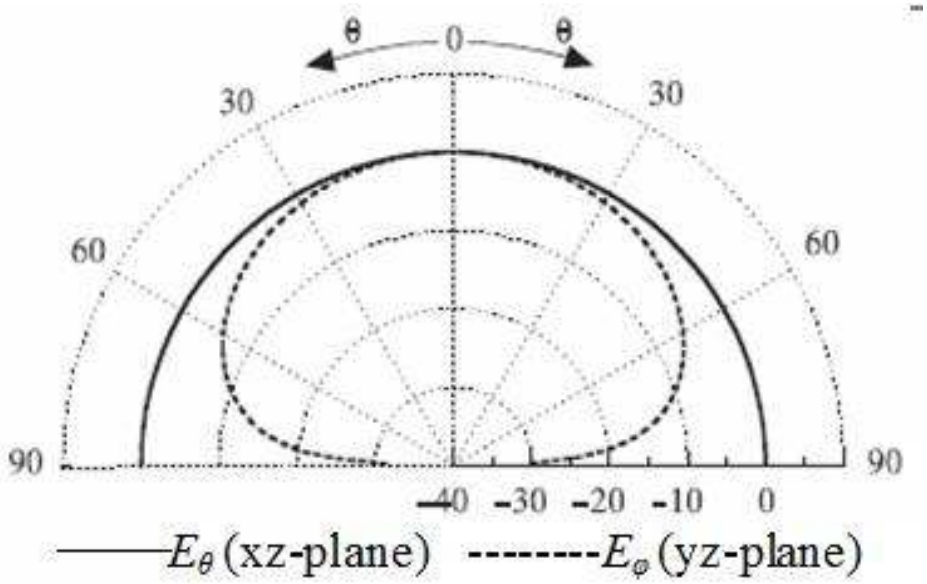

Figure 10: Far field radiation pattern for the $HE_{11\delta}$ mode of a cylindrical dielectric resonator antenna [3].

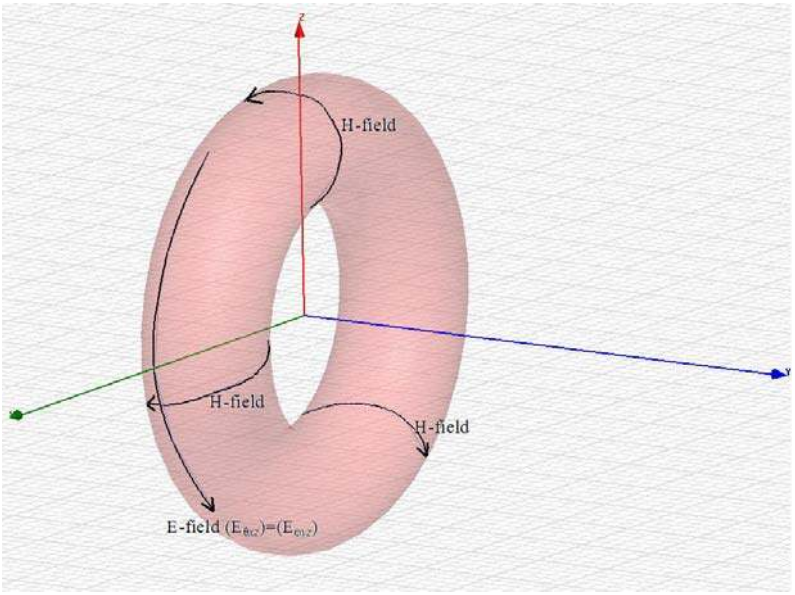

Figure 11: 3D Radiation pattern of the HE_{11} mode shown in Figure 10.

2.5.1.2 Resonant Frequencies

The resonant frequency for the TE_{01} mode in a cylindrical dielectric resonator on a ground plane (see Figure 4) is given by [3]:

$$f_0 = 2.921 \cdot \frac{c\varepsilon_r^{-0.465}}{2\pi a}\left[0.691 + 0.319\frac{a}{2h} - 0.035 \cdot \left(\frac{a}{2h}\right)^2\right]. \tag{2.19}$$

The numerical expression for the Q-factor is given by:

$$Q = 0.012 \cdot \varepsilon_r^{1.2076}\left[5.270\frac{a}{2h} + 1106.188\left(\frac{a}{2h}\right)^{0.625} \cdot e^{-1.0272x}\right]. \tag{2.20}$$

These expressions have been derived by large numerical simulations and curve-fitting methods [22]. The denominator $a/(2h)$ comes from the fact that the ground plane, by image theory, implies a cylindrical resonator of twice the physical height. The graphical form is shown in Figures 12.

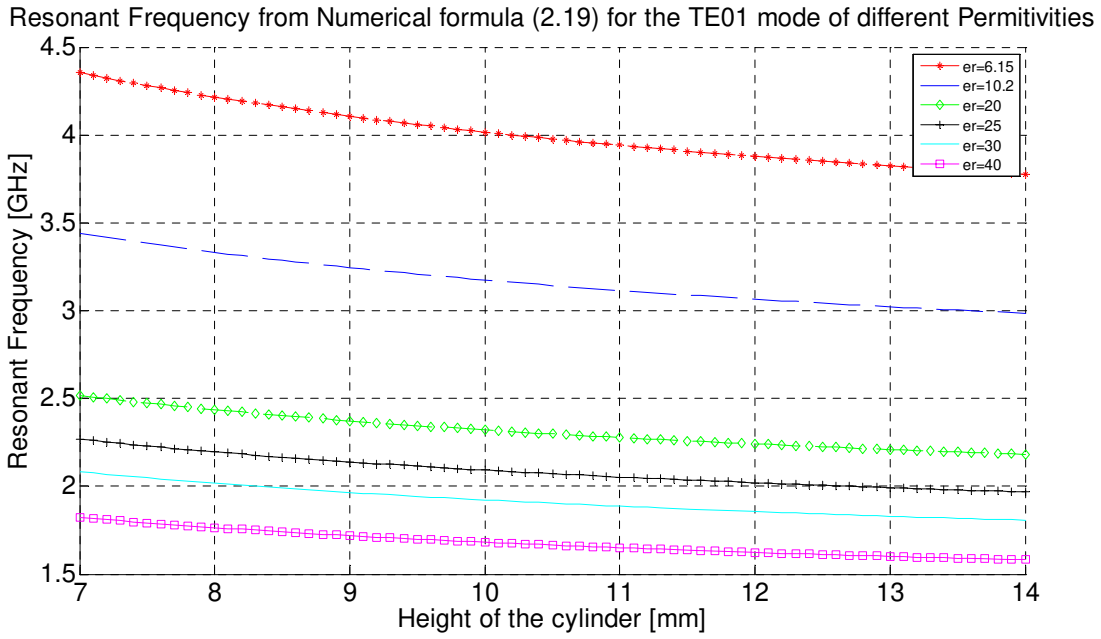

Figure 12: Resonant frequencies as a function of height of the *TE₀₁* mode of a cylindrical DRA with different permittivity and radius *13.22mm*. The model used is from the numerical formulas by Kishk et al [3].

The resonant frequencies for the TM_{01} and HE_{11} are given by [22]:

$$f_0 = 2.933 \cdot \frac{c\varepsilon_r^{-0.468}}{2\pi a}\left[1-\left(0.075-0.05\cdot\frac{a}{2h}\right)\left(\frac{\varepsilon_r-10}{28}\right)\right]\left[1.048+0.377\left(\frac{a}{2h}\right)-0.071\left(\frac{a}{2h}\right)^2\right] \quad (2.21)$$

and

$$f_0 = 2.735 \cdot \frac{c\varepsilon_r^{-0.436}}{2\pi a}\left[0.543+0.589\frac{a}{2h}-0.050\cdot\left(\frac{a}{h}\right)^2\right]. \quad (2.22)$$

Their Q-factors are given by

$$Q = 0.009\varepsilon_r^{0.888}\cdot e^{0.040\varepsilon_r}\left[1-\left(0.3-0.2\frac{a}{2h}\right)\left(\frac{38-\varepsilon_r}{28}\right)\right]\left[9.498\left(\frac{a}{2h}\right)+2058.33\left(\frac{a}{2h}\right)^{4.322}\cdot e^{-3.501x}\right] \quad (2.23)$$

and

$$Q = 0.013\cdot\varepsilon_r^{1.202}\left[2.135\frac{a}{2h}+228.034\left(\frac{a}{2h}\right)\cdot e^{-2.046x+0.111\left(\frac{a}{2h}\right)^2}\right]. \quad (2.24)$$

The graphical form is shown in Figures 13 and 14.

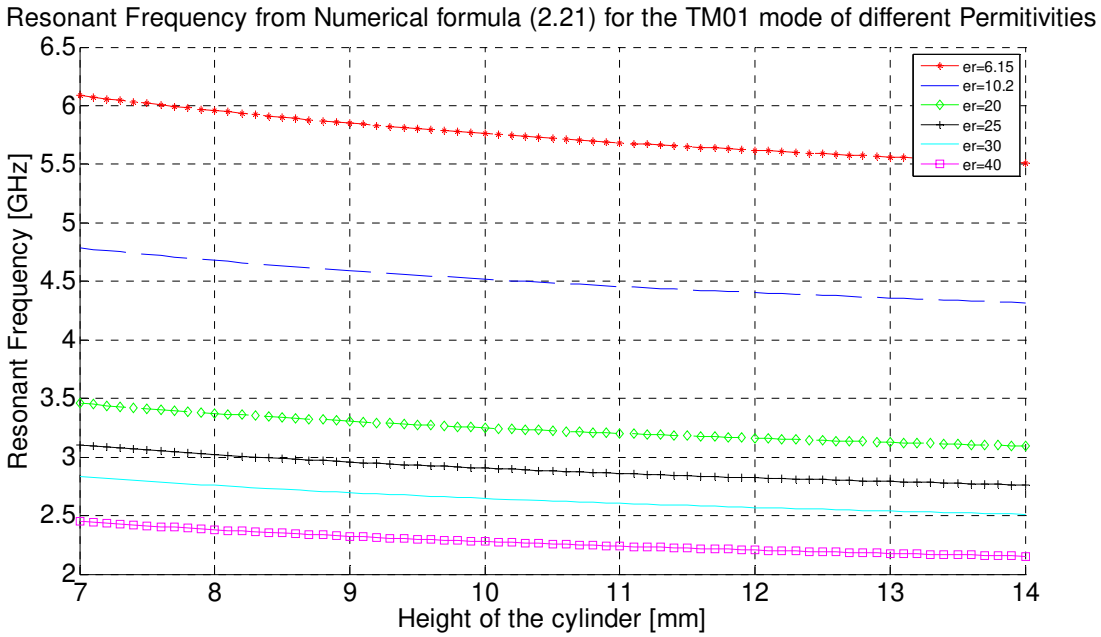

Figure 13: Resonant frequencies as a function of height of the TM_{01} mode of a cylindrical DRA with different permittivities and radius *13.22mm*. The model used is from the numerical formulas by Kishk et al [3].

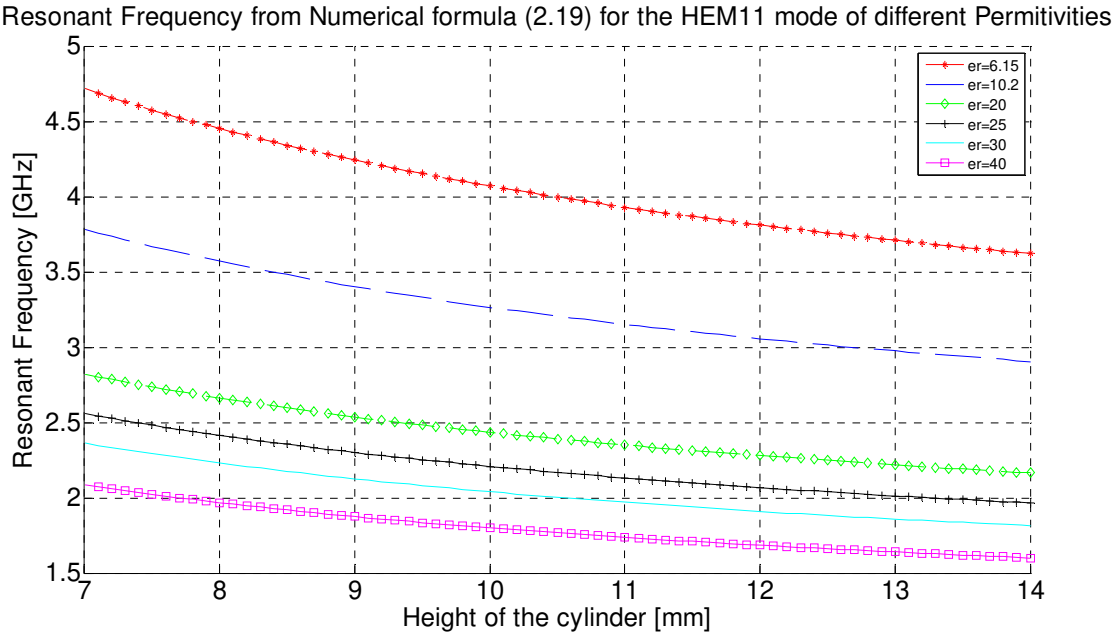

Figure 14: Resonant frequencies as a function of height of the HE_{11} mode of a cylindrical DRA with different permittivity and radius *13.22mm*. The model used is from the numerical formulas by Kishk et al [3].

The analytical closed form expressions for a metal-shielded cylindrical resonance cavity:

$$f_0 = \frac{1}{2\pi\sqrt{\mu_0\varepsilon_0\varepsilon_r}}\left[\left(\frac{\xi_{01}}{a}\right)^2 + \left(\frac{p\pi}{2h}\right)^2\right]^{1/2}. \qquad (2.25)$$

This is the resonant frequency of the TM_{01} and TE_{01} modes and ξ_{01} is the first zero of the zero-order Bessel function or its derivative, repectively. The parameter p denotes the number of longitudinal variations in the cylinder and $2h$ is the cylinder height which needs to be doubled compared to the numerical formulas above since the cavity is not on a ground plane and image theory does not apply here. The graphs for the first ($p=1$) TE_{01} and TM_{01} resonant frequencies are shown in Figures 15 and 16. All figures below are showing the different modes with different models for a cylindrical dielectric resonator of radius *13.22mm* with variation in height and permittivity. The radius is the same as the one used in [12] for comparison.

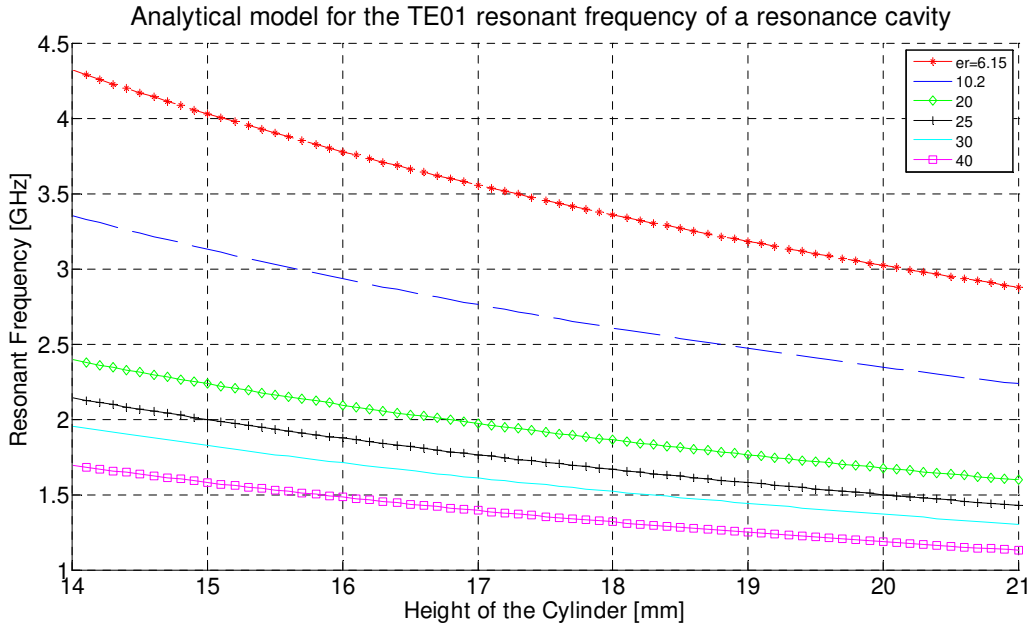

Figure 15: Resonant frequencies as a function of height of the TE_{01} mode of a metallic cylindrical DRA with different permittivities and radius 13.22mm. The model used is from the analytical formulas for a cylindrical resonance cavity given by (2.25) [25].

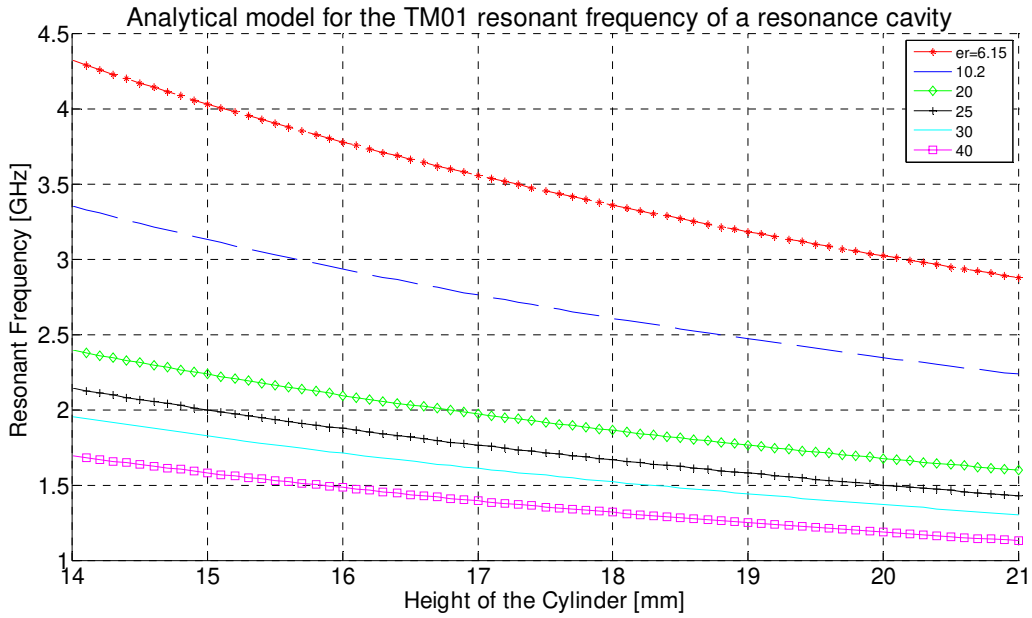

Figure 16: Resonant frequencies as a function of height of the TM_{01} mode of a cylindrical DRA with different permittivities and radius *13.22mm*. The model used is from the analytical formulas for a cylindrical resonance cavity given by (2.25) [25].

For a dielectric resonator situated on a substrate used as dielectric material for a microstrip feed, the situation is more complicated, since there is a dielectric below the resonator, and the normal component of the electric displacement field will be continuous over the boundary.

The method that has proven to be of best approximation during the modeling is the program FOAM© [23], a computer program written by D. Kajfez for designing dielectric resonators. This numerical solution is based on the Itoh-Rudokas model from 1977 [24] which has its core in an assumption of exponential decay of the fields outside the resonator.

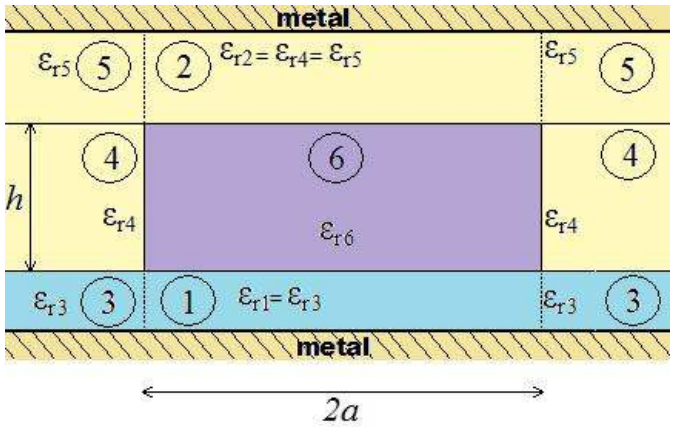

Figure 17: Geometrical model of the dielectric resonator on a substrate with boundaries used for the analysis FOAM©. The underlying mathematical model is due to Itoh-Rudokas [24].

The program assumes a dielectric resonator between two metal plates of infinite transverse extent. The input parameters are the resonator radius, permittivity, height and distance to the upper plate as well as substrate thickness and permittivity, see Figure 17. The dielectric resonator is in region 6. The fields in regions 4 and 6 are assumed to be the propagating modes in a circular waveguide, with an exponential decay in the radial direction for region 4 [24]. Regions 3 and 5 are ignored in this model in the sense that the fields are set to zero here. Regions 1 and 2 have fields with exponential decay in the longitudinal direction (along *h*) [24]. These assumptions, together with the boundary conditions between the regions lead to eigenvalue equations that are solved numerically. The output information are the resonant frequencies of the *16* lowest modes, see also Chapter 2. The values given by FOAM© for the same dimensions as in Figure 12, 13 and 14 are interpolated and shown in Figures 18 and 19.

As can be concluded from the figures, both FOAM© and the numerical methods in equation 2.19, 2.21 and 2.22 have the same basic shape and behavior as the basic model in equation 2.25. Note that the curves illustrating equation 2.25 in Figures 15 and 16 and the numerical formulas 2.19, 2.21 and 2.22 in Figures 12, 13 and 14, respectively, are lying on lower frequencies (around *3-6GHz*) than the FOAM© methods (around *10GHz* for *7mm* height).

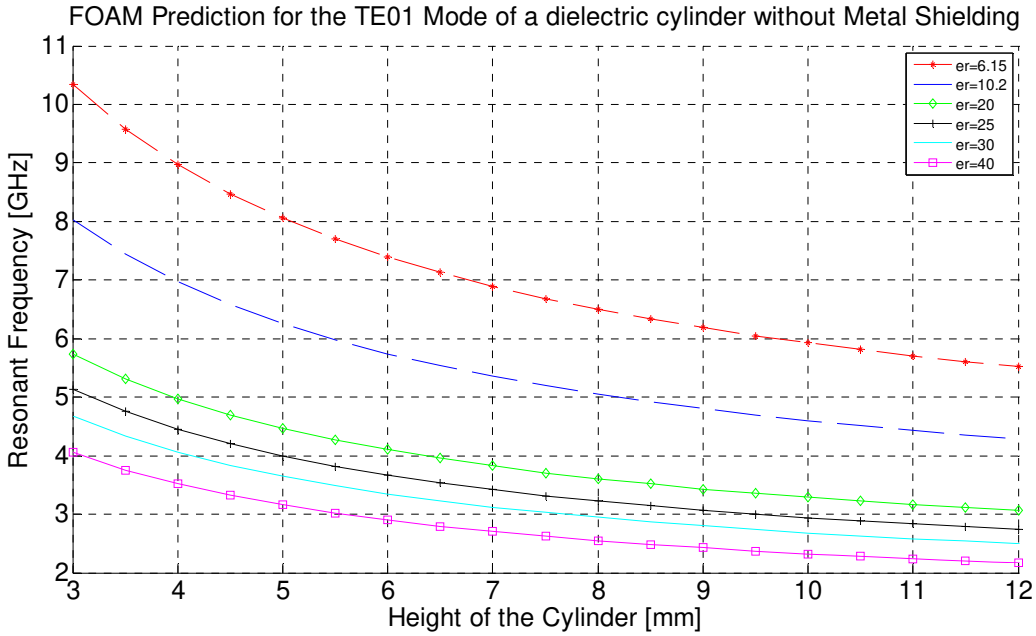

Figure 18: Resonant frequencies as a function of height of the TE_{01} mode of a cylindrical DRA with different permittivities and radius *13.2 mm*. The calculations are made by FOAM© [23].

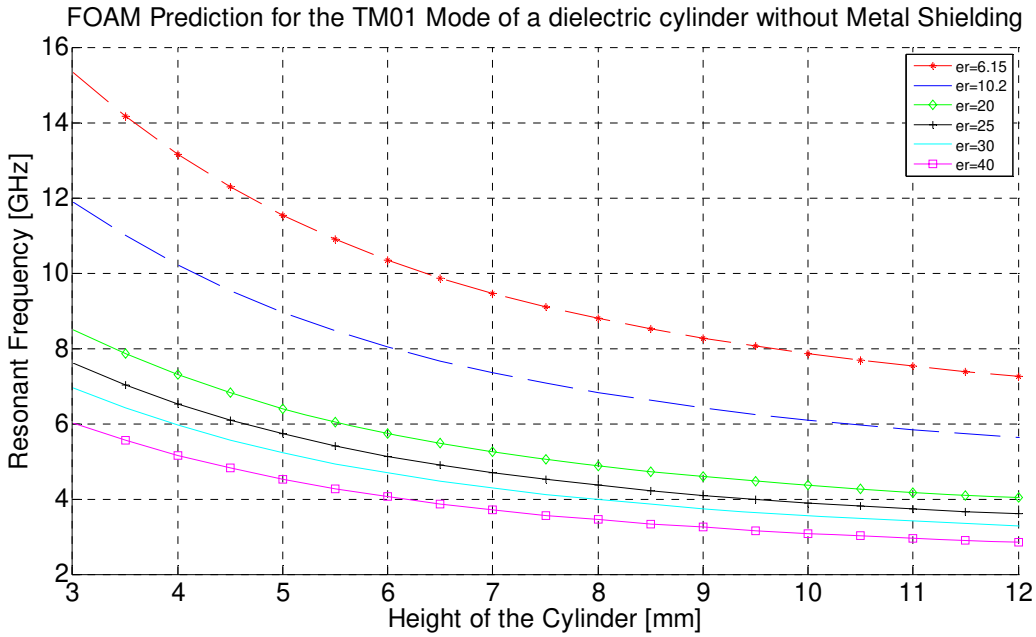

Figure 19: Resonant frequencies as a function of height of the TM_{01} mode of a cylindrical DRA with different permittivities and radius *13.22mm*. The calculations are made by FOAM© [23].

2.5.2 The Hemispherical Dielectric Resonator

The characteristics of the hemispherical dielectric resonator are determined by its relative permittivity ε_r and radius a, see Figure 20.

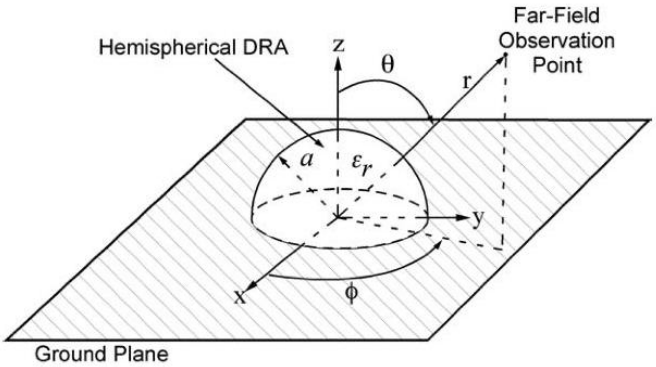

Figure 20: Geometry of the hemispherical dielectric resonator mounted on a ground plane in a spherical coordinate system [11].

The electromagnetic resonant modes have been analytically analyzed in depth. If the hemispherical dielectric resonator is placed on a perfectly conducting ground plane, image theory can be used and the analytical solutions for the sphere can be found. The modes can be divided into *TE* and *TM* modes, where a transverse mode has no radial field component with respect to a spherical coordinate system. The fundamental mode is the TE_{111} whose radiation pattern is

similar to that of a short magnetic dipole situated horizontally above a ground plane, see Figure 21. The other mode of interest is the TM_{101} which has a similar radiation pattern as a quarter-wave electric monopole above ground, see Figure 9. The hemispherical shape can be excited by a probe or a slot aperture.

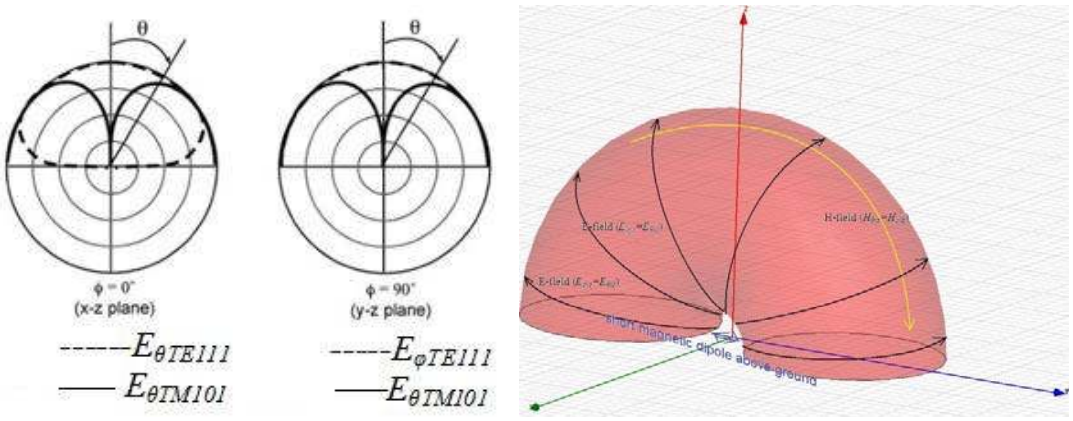

Figure 21: Radiation patterns of the TE_{111} (horizontal magnetic dipole) and TM_{101} (electric monopole) modes in a hemispherical dielectric resonator (left) [11] and 3D Radiation pattern of the TE_{111} mode (right).

Hemispherical resonators have very limited practical value, due the difficulty in fabrication and a lack of freedom in design parameters. Some flexibility can be achieved by using a non-homogeneous distribution of permittivity, i.e. by having a core of permittivity ε_{r1} with radius b covered by a shell of outer radius a and permittivity ε_{r2}, as shown in Figure 22 [11].

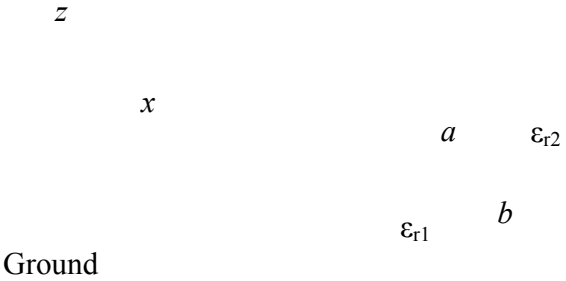

Figure 22: A hemispherical dielectric resonator with non-uniform permittivity distribution [13].

The radiation Q-factor and the resonant frequency for the TE_{111} mode can be calculated by the following equation [11]:

$$\frac{J_{\frac{1}{2}}(\sqrt{\varepsilon_r}k_o a)}{J_{\frac{3}{2}}(\sqrt{\varepsilon_r}k_o a)} = \frac{H_{\frac{1}{2}}^{(2)}(k_o a)}{\sqrt{\varepsilon_r}H_{\frac{1}{2}}^{(2)}(k_o a)}, \tag{2.26}$$

where $J(x)$ is the first-order Bessel function, $H^2(x)$ is the second-order Hankel function, and k_0 is the free-space wave number. A similar transcendental equation exists for the TM_{101} mode. When k_0 is obtained then the resonant frequency for this mode can be determined [11]:

$$f_{GHz} = 4.7713\, Re(k_o a)/a_{cm} \tag{2.27}$$

$TE_{111}Mode$: $$Re(k_o a) = 2.8316\varepsilon_r^{-0.47829} \tag{2.28}$$

$$Q = 0.08 + 0.796\varepsilon_r + 0.01226\varepsilon_r^2 - 3\cdot 10^{-5}\varepsilon_r^3 \tag{2.29}$$

$TM_{101}Mode$: $$Re(k_o a) = 4.47226\varepsilon_r^{-0.505} \tag{2.30}$$

For $\varepsilon_r \leq 20$ $$Q = 0.723 + 0.9324\varepsilon_r - 0.0956\varepsilon_r^2 - 0.00403\varepsilon_r^3 - 5\cdot 10^{-5}\varepsilon_r^4 \tag{2.31}$$

For $\varepsilon_r > 20$ $$Q = 2.621 - 0.547\varepsilon_r + 0.01226\varepsilon_r^2 - 2.59\cdot 10^{-4}\varepsilon_r^3 \tag{2.32}$$

2.5.3 The Rectangular Parallel Epiped Dielectric Resonator

The rectangular parallel epiped resonator antenna is characterized by a height h, a width w, a depth d, and a dielectric constant ε_r, as shown in Figure 23. The rectangular shape offers a second degree of freedom. A rectangular dielectric resonator gives more flexibility to the manufacturer making it more versatile in achieving the desired bandwidth characteristics for a given resonant frequency and dielectric constant. The ratios w/h and w/d can be chosen independently of each other. This helps to design either a resonator tall and slender or a thin and wide resonator by selecting the desired aspect ratio, depending on the particular application. The aspect ratio also decides the radiation Q-factor [11].

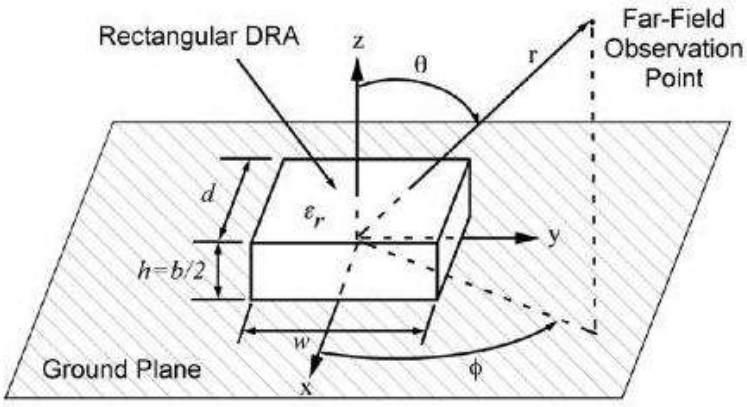

Figure 23: Geometry of the rectangular dielectric resonator mounted on a ground plane in a spherical coordinate system [11].

As in the case with the cylindrical dielectric resonator, the starting point is the rectangular waveguide. An assumption of perfect magnetic walls for the four surfaces parallel to the longitudinal direction is made. The two end surfaces, normal to the direction of propagation are

assumed to maintain a continuous transition of the tangential electric and magnetic fields [11]. With the resonator placed on a ground plane, typically the *TE* modes are excited, but *TM* modes are possible as well. The *TE* modes radiate like short magnetic dipoles in the *x*, *y* and *z*-directions. The resonant frequency of each of these modes depends on the resonator dimensions. If $w > d > b$, unwanted modes will not appear in between these *TE* modes. By properly choosing a size, an undisturbed frequency band of operation can be achieved.

2.5.4 Other Shapes for Dielectric Resonator Antennas

Besides the different shapes mentioned above, there exist many other variants of the basic shapes designed for different requirements, such as circular polarization, wide bandwidths or easy fabrication. Another possible strategy for bandwidth enhancement is a hybrid solution, which is a combination of a dielectric resonator antenna and some other antenna. A single element dielectric resonator antenna can have better bandwidth if the feeding mechanism is optimized or if the resonator itself or the feeding is geometrically changed (stub matching).

2.5.4.1 Split-Cylinder Dielectric Resonator

By modifying the cylindrical shape, improved bandwidths or more compact sizes can be obtained for a dielectric resonator antenna. The split-cylinder dielectric resonator is especially suitable for excitation by slot apertures, since a dual polarized antenna would have low cross-polarization levels. For example, the TE_{01} mode radiates like a short horizontal magnetic dipole. The slot also radiates like a short magnetic dipole. Thus this structure can, when properly tuned, have several resonances and an increased bandwidth [26]. One such element is shown in Figure 24. The U-shaped slot is a parasitic slot used for tuning difference in frequency between the resonances and for impedance matching.

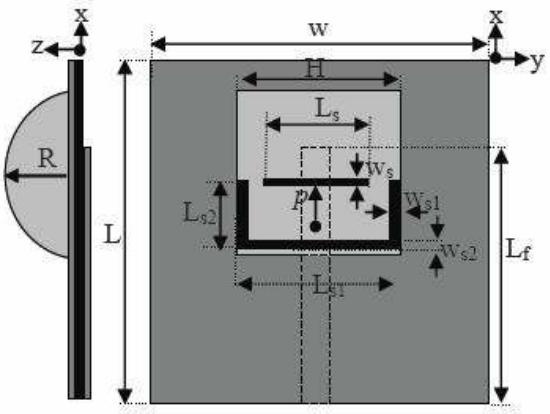

Figure 24: Cross sectional and top view of a half cylindrical dielectric resonator antenna with two slots [26].

2.5.4.2 Cylindrical-Ring Dielectric Resonator

By removing the most central part of a cylindrical dielectric resonator, the *Q*-factor can be reduced [11]. From the theory of resonance cavities, this loss of volume implies an increase in resonance frequency. An illustration of this structure is found in Figure 25.

A way to modify the cylindrical-ring dielectric resonator is to add a circular metallic disc on top of the cylinder above the cavity. By adjusting the disk size, a certain amount of tuning is possible.

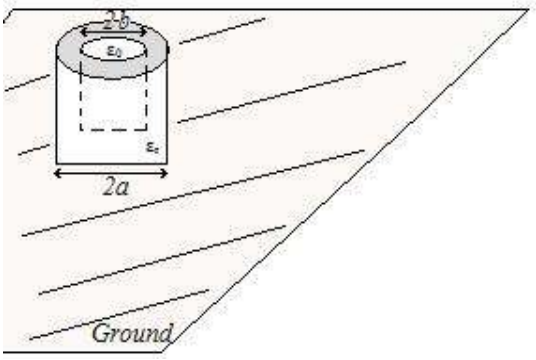

Figure 25: A cylindrical-ring dielectric resonator with outer radius *a* and inner radius *b* on a ground plane.

2.5.4.3 Cross-Shaped Dielectric Resonator

A dielectric resonator antenna developed for generating circular polarization is the cross-shaped DRA. It is made by two crossing rectangular resonators of different lengths, so that their resonant frequencies vary by a small amount. This is compensated by the excitation which is made by one single slot at the bottom center of the resonator, as shown in Figure 26.

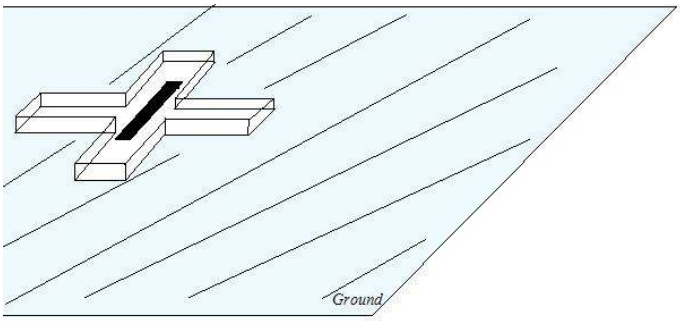

Figure 26: A cross-shaped DRA fed by a slot aperture on a ground plane.

2.5.4.4 Perforated Dielectric Resonator

One of the main drawbacks of dielectric resonator antennas is the difficulty in manufacturing. This can be omitted by so-called perforated DR antennas. Resonator elements are typically machined from ceramic blocks or cast from molds. In array applications, a high number of

elements must be precisely placed on a ground plane. For microstrip systems, this is obtained by etching from substrates with circuit board technology. In a similar way, the dielectric sheet can be perforated in order to create regions of lower permittivity surrounding the "elements" as islands of higher permittivity. The lowered permittivity of the surroundings of the actual dielectric resonator can be calculated from [11]:

$$\varepsilon_{eff} = (1 - \alpha)\varepsilon_r + \alpha, \tag{2.33}$$

where α is the co-called filling factor depending on the arrangement of the perforations. An illustration is shown in Figure 27.

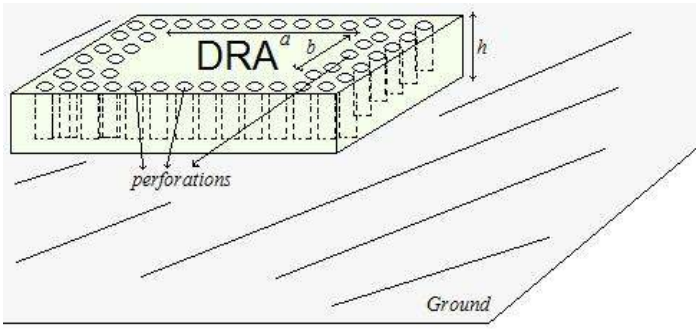

Figure 27: A rectangular perforated DRA on a ground plane.

2.5.4.5 Cone-Shaped Dielectric Resonator

Conical and split-conical dielectric resonators, see Figure 28 are reported to have large bandwidths of up to *50*% [3] for a relative permittivity of *12* and a base and height size around *50mm*. The split structures do have a tendency to excite higher order modes, which perturbs the radiation pattern in the middle of the frequency band, as shown in Figure 29.

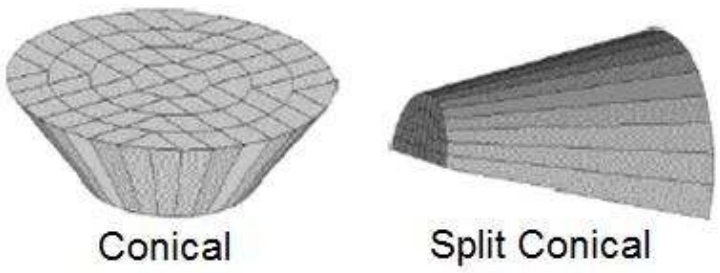

Figure 28: Geometry of a cone-shaped and split-cone shaped DRA [3].

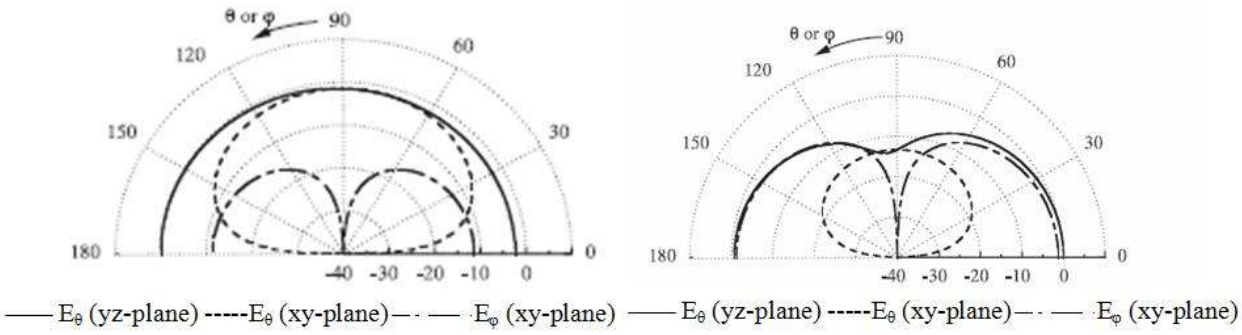

Figure 29: Radiation pattern of a split-conical dielectric resonator antenna, beginning of operation band (left) and in the middle of the band (right) [3].

2.5.4.6 Stepped-Stair Structured Dielectric Resonator

The stepped-pyramid structure has been reported to have bandwidths up to *60%*. The stepped stair design has also been evaluated for the cylindrical shape with similar bandwidths [3].

2.6 Wideband Techniques

There are many techniques to improve dielectric resonator antennas to achieve higher bandwidths and different fabrication methods can be used which are as follows [3]:

- Optimizing the dielectric parameters and the feeding pattern.
- Using a transformer and stub for microstrip feeding.
- Changing the shape of the dielectric resonator antenna, see Figure 30.
- Introducing an air gap between the ground plane and dielectric resonator.
- Reducing the permittivity of the dielectric resonator.
- Combining two different dielectric materials in a dielectric resonator antenna.
- Making a cavity backed dielectric resonator antenna
- Using hybrid antennas including the dielectric resonator antenna and a microstrip patch, dielectric resonator antenna loaded monopole, etcetera.

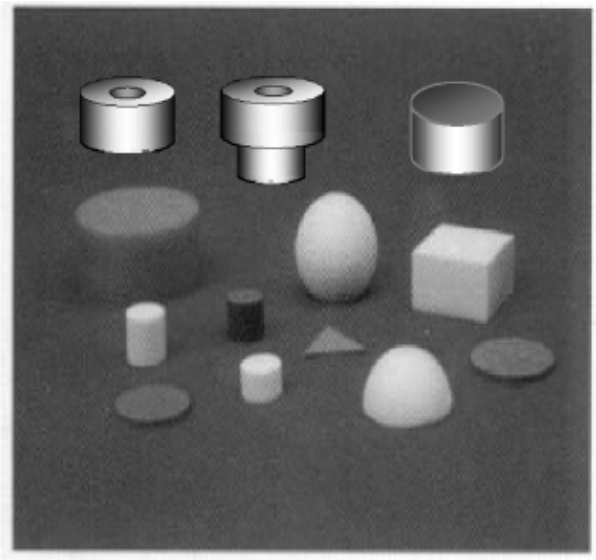

Figure 30: Various shapes of dielectric resonators [3].

2.7 Excitation Techniques

The operational mode depends on the method of excitation of the dielectric resonator antenna. The coupling mechanisms significantly affect the resonant frequency and radiation *Q*-factor of a dielectric resonator antenna. There are many different techniques which have been used and adopted in the past. These include coaxial probe, aperture coupling with a microstrip feedline, aperture coupling with a coaxial feedline, waveguide coupling with a microstrip feedline, direct microstrip feedline, coplanar feed, soldered through probe, slot line, conformal strip and direct image guide. Some of the excitation methods are shown in Figure 31 [3].

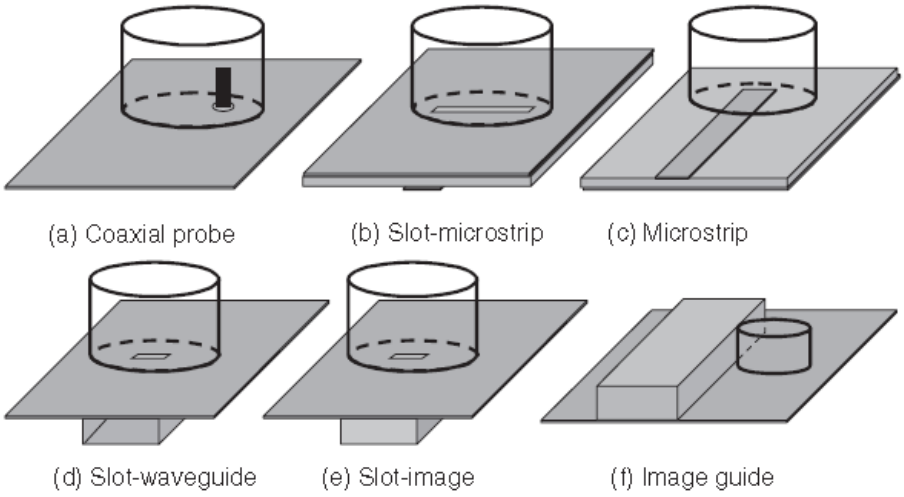

Figure 31: Different excitation methods for dielectric resonator antennas [3].

To couple to the aperture different shapes can be used such as a narrow slot, cross or C-shaped cut in the ground plane. These shapes can be fed by a microstrip line or a coaxial feedline beneath the aperture cut or the ground plane on the surface of the waveguide. In this way, the behavior of the aperture is like a magnetic current which runs parallel to the length of the slot and excites the magnetic field of the dielectric resonator antenna. If the aperture size is adjusted or the dielectric resonator antenna is moved with respect to the aperture, the coupling level can be adjusted. The feeding network is kept below the ground plane which gives the advantage of avoiding spurious radiation. Moreover, slot aperture is widely used for integrating the dielectric resonator with the printed feed structure.

The use of coplanar waveguides in exciting the dielectric resonator appears to be highly useful because they enable easy coupling with MMICs. This helps to adjust the coplanar level and the position of the dielectric resonator over the coplanar structure. Impedance tuning can also be adjusted by adding a stub, slot, or loop at the end of the coplanar line, although the coplanar line and the coplanar loop work alike. In this way, the operational mode can be selected by changing the position of the dielectric resonator over the loop.

The dielectric image waveguide excitation method offers advantages over the microstip line methods because it does not suffer from conductor losses even at millimeter wave frequencies. Usually the coupling is small between the dielectric resonator and the guide but it can be adjusted or increased by operating the guide closer to the cutoff frequency. This method is similar to the waveguide but this kind of excitations can be found in many applications, especially in series-fed linear dielectric resonator antenna arrays.

In excitation through coaxial probe feed, the pin of the coaxial transmission line is extended through the ground plane. This acts as an electric current running vertically through the dielectric resonator antenna. The strength of the coupling depends on the length of the probe and different modes can be activated by changing the location of the probe, depending on what mode is desired. Another advantage of this method is that the antenna is directly connected to the circuit of 50Ω characteristic impedance without any matching network.

The other method for excitation is the microstrip method which is the simplest method to activate the dielectric resonator antenna. The microstrip line is printed on the same substrate which is directly connected to the dielectric resonator antenna. By altering the permittivity of the substrate and by changing the distance to the dielectric resonator antenna, the level of the coupling can be adjusted. For wider bandwidth the permittivity should be kept low but this requires better coupling. Microstrips are easy to fabricate and it is also cost effective because the feedline is printed on the substrate but the disadvantage of microstrip is the limitation in polarization, as the polarization of an array is dedicated to the orientation of the microstrip line [3].

If both a coaxial probe and a microstrip line are used simultaneously, it gives the opportunity of exciting different modes simultaneously. By placing two microstrip lines near the antenna, two different modes can be excited.

2.8 Polarization

The polarization is defined as the orientation of the electric field vector. The electric field vector is perpendicular to both the direction of the traveling wave and the magnetic field vector. In general, all electromagnetic waves are elliptically polarized. Figure 32 is showing the orientation of the electric field in two dimensions x and y. The total E-field is the vector sum of the $\overrightarrow{E_x}$ and the $\overrightarrow{E_y}$ vectors.

There are two special cases of elliptical polarization; linear polarization and circular polarization. A linearly polarized electromagnetic wave is comprised of a single electric component and the polarization is a fixed straight line. Linear polarization is further sub-divided into three types; vertical polarization, horizontal polarization and slant polarization. Vertical polarization is the one which travels orthogonal to the surface of the Earth and horizontal polarization travels parallel to the surface of the Earth.

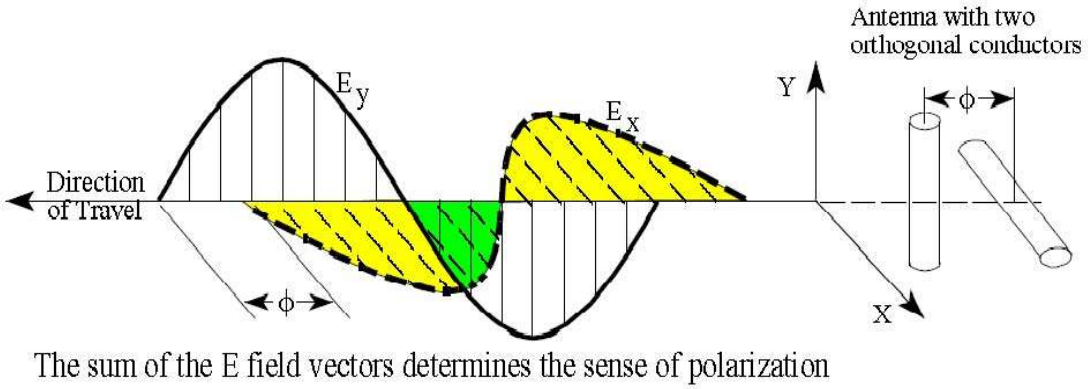

Figure 32: Polarization Coordinates [30].

A circularly polarized electromagnetic wave is the combination of two linearly polarized electromagnetic waves orthogonal to each other, having equal amplitude but being 90 degrees out of phase. Circular polarization is shown in Figure 33 below.

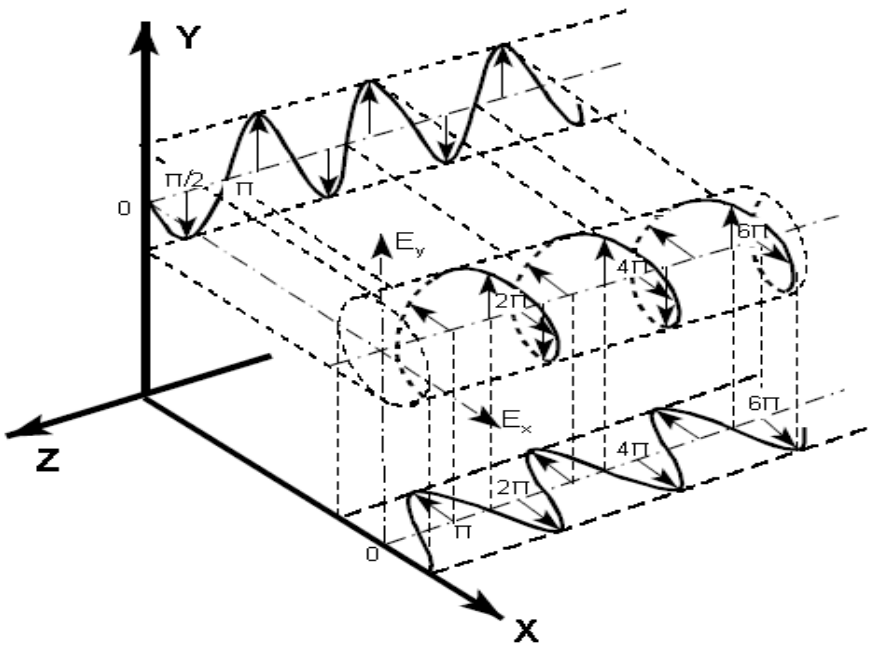

Figure 33: Circularly Polarized Electromagnetic Wave [30].

The axial ratio (*AR*) is the term used to describe the magnitude ratio of the two linearly polarized electric field components. In a circularly polarized wave the magnitude and axial ratio are equal, *1* or *0dB* (*10·log[AR]*) and in linearly polarized waves the axial ratio is infinite [27].

2.9 Input Impedance

Measurements of input impedance have been described in [7] and [3]. In [3] this is done by exciting a cylindrical dielectric resonator of permittivity *12*, radius *27.5mm* and height *26mm* with a coaxial probe. The probe is located at a distance of *14mm* from the center of the cylinder extending *20mm* into the resonator. The radius of the probe is *0.381mm* and the expected resonant frequency is *1.377GHz*. The location of feeding point indicates that the desired operating mode is the HE_{11} mode. The computed and measured impedance as a function of frequency is shown in Figure 34. The fields are obtained by assuming perfect magnetic walls on the boundary surfaces. The experimental resonant frequency is taken as that where the measured resistance is at maximum [7].

It is clear that resistance is maximal and reactance zero at resonance. In [7], the impact of the shape and excitation properties on the circuit characteristics is examined. The load impedance is measured and the frequency where resistance is maximal and reactance (close to) zero, is taken as the experimental resonance frequency. This frequency is then compared to the theoretical resonance frequency. A frequency dependence of the inductance causes the resistance peak and reactance null not to coincide at exactly the same frequency [7].

Measurements performed in [7] show that when the ratio between radius and height (*a/h*) of the cylindrical dielectric resonator is varying, the measured input impedance is deviating from the calculated value by maximum four per cent. For a radius of *3mm* and *a/h* ratios of *0.3*, *0.5*, *0.67* and *0.15*, the calculated (measured) resonance frequencies were (in *GHz*) *10.13* (*10.0*), *10.67* (*10.5*), *10.24* (*10.5*) and *9.90* (*10.0*), respectively. For the last aspect ratio, two modes are lying close together around *10GHz*, which distorts the peak of the resistance versus frequency curve.

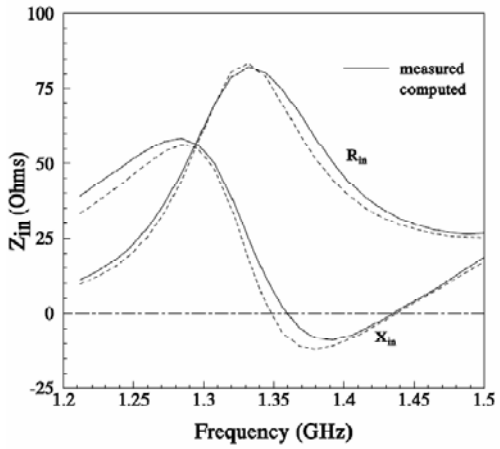

Figure 34: Measured and calculated input impedance of a cylindrical dielectric resonator with ε_r= *12*, radius= *27.5mm* and height= *26 mm* [3].

In [20], resonance and impedance are discussed for *a/h=0.5* and *a/h=1* with *a=12.83mm*. The probe excitation is made with a wire of radius *0.118mm* and the position of the feeding point is *9.62mm* from the cylinder base center point.

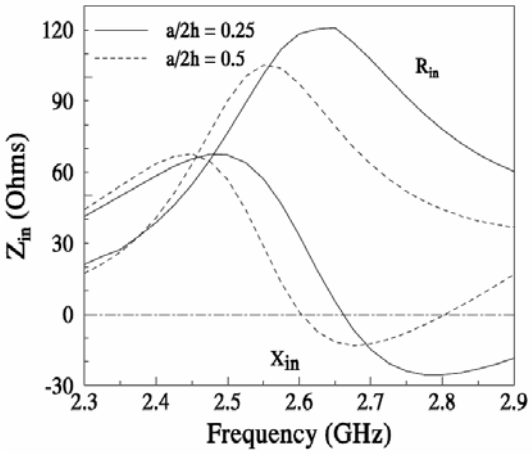

Figure 35: Measured input impedance of a cylindrical dielectric resonator with ε_r= *8.9*, radius=*12.83mm* and a/h=*0.5* and a/h=*1* [20].

The probe length was *12.5mm* and the relative permittivity was *8.9*. Results are shown in Figure 35. As the height increases, the resonant frequency decreases, in contrast to the conducting wire

antenna. This also indicates that not only radius, but also total volume decides the resonant frequency, which is also confirmed from FOAM© [23]. The input impedance in Figure 35 shows that also DRA dimensions can be used for tuning the circuit parameters of the DRA.

The effect of probe position was examined in [20] with relative permittivity *8.9*, radius *a=12.83mm* and aspect ratio *a/h=0.5*. The results in Figures 36 and 37 show the shift in the resonant frequency with probe position. The excited mode was in this case the HE_{11} mode. For small distances to the cylinder base center position the $TM_{01\delta}$ mode is also excited and is affecting the input impedance.

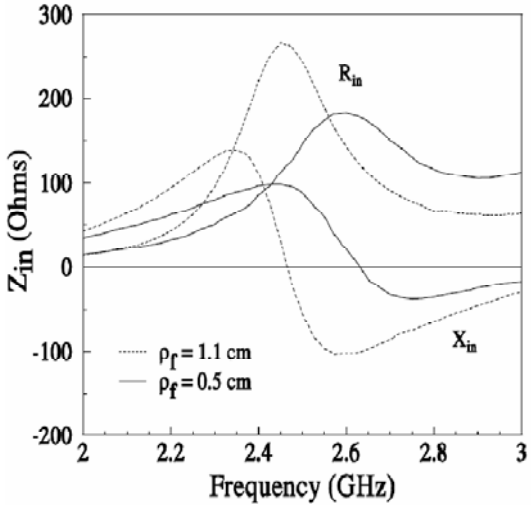

Figure 36: Measured input impedance of a cylindrical dielectric resonator with ε_r= *8.9*, radius= 12.83mm and a/h= *0.5* for two different excitation points [20].

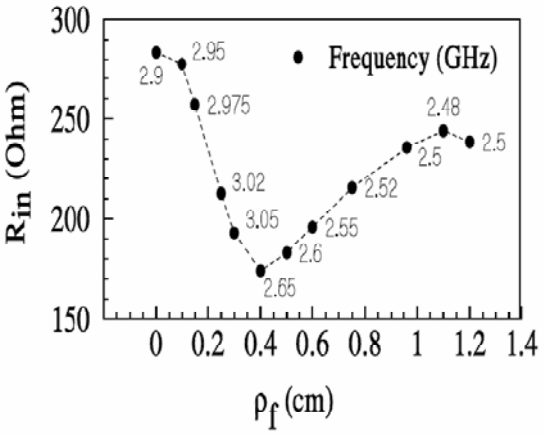

Figure 37: Measured peak resistance of a cylindrical dielectric resonator with ε_r= *8.9*, radius= *12.83mm* and a/h= *0.5* for varying feed position normalized to cylinder radius. The resonant frequency at each peak is also written near the points [20].

The effect of probe length was examined in [20] with relative permittivity *8.9*, radius *a=12.83mm* and *a/h=0.5*. The probe radius is *0.118mm* and the feeding position is *9.63mm* from the cylinder base center. The results are shown in Figures 38 and 39. The excited mode was in this case the HE_{11} mode. The probe length has two effects on the input impedance. As the probe length increases, the input resistance increases and this can be used for tuning. The second effect is the shift of resonant frequency. By choosing one peak resistance, i.e. one probe length, the resonant frequency can thus be adjusted. With a short probe length the deviation from the theoretical resonant frequency is smaller, but so are the coupling and possibilities for tuning.

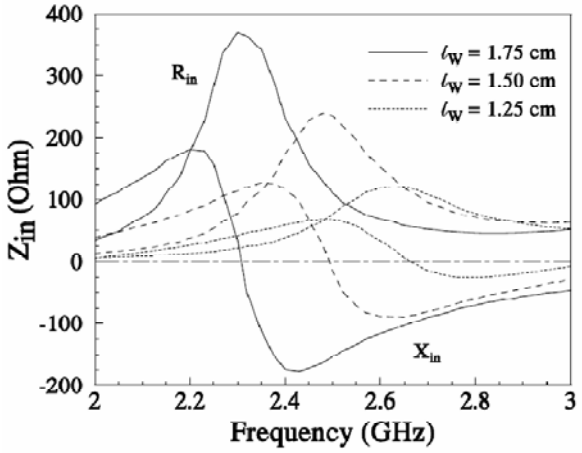

Figure 38: Measured input impedance of a cylindrical dielectric resonator with ε_r= *8.9*, radius= *12.83mm*, feed position *9.62mm* and a/h= *0.5* for varying excitation probe lengths [20].

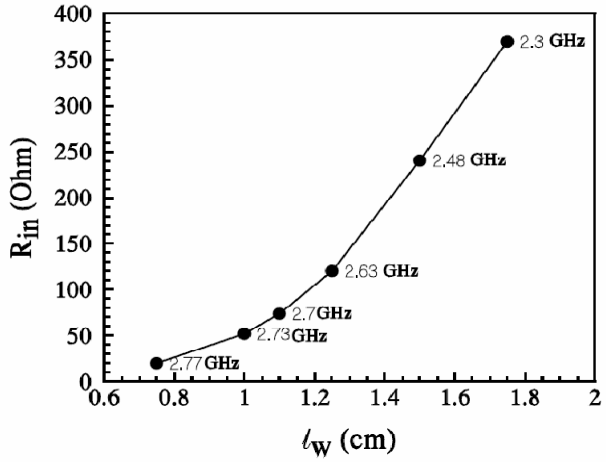

Figure 39: Measured peak resistance of a cylindrical dielectric resonator with ε_r= *8.9*, radius= *12.83mm*, feed position *9.62mm* and a/h= *0.5* for varying probe lengths. The resonant frequency at each peak is also written near the points [20].

The relative permittivity has also been investigated in the impedance study [20]. The parameters were radius *a=12.83mm*, *a/h=0.*5, probe wire radius *0.118mm*, feed position *0.962mm* from the cylinder base center and probe length *15mm*. The investigated permittivity ranged from *7* to *12*. The results are in Figure 40. As expected, the resonant frequency decreases with higher relative permittivity. This is due to a smaller dielectric wavelength for the original resonant frequency and

a larger wavelength is needed to obtain the same number of nodes for a particular mode in the cylinder. The resonant frequency cannot be linearly scaled by the square root of the relative permittivity, though [20].

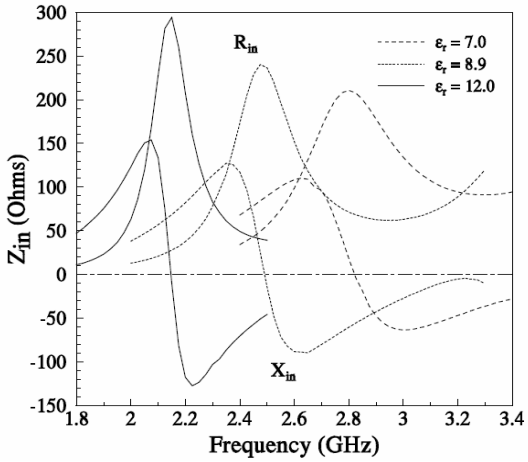

Figure 40: Measured input impedance of a cylindrical dielectric resonator with ε_r= *7, 8* and *12*, respectively and radius= *12.83mm* and a/h= *0.5*. [20].

CHAPTER 3

METHODOLOGY

3.1 Decision of Shape

The dielectric resonator antenna can have many different shapes as described in section 2.5. Depending on the mode of operation and performance of a DRA, the desired shape can be selected to fulfill the requirement. Many different shapes have been tried experimentally, e.g. half cylindrical, hemispherical, semi-conical, pyramid, and truncated triangular as shown in Figure 41.

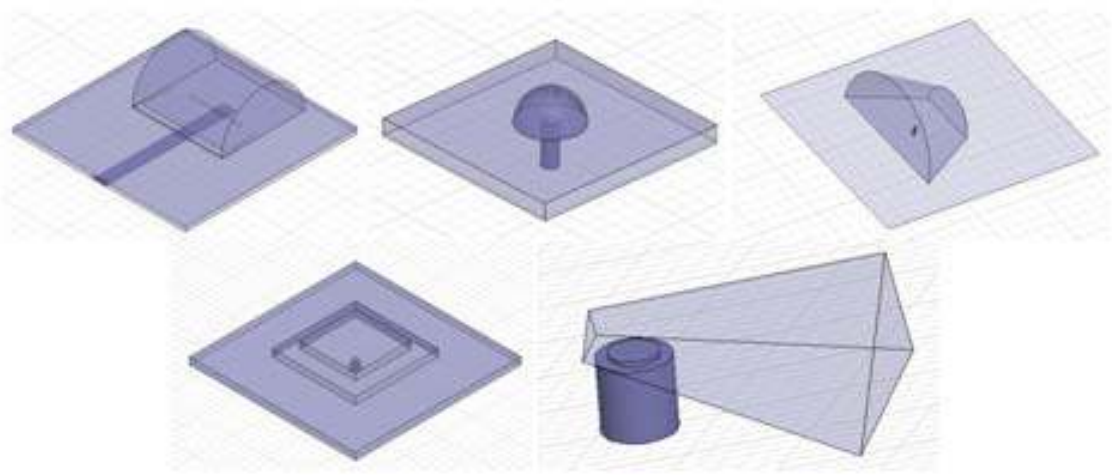

Figure 41: Different experimented shapes of dielectric resonator antennas.

Many designs were studied but none of the above mentioned shapes fulfilled the requirements.

The problem formulation clearly depicts the wish for a dual polarized antenna. In the case of a dielectric resonator antenna, this could be achieved by somehow combining two dielectric resonators which have different geometrical orientation or size with respect to each other. The excitation of such an antenna could be more complicated, see Figure 42**.**

Another way of obtaining dual polarization could be to excite two modes at the same frequency in one resonator. These two modes could either be two degenerative modes which analytically have the same resonant frequency, or the antenna element could be manipulated in some way in order to make two modes coincide in frequency. The excitation method in detail is described below in the report.

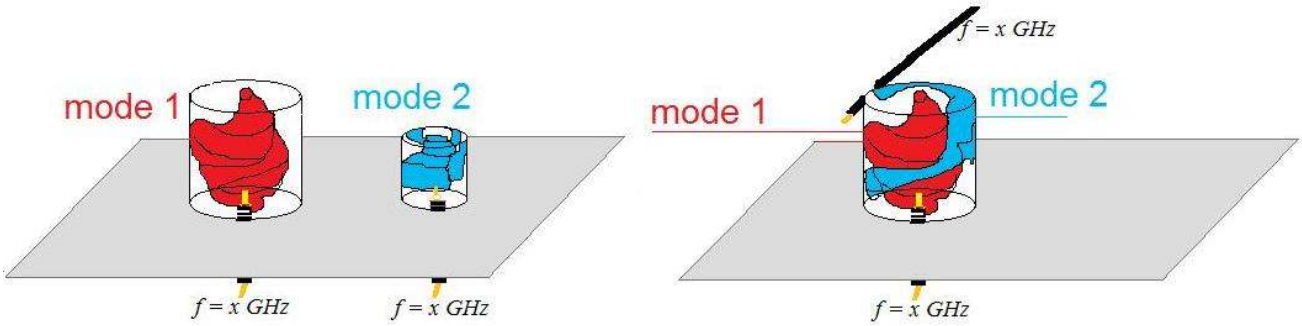

Figure 42: A dual polarized dielectric resonator antenna can be realized by separating resonators from each mode (left) or by two modes on the same resonant frequency with orthogonal field distributions (right).

The latter alternative has been successfully performed where two radiating modes and one filtering narrowband mode are operating on the same frequency band [12], [28].

This multi-mode function requires individual excitation of each mode. Thus a combination of microstrip, slot, coaxial probe or other excitation techniques must be implemented simultaneously. In [12] this was done by a combination of microstrip and coaxial feedlines.

The objective is to create one omni-directional radiating dielectric resonator antenna element and one broadside radiating dielectric resonator antenna element. The radiation pattern is determined by the shape of the resonator and the mode which is excited. For a cylindrical dielectric resonator, two low omni-directional modes are the TE_{01} and TM_{01} modes. These radiate like short magnetic and electric dipoles oriented along the longitudinal axis, respectively. The cylindrical shape is a body of revolution, symmetrical along the longitudinal axis, which makes it neutral to excite from any azimuth angle.

The cylindrical shape is the simplest shape for a body of revolution and its modes have a simple mathematical description with explicit analytical formulas in the case of a shielded cylindrical cavity. Many exotic shapes of dielectric resonator antennas have evolved from the desire to lower the effective relative permittivity of the material used in the resonator. Such antennas are e.g. the notched rectangular dielectric resonator and the cylindrical-ring dielectric resonator. The reason for using low permittivities is the desire for high bandwidth, see section 2.3.11. By using a simple basic shape together with a lower relative permittivity, these complicated shapes can be omitted. Considering the transverse modes, there are thus fields with increasing numbers of radial and azimuthal variations that can resonate, which enables a clear perception of possible field distributions and excitation locations.

Another argument for settling with the cylindrical dielectric resonator was its common use for microwave circuit components, the documentation of the use, the excitation of different modes, the impedance characteristics as well as fabrication issues.

3.2 Omni-directional Dielectric Resonator Antenna Design

In this part, the methodology for designing and manufacturing an antenna with an omni-directional radiation pattern for operation between *2.4GHz – 2.7GHz* is described step by step. The required performance characteristics are restated below in Table 3.1.

Parameter	Requirement
Frequency	2400 – 2700 MHz
Return loss	> 15 dB
Antenna port isolation	> 15 dB
Efficiency	> 90 % (> -0.45 dB)
Connector	SMA (female)

Table 0.1: Parameters for the performance characteristics of the omni-directional antenna.

3.2.1 Excitation techniques

The azimuthal independence of the electric field of the TE_{01} mode and the magnetic field of the TM_{01} mode makes the two modes appropriate for excitation with electric and magnetic currents respectively, going around the center longitudinal axis. A straightforward method for exciting the TE_{01} mode is by a stripline, since the dielectric resonator is located on a substrate above a ground plane. This stripline can to a varying extent follow the curvature of the sidewalls and its exact design will turn out to be an important matching parameter. The TM_{01} mode is easily excited by an electric current along the longitudinal axis, which can be realized by a probe extension from a coaxial cable as shown in Figure 43.

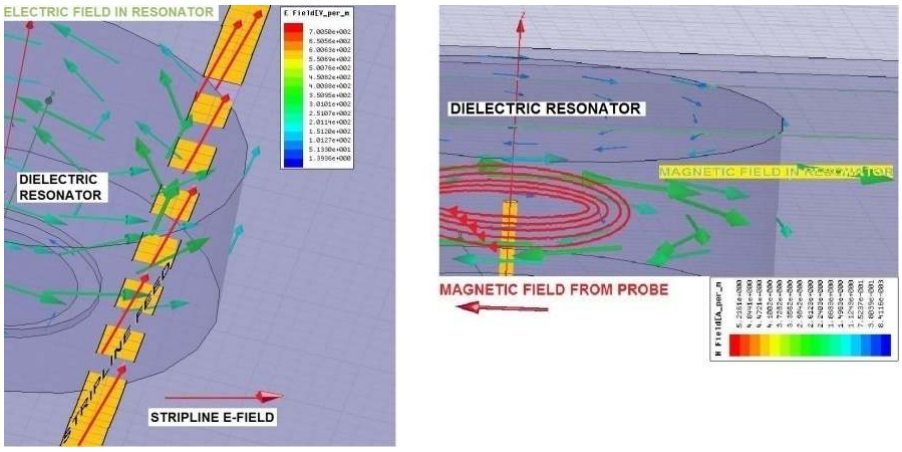

Figure 43: Excitation of the TE_{01} mode by stripline (left) and the excitation of the TM_{01} mode by probe (right).

Excitation of the TE_{01} mode can be done by a microstrip line parallel to the transverse plane of the resonator (left). The excitation of the TM_{01} mode is made by a magnetic field from an electric cable along the center longitudinal axis of the cylindrical dielectric resonator (right).

An alternative way of exciting the TM_{01} mode is the use of a slot, with a principal sketch shown in Figure 44. The TE_{01} mode is excited by the stripline going on top of a dielectric substrate to the right. The strength of the coupling is determined by the closeness of the stripline. One possible implementation of this technique in practice would require a double dielectric substrate layer on each side of the ground plane. The slot is on a ground plane below the dielectric resonator which is placed in the center of the resonator with the aim of leakage of the electric field and it is directed from the stripline beneath the dielectric sandwich up to the ground plane on the top. However, Figure 44 only shows a general sketch of the possibility to excite the TM_{01} mode with a slot. In reality the implementation would be complicated since the ground plane needs to be symmetric and the other feed, the stripline for the TE_{01} mode, is reversely placed on the dielectric substrate.

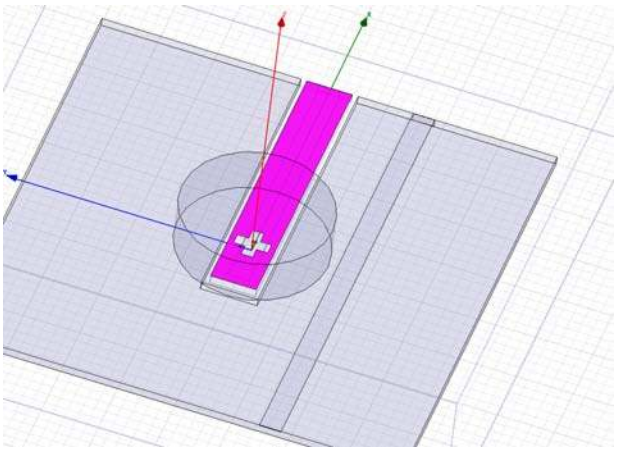

Figure 44: Excitation of the TM_{01} mode by a slot located at the center of the resonator base.

In [12] and [28] the magnetic field excitation of the TM_{01} mode is made by a coaxial cable touching the center of the lower base surface of the resonator. No penetration is made by a probe to avoid high cross coupling and destruction of the field distribution of the TE_{01} mode. The effect of the coaxial cable is instead enhanced by a circular disc on the base of the resonator, which increases the area on which the longitudinally oriented electric field is present.

The TE_{01} and TM_{01} modes are also, with exception for the TE_{11} mode, the two lowest modes, meaning that they have the lowest resonant frequencies. If the resonator is considered as a dielectric waveguide, the cut-off frequencies of the higher modes will not be attained if the resonator is excited at the resonant frequency of the lowest modes. The TE_{01} mode is to prefer instead of the TE_{11} mode since the latter has an azimuthal variation and thereby the radiation pattern is not donut-shaped.

3.2.2 Choosing parameters

The initial problem with defining the design parameters of a cylindrical shape (or any arbitrary shape for that matter) is to have a proper model for predicting the resonant modes. As discussed in section 2.5.1 the three main alternatives, namely the analytical formulas in equation 2.25 of a shielded dielectric cavity, their numerical approximation for an unshielded cavity which are given in equations 2.19 and 2.21 as well as the computer program FOAM©, all have the same asymptotic behavior of $(1/h^2)$, h denoting the height, which shows that they all originate from the resonance cavities.

In the first stage the resonant frequency is approximated by the numerical formulas in equations 2.19 and 2.21 which give a rough estimation of size, permittivity and resonant frequency. However, the simulation results in terms of *S*-parameters are deviating by more than *10%* to *15%.* The need for a more exact model becomes apparent when trying to excite two modes at one frequency, something which for a regular hollow waveguide is only possible for degenerative modes. In this case, the need to plot the resonant frequency versus dimension parameters comes from a desire of finding an intersection between two curves at one specific size for one specific relative permittivity.

A plot of the numerical formulas in equations 2.19 and 2.21 shows that their curves may intersect if the aspect ratio is high. This is shown in Figure 45. The numerical formulas which give the TE_{01} and TM_{01} resonant frequencies have an intersection before they decay asymptotically as $(1/h^2)$. However, the analytical resonance cavity formula in equation 2.25 shows that the curves are only approaching each other asymptotically. For simplification expression (2.25) is shown again

$$f_0 = \frac{1}{2\pi\sqrt{\mu_0\varepsilon_0\varepsilon_r}}\left[\left(\frac{\xi_{01}}{a}\right)^2 + \left(\frac{\pi}{2h}\right)^2\right]^{1/2}. \qquad (2.25)$$

As before, ξ_{01} denotes the first zero of the zeroth Bessel function or its derivative, depending on if the mode is TM_{01} or $TE_{01.}$ It is clear that for a fixed radius of the resonator, the frequency versus height curves is scaled along the y-axis when varying the relative permittivity $\varepsilon_{r.}$ No intersection takes place because of the monotone decrease with increasing cylinder height *h.*

In Figure 45, the radius is *19.22mm* and the height is varying from *1mm* to *4mm*. For one particular permittivity, the TE_{01} and TM_{01} frequency curves have the same color. The intersections for each permittivity are marked by circles. The dimensions and permittivity of these intersections are then modeled in Ansoft HFSS.

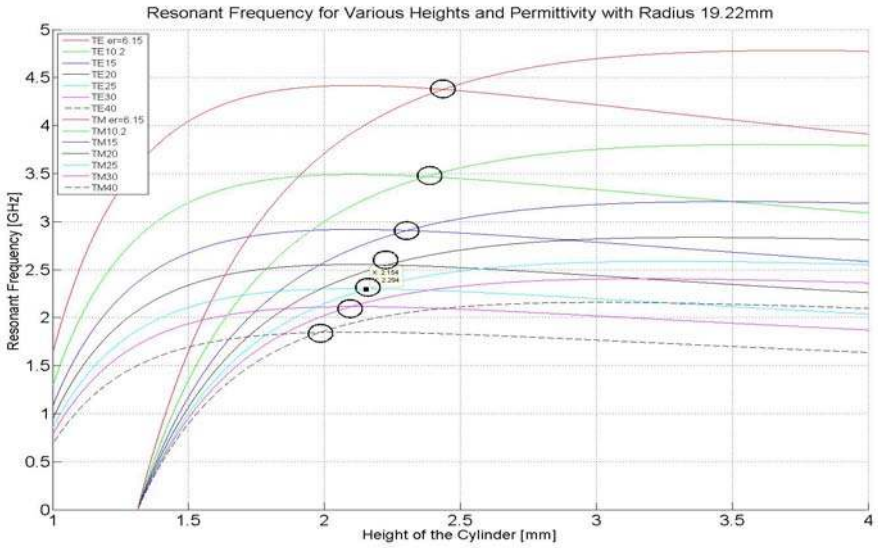

Figure 45: A plot of the resonant frequency curves for decreasing aspect ratio (radius/(2*height)) from the numerical models (2.19) and (2.21). TE_{01} and TM_{01} curves with the same color correspond to one permittivity.

In Figure 45, one intersection takes place for a permittivity of *25* and a height of *2.154mm*. The model made in Ansoft HFSS has the design shown in Figure 46.

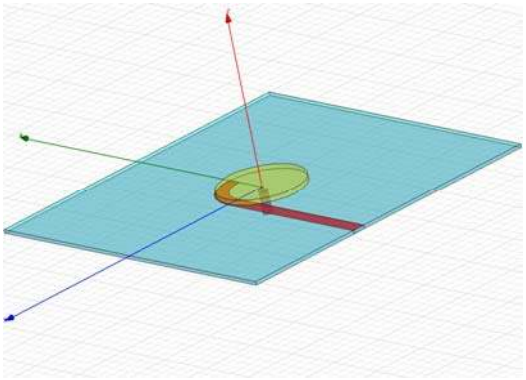

Figure 46: The cylinder from the intersection for permittivity *25* from Figure 45. The aspect ratio is high and the excitation is, as always, by coaxial cable and microstrip line. The feedlines are marked with red.

In Figure 47, the reflection coefficients (S11 and S22) are shown below for the two modes.

The TE_{01} resonance is at *5.31GHz* and the TM_{01} resonance is at *5.5GHz*. This is verified by a check on the field distribution and the Smith chart. They are coinciding but not at *2.3GHz* as predicted in Figure 45. FOAM© gives a TE_{01} resonance at *5.45GHz* and no solution for the TM_{01} mode (because of the small variation in height). The analytical shielded resonance cavity formula in equation 2.25 gives a TE_{01} resonance around *20GHz* which again demonstrates the accuracy of the FOAM© model. In the same way the intersection for a relative permittivity of *15* with the same radius gives the reflection diagram in Figure 48.

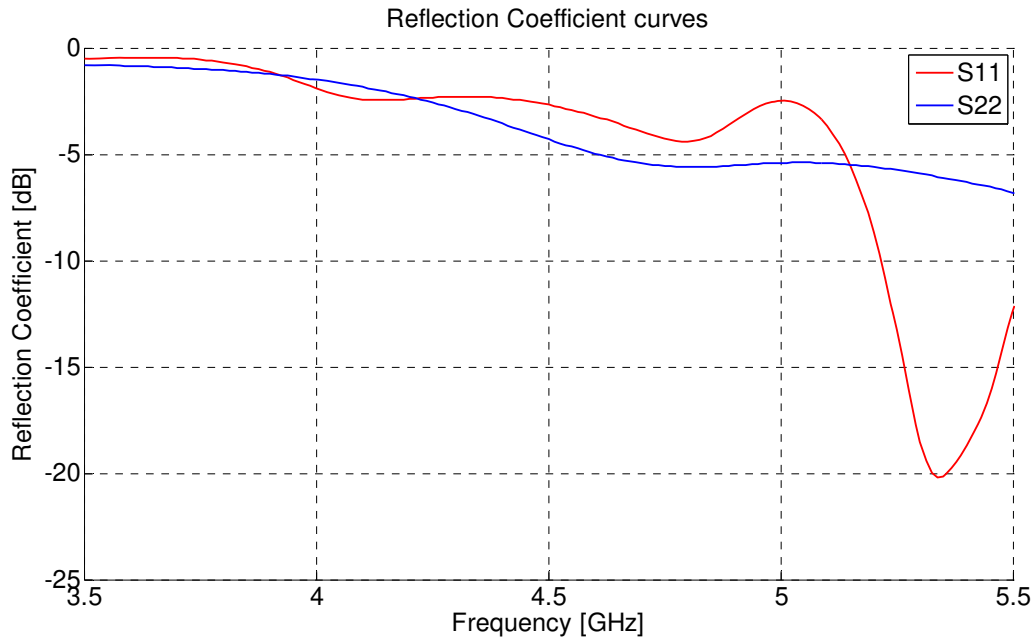

Figure 47: Reflection diagram for the cylinder from the intersection for permittivity *25* from Figure 45. The red curve is the microstrip excitation reflection coefficient (*S11*) and the dark curve is the coaxial cable reflection coefficient (*S22*). The two deepest dips belong to the TE_{01} and TM_{01} mode respectively. The resonances do coincide, but not at the frequency predicted in Figure 45.

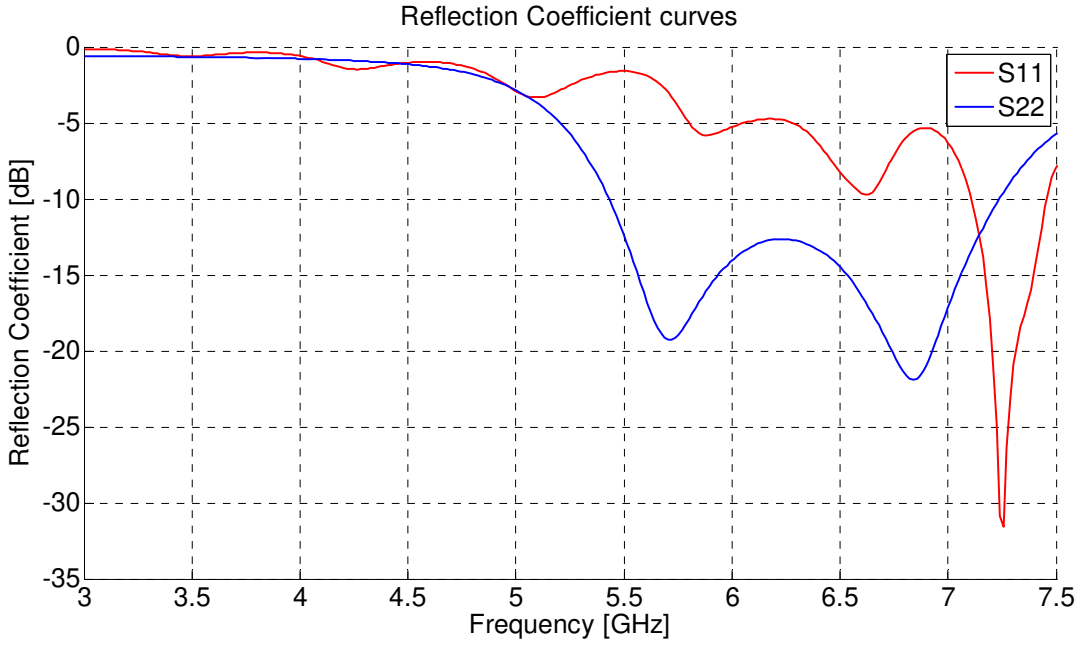

Figure 48: Reflection diagram for the cylinder from the intersection for permittivity *15* from Figure 45. The red curve is the microstrip excitation reflection coefficient (*S11*) and the dark curve is the coaxial cable reflection coefficient (*S22*). The three deepest dips belong to the TE_{01} and TM_{01} (double dip) mode. The resonances do coincide, but not at the frequency predicted in Figure 45.

A cross-check with the Smith chart and field distributions again shows that the two deepest dips correspond to the TE_{01} and TM_{01} (double dip) modes. Again, the TM_{01} mode is several times more wideband than the TE_{01} mode. The resonant frequencies are again far above the predicted *3.13GHz*.

This method does not always work, for permittivity *25* and radius *11.22mm*, for example, the modes are not coinciding by applying this method; the TM_{01} resonance comes at *6GHz* and the TE_{01} resonance is at *7.2GHz*. Another drawback is that the prediction made in MATLAB deviates by more than *100%*. Usage of this method would require scaling of the dimensions or permittivity and it would all come down to a trial and error process. This scaling would also require relatively high dimensions. An attempt to scale the cylinder dimensions (radius and height) in Figure 46 by a factor of two (a frequency decrease by the same factor from *5.3GHz to 2.65GHz*), has neither any TE_{01} resonance between *1GHz* and *6GHz* in Ansoft HFSS nor does FOAM© return any solution. The same holds if instead the bottom area and height are scaled by a factor two. If however this second scaling is modified so that the height is decreased by an additional *1mm*, the modes coincide at *3.8GHz*. The diameter is around *53mm* for that cylinder.

The last paragraph shows the potential with the numerical model in using a simple cylinder for dual polarization but it relies on arbitrariness and luck. Possibly, the model might work if improved. It is neither the solution that gives the most compact size of the resonator.

In the beginning of the investigation, the importance of keeping a high aspect ratio (radius/height) became apparent, when simulations of a resonator with permittivity *6.15* gave high return loss around *3GHz*. The degree of freedom was set to be the height and the radius kept small, at *10mm*. In order to decrease the frequency, by stepwise modification, the return loss characteristics turned out to be very satisfying at an aspect ratio of *(a/h)=(1.805/80)*, with a picture of such a model in Figure 49.

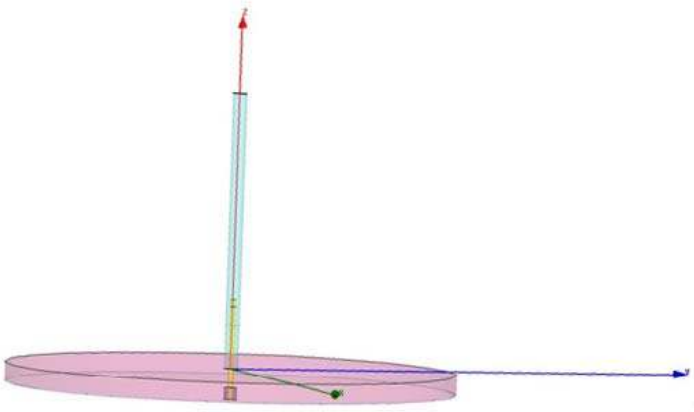

Figure 49: The resonator radius is *1.805 mm* and the height is *72.2mm*.The circular ground plane is placed below a cylindrical substrate of relative permittivity *2.2* and thickness *5mm*.

The reflection diagram of this structure is shown in Figure 50.

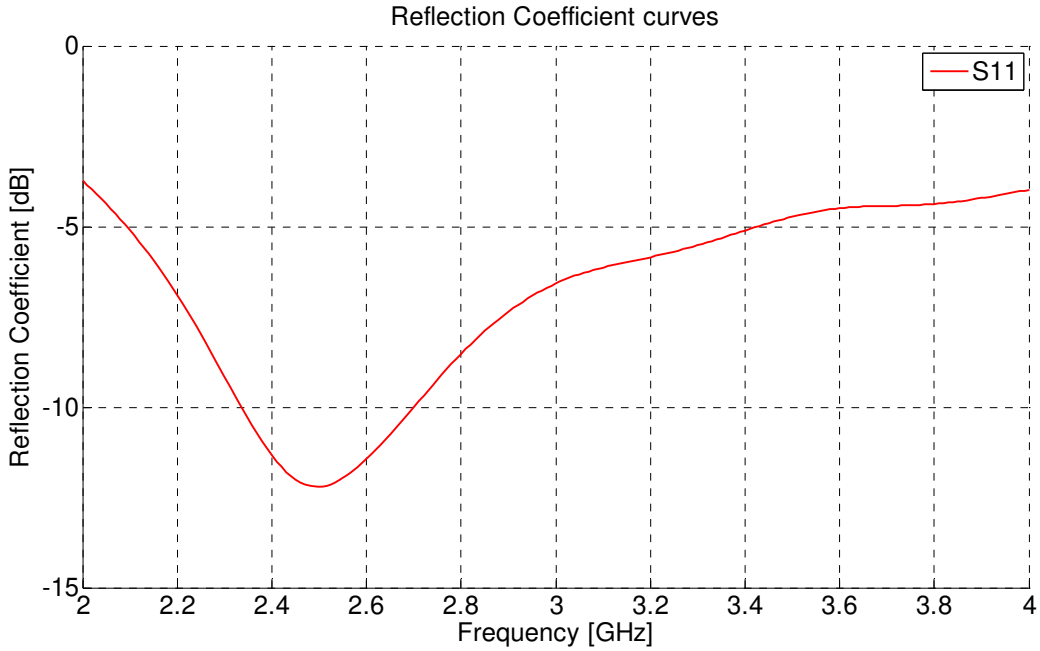

Figure 50: The reflection coefficient of the dielectric structure in Figure 45. The result shows a satisfying bandwidth.

However, this is not the result of a resonating mode but rather a loaded dielectric monopole. This is confirmed by the characteristics of the radiation pattern, which is not shown here. In most reports, the aspect ratio is kept such that the radius is larger than the height for a cylindrical dielectric resonator.

In general it is not as straightforward as only to scale the dimensions with $\sqrt{\varepsilon_r}$ in order to adjust the resonant frequency. A main step forward is made by the acquisition of the FOAM© software [23]. This turns out to be a precise tool in predicting the resonant frequencies and is accurate within *200MHz* in the *2GHz* region. The model is based on a shielded cylindrical dielectric resonator located on a dielectric substrate. The available parameters to be set are the substrate permittivity and thickness, the resonator permittivity, radius and height as well as the distance to the metallic lid above the resonator and the permittivity outside the resonator. The outputs are the resonant frequencies of the 16 lowest modes that can be excited in a cylindrical dielectric resonator located on a dielectric substrate. The TE_{11} mode is not in this list of modes, for example. FOAM© stands for *Frequency of All the Modes*. An illustration of the program is shown in Figure 51.

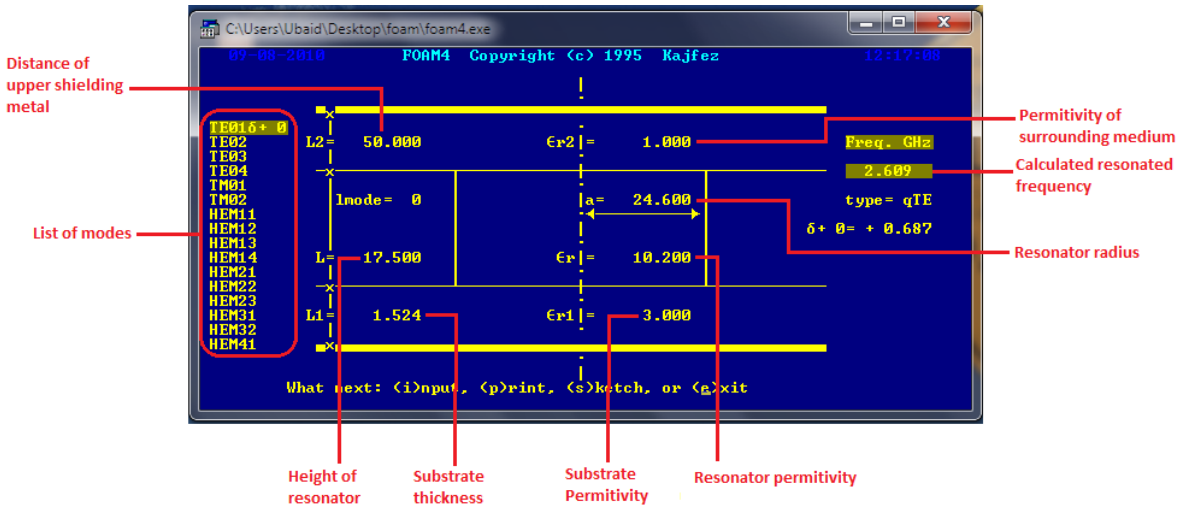

Figure 51: User interface of the FOAM© software [23].

For antenna applications, the distance to the upper shielding metal is set to be *60mm*, which will turn out to be several times the resonator height. The distance to the lower metal plate is the distance to the ground, which is the substrate thickness. The dielectric substrate plane is infinitely large and the shape of the resonator is cylindrical. Nevertheless, the highest accuracy is obtained for small distances between the resonator and the metallic plates [25]. Also affecting the accuracy of the algorithm of this software is the height of the cylinder relative to the thickness of the substrate. According to [25] the open resonators are modeled by setting the distance to the upper plate *L2* as at least three times *L*, the height of the resonator.

A small circumference of the cylinder implies a change of the parameter *lmode*, which denotes the number of half-wave variations in the longitudinal direction. This is generally kept as zero but for the structure in Figure 49, the number of variations needs to be larger in order to have a wavelength acceptable for the small circular base. In this case, for an *lmode* index of 10, the TE_{01} resonant frequency is around *29GHz*, which shows the importance of a larger radius for lower frequencies (small radius can not only be compensated with height) and it shows that the low reflection coefficient in Figure 50, is due to a loaded monopole effect.

The next step in deciding the geometrical and material parameters of the dielectric resonator is to plot the resonant frequencies of the TE_{01} and TM_{01} modes as a function of dimensions for several permittivities. This is done for two reasons. First to find the appropriate dimensions for a resonance around *2.5GHz* and second to see where the difference in resonant frequency between the two modes is the smallest.

The answer to the first question is dependent on the permittivity used. The relative permittivities that were tried out were between *15* and *30*. For these permittivities, the radius of the resonator should be between one and two inches. The reason for considering permittivities in this range is the matter of size. A size no larger than one inch is desired for compactness. Also, the availability

of dielectric materials with permittivities of *15*, *20*, *25* and *30* is satisfactory. The suitable suppliers at this stage are the Cumming Microwave Corporation and TransTech Incorporated.

The answer to the second question is that for all calculated dimensions and permittivities, the difference in resonant frequency between the modes is around *700MHz*, with little variation. The FOAM© software returns no available solution for the TM_{01} resonant frequency for the small aspect ratios for which there is an intersection with the method used in Figure 45.

It is obvious that some kind of manipulation of the dielectric needs to be done for frequency trimming. The key lies in understanding the field distributions and their dependence on the space coordinates. In Figure 52, the field distributions of the TM_{01} and TE_{01} modes in a cylindrical resonator are shown as well as the *z*-dependence of some components.

The TM_{01} electric field is as that of a half wave electric dipole. The longitudinal component of the E-field, $\overrightarrow{E_z}$, is at the bottom of the resonator the only E-field component. However, as can be seen in Figure 52, it becomes smaller as the radial component of the same field becomes the dominant one with increasing *z*.

The consequence from this *z*-dependence of the electric field is that the coupling from a probe is more efficient at the bottom, since the probe is directed in the *z*-direction.

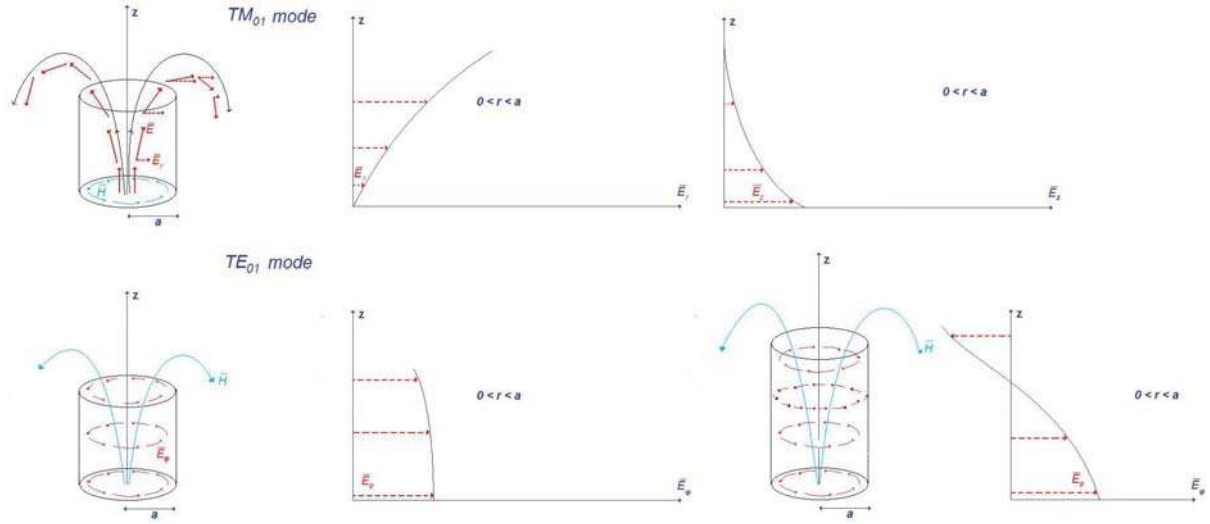

Figure 52: The *z*-dependence of the E-field component that is object to excitation from a probe (above) and a microstrip (below). The longitudinal E-field component decays to zero close to the top of the cylinder and the coupling to this component is more efficient at the bottom. For the TE_{01} mode, the azimuthal component varies slower with z and is not dramatically changed by a cut-out at the bottom. A frequency shift is expected for both modes because of the change of shape and volume, but with different degrees of change for the TE_{01} and TM_{01} modes.

The main point is now, that by removing parts of the bottom area of the cylinder, e.g. by making a lower cylinder with a radius smaller than the original one and in that way creating a mushroom-like cylinder constellation, the coupling to the TM_{01} mode from the center probe will be affected and the frequency will shift, since the main coupling is in the lower cylinder. The decrease in

total dielectric volume guarantees increased frequency. The TE_{01} mode, which is purely azimuthal, has a slower longitudinal dependence for its $\overrightarrow{\boldsymbol{E}_{\boldsymbol{\varphi}}}$-component. It means that the coupling to this mode from a microstrip on the underlying substrate will be less affected. It is for a small aspect ratio that the number of half wave variations in the longitudinal direction is larger than one.

The creation of a mushroom would theoretically shift the resonant frequency up for both modes but the TM_{01} mode would be affected to a larger extent for the reasons mentioned above. Since the TM_{01} mode is generally above the TE_{01} mode in terms of resonant frequency according to calculations with FOAM©, see Figures 18 and 19, the aim is to create a modified cylinder so that these two resonating modes meet on one frequency.

An interesting remark is that the FOAM© software gives the TM_{01} mode resonant frequencies above the corresponding TE_{01} modes, whilst formula in equation 2.25 implies that the TE_{01} modes should have higher resonant frequencies because the first zero of the zeroth Bessel function is smaller than the first zero of the derivative of the zeroth Bessel function, which is visible in Figures 15 and 16. Also see the Appendix for Bessel functions with tables.

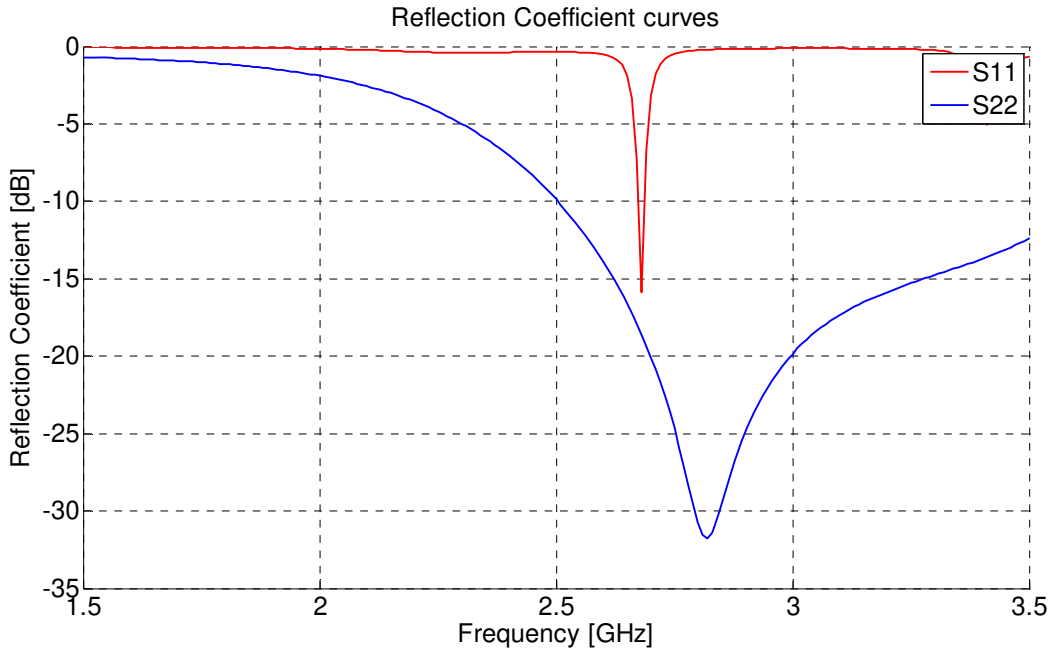

Figure 53: : Reflection diagram for the modified two-cylinder structure with radii *4.53mm* and *12.7mm*, respectively and heights *2.5mm* and *14.7mm*, respectively. A smaller bottom cylinder implies a remarkable frequency shift towards lower frequencies for the TM_{01} mode (dark curve) whereas TE_{01} mode (red curve) does not shift dramatically.

A first mushroom-like design is made with the desire of keeping the dimensions of the resonator below one inch. A cylinder of relative permittivity *22*, radius *12.7mm* and height *17.2mm* has, according to FOAM©, a TE_{01} resonance at *2.647GHz* and a TM_{01} resonance of *3.509GHz*. The Ansoft HFSS simulation fed by a *50Ω* microstrip line and a *50Ω* coaxial cable gives a TE_{01} resonance at *2.59GHz* and a TM_{01} resonance at *3.1GHz*, respectively.

The cylinder is now cut into a combination of a lower cylinder with radius *4.53mm* and height *2.5mm* on top of which is a cylinder of radius *12.7mm* and height *14.7mm*, so that the sum of the two heights is the same as that of the original cylinder. The reflection coefficient (S11 and S22) of this cylinder are shown in Figure 53.

The modified cylinder has a TE_{01} resonance at *2.68GHz* and a TM_{01} resonance at *2.82GHz* according to Ansoft HFSS. The TE_{01} mode has shifted slightly up in frequency while the TM_{01} mode has moved down by *300MHz*. The unexpected is that the TM_{01} mode moves *down* in frequency, but as expected this mode is subject to a more dramatic change.

As can be seen from Figure 53, the TE_{01} resonance is quite narrowband, with a *-10dB* bandwidth of around *10MHz*. The aim for higher bandwidths is thus a challenge.

In the literature [25], the TE_{01} mode has been successfully implemented as a filtering mode. This mode has a high *Q*-factor compared to the wideband TM_{01} mode, see Figures 54 and 55. Since the *Q*-factor is inversely proportional to bandwidth, the TE_{01} mode is in theory more narrowband. On the other hand, the *Q*-factor is proportional to the relative permittivity; see section 2.3.11, which means that a lower permittivity would imply a higher bandwidth for all modes.

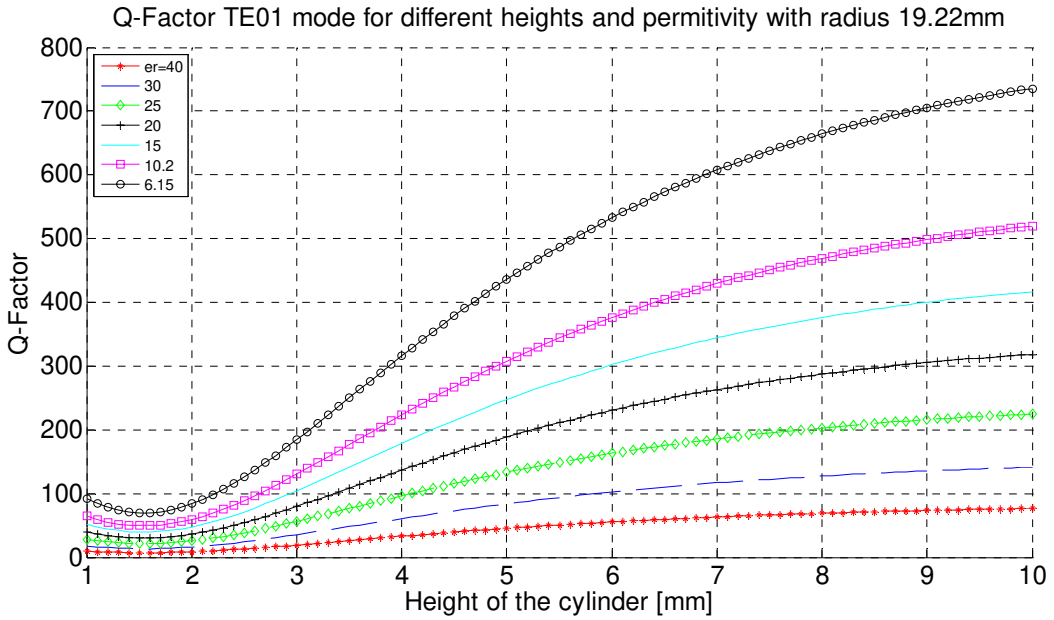

Figure 54: Plot of the *Q*-factor for the TE_{01} mode for a cylinder of radius *19.22mm* with varying height and relative permittivity.

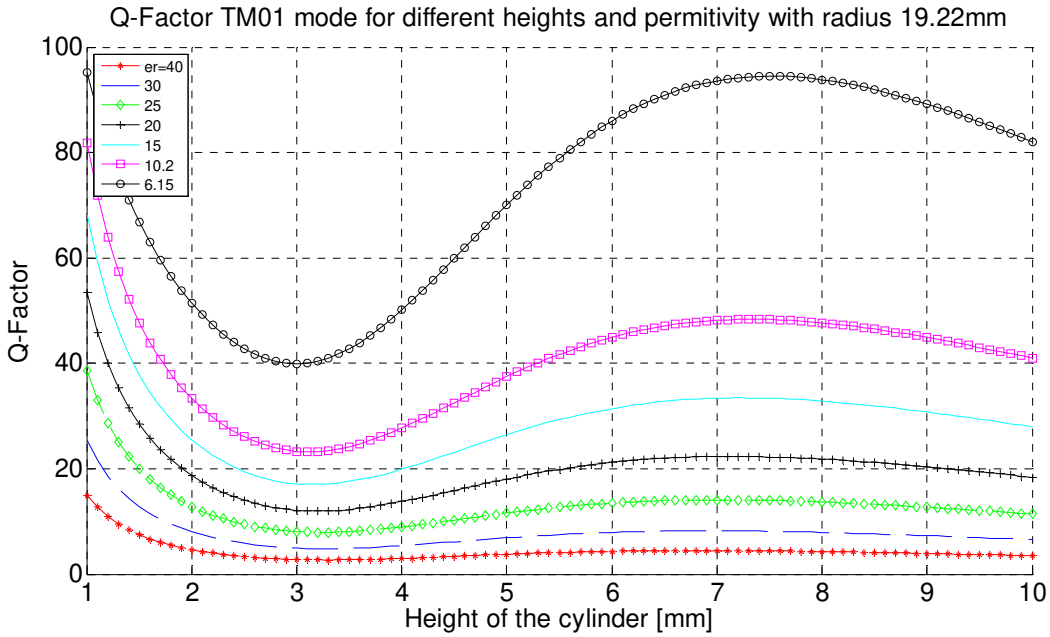

Figure 55: Plot of the *Q*-factor for the TM_{01} mode for a cylinder of radius *19.22mm* with varying height and relative permittivity.

As discussed in section 2.3.11, dielectric materials of permittivities above *20* are available for dielectric resonators. One import company providing materials from Cumming Microwave has for example only permittivities above *20* available for orders. These materials can be ordered as rods of radii below one inch. For lower permittivities, the main provider is Rogers Corporation who has PTFE and ceramic dielectric sheets with relative permittivity from *1* to *10.2*. As the dimensions are considered to be a critical point, a simulation is run with permittivity *10.2*. These sheets come in a variety of thicknesses with *2.5mm* as the maximum. It turns out that a cylinder with this permittivity and radius of one inch and height *18mm* would have a TE_{01} resonance at *2.53GHz* and a TM_{01} resonance at *3.2GHz*, according to FOAM©. This structure is the starting point in the next phase of the project and is shown in Figures 56 and 57.

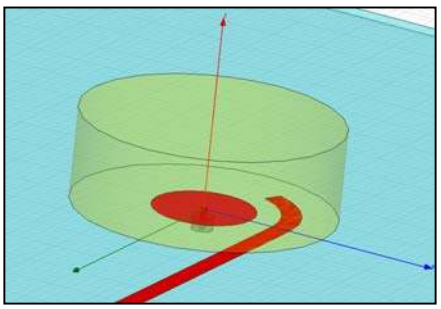

Figure 56: The solid cylinder of permittivity *10.2*. The feeding is made by a microstrip and a probe from a coaxial cable ended by a circular disc.

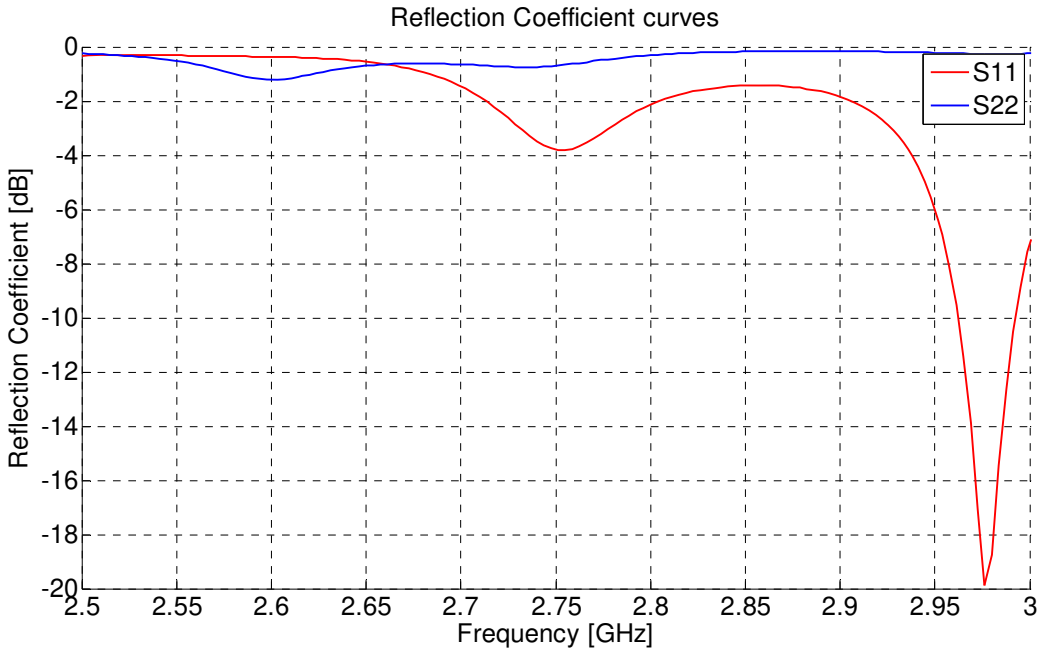

Figure 57: Reflection diagram for the cylinder in Figure 56. The red curve corresponds to the microstrip feeding (*S11*) and the dark curve to the coaxial feeding (*S22*). The wideband TM_{01} resonance is ill-matched and centered around *2.65GHz*. The TE_{01} resonance is around *2.82GHz*.

The challenge is to remove some of the volume from the lower parts of the cylinder in such a way so that the TM_{01} mode moves down in frequency and the TE_{01} mode is minutely changed.

At this stage, the probe is not entering the actual resonator, to avoid the feared interference between the probe and the TE_{01} field distribution. The heritage from previous simulations with higher permittivities was the dimensions with radii of one inch and one half inch in which rods from Cumming Microwave are available.

These standard dimensions were kept for the Rogers materials of permittivity *10.2*. Please note that a relative permittivity of *10.2* requires two times the radius of permittivity *22*.

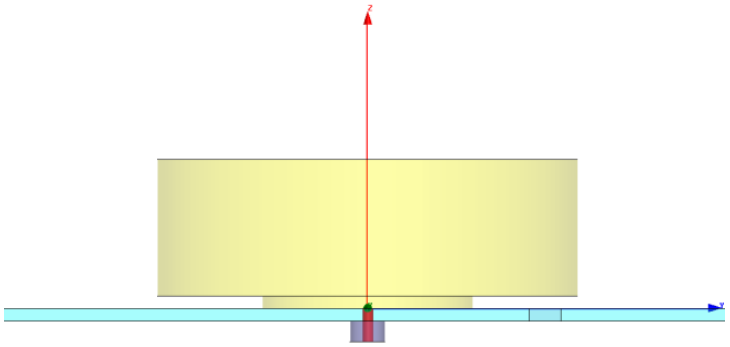

Figure 58: The modified cylinder of permittivity *10.2*. The airgap between the microstrip and the resonator results in a weaker coupling. The microstrip cannot be too close to the coaxial feeding because of the risk of high cross coupling.

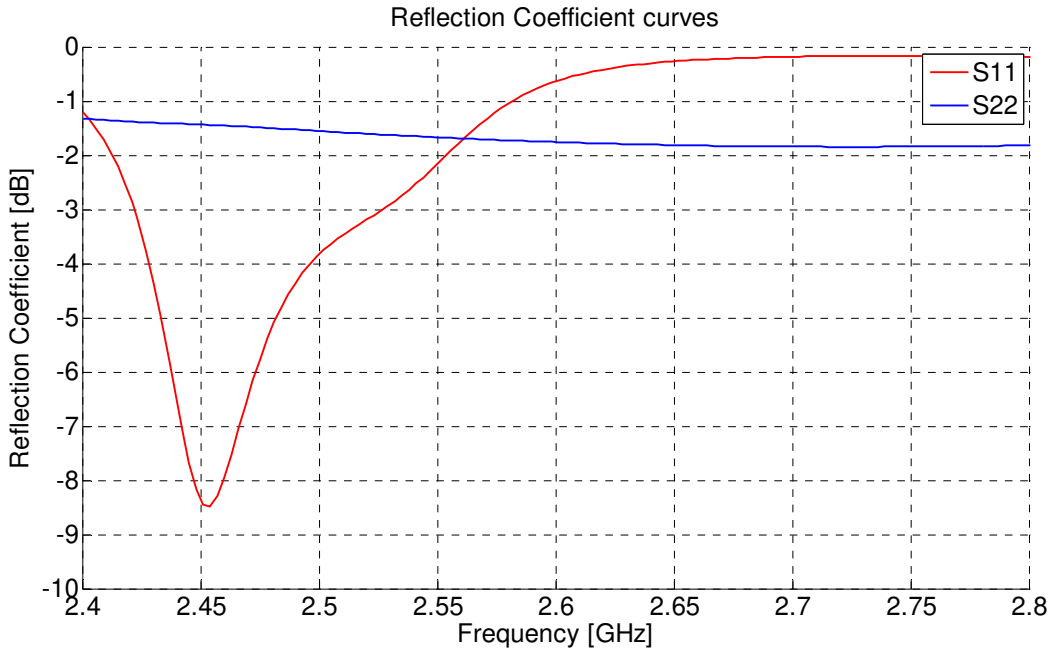

Figure 59: Reflection diagram for the modified cylinder in Figure 58. The red curve corresponds to the microstrip feeding and the dark curve to the coaxial feeding. The TE_{01} reflection coefficient is higher with the air spacing between the microstrip and the resonator than in Figure 57.

The cylinder in Figure 56 is now on the bottom end replaced by a cylinder with radius *12.7* (one half inch) and height *1.5mm*. The modes are moving closer but with two problems. First the TE_{01} mode is still narrowband and second, the reflection coefficient of the microstrip feed is too high at resonance, this is due to the distance from the microstrip to the bottom of the upper cylinder, since the microstrip is not directly under the lower cylinder. This leads to the challenge of improved matching in order to tune the frequencies and precisely determine the geometrical parameters. An example of this is shown in Figures 58 and 59. For convenience, the microstrip feedline is matched in Figures 58 and 59, so that the scale in Figure 59 is informative. The matching is described in the next section. The TM_{01} mode is ill-matched but is more wideband than the TE_{01} mode so that with improved matching, the TE_{01} mode will be within the TM_{01} resonance. In this modification, the TE_{01} mode has moved down in frequency to *2.47GHz* and the TM_{01} is now centered around *2.6GHz* but the bad matching and wideband behavior are hiding that it is covering the TE_{01} mode at *-10dB* reflection coefficient.

3.2.3 Matching

As can be seen in Figure 59, the coupling to the TM_{01} mode using only a circular disc at the bottom of the resonator is weak. A glance at the Smith chart for the structure corresponding to Figure 58 with a microstrip and coaxial cable of *50Ω* characteristic impedance shows that the TM_{01} mode is ill-matched, see Figure 60. Since the load (dielectric resonator) impedance is not known the matching of this load requires some attention. For the microstrip excitation, matching

can be done by a quarter-wave transformer or a stub. For the coaxial feedline, a matching network is more difficult to realize, especially since the deembedded input impedance at the bottom of the resonator is below 5Ω. In the microstrip case, there is also the complication of a large input impedance variation over the frequency range.

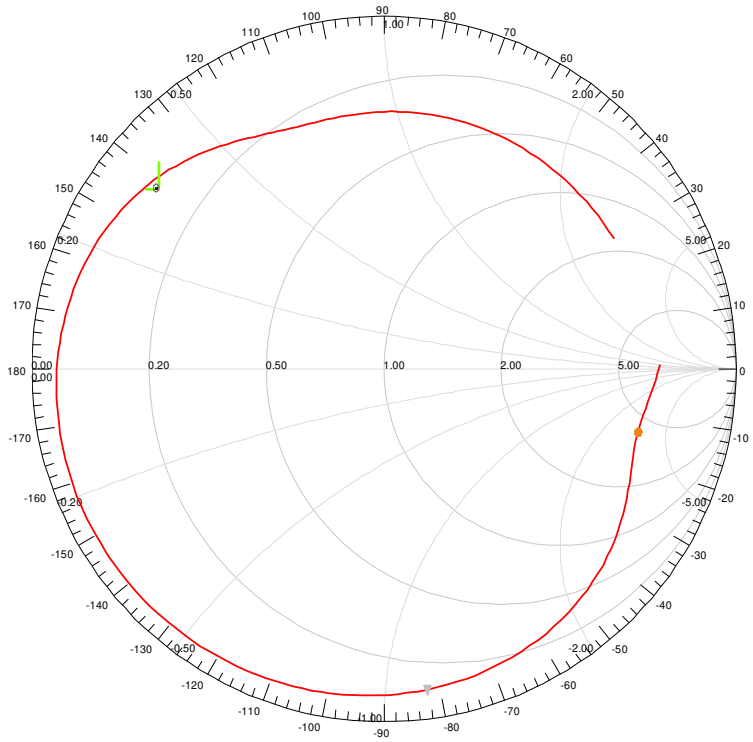

Figure 60: Smith chart of the reflection coefficients for the structure from Figure 58. The microstrip feeding (red curve) has a high impedance-versus-frequency variation. The coaxial feed (green curve) is inductive and the resistive part is below 5Ω. The solid-dot marker is at frequency $2.47GHz$ (see Figure 59). The triangle and empty dot markers are for the center frequency $2.55GHz$. Both excitations need some kind of matching at this stage.

3.2.3.1 Coaxial Cable Coupling

The effect of the conducting disc is that the TM_{01} mode couples better to the resonator. The larger the disc, the lower is the reflection coefficient. However, a too large disc may have the result of high ohmic losses and more important, a large disc radius would imply closeness to the microstrip and thus higher cross coupling between the two ports. Furthermore, the disc might radiate itself.

The disc size is seen to be best in terms of cross coupling at around $5mm$. The impedance matching is, however, very little affected by this. The thickness considered for the disc is $35\mu m$. A large disc is expected to act like a loaded monopole alone, regardless of the resonator. However, no dramatic change in return loss or in the Smith Chart is noticed.

The fear from section 3.2.1, that a penetration of the dielectric resonator by an inner conductor probe from a coaxial cable would disturb the TE_{01} field distribution and possibly lead to the excitation of other modes, e.g. the HE_{11} mode, is then tried. The reference point in the Smith Chart is a frequency of *2.55GHz*, i.e. in the middle of the frequency interval.

The result from this experiment is positive. The TM_{01} mode is excited with a small frequency shift and the coupling is stronger. The Smith chart of the S11-parameter for this excitation shows that the resistive part of the input impedance is very low and for the reference point, also slightly inductive.

The length of the probe is the main parameter for this coupling. The longer the probe (up to a certain limit), the higher is the return loss for the TM_{01} mode. The aim is to have a probe as short as possible to avoid cross coupling and mechanical fragility of the structure. An ideal length of the penetration into the resonator is then confirmed to be *10mm*. The total length chosen for the probe is thus *11.524mm*. Both shorter and longer probes give a weaker coupling to the TM_{01} mode.

A circular ring is then introduced with intention to surround the probe and thus shield it from the TE_{01} field distribution but also to have a capacitive effect on the probe feeding. A number of simulations are made with varying ring size for inner and outer radius.

3.2.3.2 Microstrip Feeding

For the microstrip feeding, several parameters affect the resonant frequency and coupling. These are the lateral distance on the substrate from the longitudinal axis of the resonator, the degree of curvature for the microstrip and the width of the microstrip.

It is important to underline that the feedlines, having impact on the resonant frequency can be used for fine frequency tuning but the variations are in the range of a couple of hundred megahertz and a structure with fairly close resonances for two modes should be elaborated from the geometrical parameters.

- Lateral Distance

  The parameter that is most influential in the TE_{01} mode matching process is the lateral distance to the resonator on the substrate. It cannot be too close to the probe but generally a small distance gives significantly better coupling (*+5 to +10dB*) compared to a lateral distance larger than the big resonator radius. This parameter is finally determined to be *10mm* smaller than the big resonator radius so that the distance to the resonator longitudinal axis is *14.6mm*, see section 3.4 below.

- Microstrip Curvature

A straight microstrip passing by the resonator with varying length has not as high return loss as a curved one. The curvature of the microstrip is parametrically optimized and is seen to be best in terms of matching for a degree of *68.4* degrees in the second quadrant, i.e. for *158.4* degrees with respect to the straight microstrip axis in the counter-clockwise direction as shown below in Figure 61. It is investigated whether a symmetric two-sided microstrip feeding has an impact on the return loss but the difference from having only one microstrip is negligible. It is also advised not to use double sided microstrip feed because of the risk of high cross-coupling.

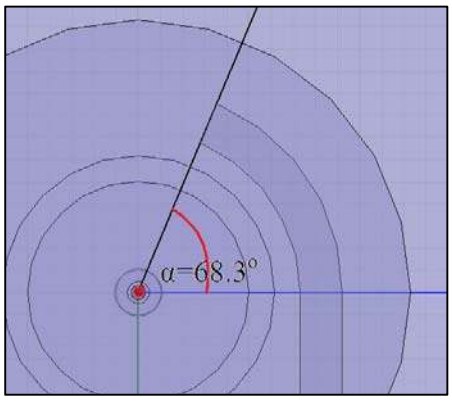

Figure 61: The angle defining the curvature of the microstrip line is optimal around *160 degrees* relative to the microstrip axis.

- Quarter-Wave Transformer

The next thing to be investigated is the influence of a quarter-wave transformer. Since the Smith chart shows impedance with a low resistive part at the port reference plane, the feeding is tried with a microstrip with *20Ω* characteristic impedance. For the substrate in question, the microstrip width is then *13.32mm*. The wider the microstrip (lower characteristic impedance) the better is the matching. This leads to the idea of using a quarter-wave transformer that transforms the impedance down to low resistance and placing it near the load. These experiments show on two things that determine the final design. The first is based on the well known fact that the use of this single-frequency transformer will reduce the bandwidth. A wide transformer (e.g. with width *13.32mm*) gives a very narrow TE_{01} resonance but with a peak return loss of *25dB*. A slimmer transformer gives a more wideband and more shallow reflection diagram. The second thing is that a transformer near the edge of the ground plane, i.e. far from the load, gives better return loss than located closer to the load. A Smith chart is simulated for a transformer placed right on the edge of the ground plane, i.e. at the microstrip connector end. From the Smith chart, the formula

$$\Gamma(z) = \Gamma(0)e^{-2j\beta z} = \Gamma(0)e^{2i\beta z} \tag{3.1}$$

is used. Here, β is the phase coefficient, $\beta = \frac{2\pi}{\lambda}$. As stated above, the reference point in the Smith chart is for the center frequency *2.55GHz*. The transformer is moved a distance z from the connector towards the load so that the (inductive) reference point is moved counter-clockwise to the real axis on the Smith chart. Since the reference point is only slightly inductive this distance is in the millimeter range. For the resonator ultimately designed, this distance is *0.4mm*, see section 3.2.3.3. The most wideband transformer that can be found in this case is a *19.02Ω* transformer (width 14mm). The length is *17.1mm* (one quarter wave in the substrate medium).

- Matching Stub

A stub of *50Ω* characteristic impedance can be used for matching. A parallel open stub is working as capacitor to ground. Its length is varying between *0* and $\frac{\lambda}{4}$ for adjustment of impedance and its position is varied from *0* to $\frac{\lambda}{2}$ for adjustment of phase [29]. A parametric sweep of simulations is made with these variations on a microstrip with the transformer as discussed above and optimal return loss characteristics are found for a length of *8mm* and for a distance from the connector of *28mm*. The wavelength in the Rogers RO3003^{TM} dielectric for frequency *2.55GHz* is *68mm*.

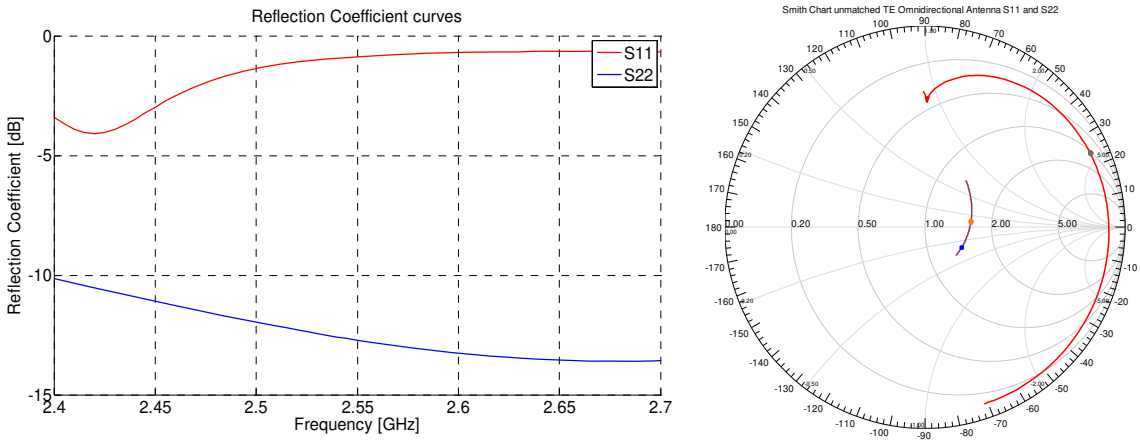

Figure 62: Reflection coefficient diagram (left) and Smith chart (right) in the range *2.4GHz-2.7GHz* of *S11* (microstrip line reflection coefficient, red curve) and *S22* (coaxial cable reflection coefficient, dark curve) for a resonator of permittivity *10.2* without matching stub and quarter wave transformer.

Figure 62 shows the reflection coefficient and Smith chart for the ultimately designed dielectric resonator with a probe of optimal length penetrating into the center surrounded by a shielding ring and a *50Ω* microstrip feedline with the right lateral distance and curvature but without transformer and stub. The coaxial feeding has low reflection coefficient (S22) because of a probe inside the resonator. The red curve in the Smith chart is S11 (microstrip feeding). The dip marked with a triangle is at *2.44GHz* and represents a resonance. The matching is not as satisfactory as for the coaxial feeding. On the S22 curve the triangle marks the center frequency *2.55GHz*.

In Figure 63, the reflection coefficient and Smith chart for the same structure including a transformer and stub is shown and a clear improvement in return loss is visible.

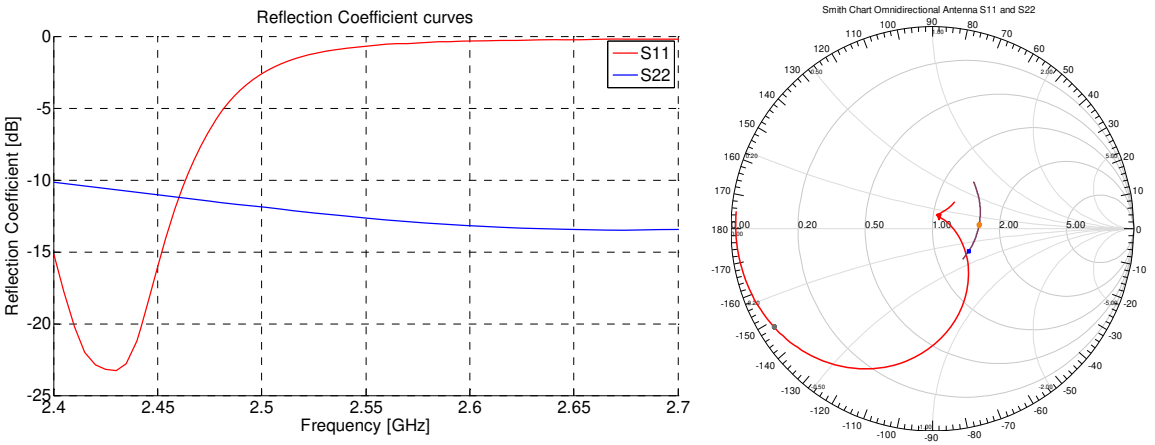

Figure 63: Reflection diagram (left) and Smith chart (right) in the range *2.4GHz-2.7GHz* of *S11* (microstrip reflection coefficient, red curve) and *S22* (coaxial cable reflection coefficient, dark curve) for a resonator of permittivity *10.2* with matching stub and quarter wave transformer.

3.2.4 Outcome

As will be explained in section 3.4 about fabrication, the final omni-directional design is a double-cylinder dielectric resonator with lower radius *12.3mm* and lower height *1mm* and upper radius and height *24.6mm* and *17.5mm* respectively. The feeding is realized by a coaxial probe of length *11.524mm* and radius *0.64mm* going through the substrate and *10mm* into the resonator along the longitudinal axis. A copper ring of thickness *35µm* and outer and inner radii *10mm* and *1mm* respectively is centered on the substrate around the probe. The microstrip feeding is realized by a curved copper strip of thickness *35µm* defined by an angle of *68.3* degrees according to Figure 61. The *50Ω* microstrip is complemented by a transformer of length *17.1mm* and width *14mm* at a distance of *0.4mm* from the connector. A *50Ω* parallel stub of length *8mm* is located *28mm* from the connector.

The resonator material is Rogers RT/duroid 6010^{TM} and the substrate material is Rogers RO3003^{TM}. The ground plane has the dimensions *250*x*250mm*^{2} and consists of a *35µm* copper layer. The connector for the coaxial feeding is *50Ω* gold plated female SMA. The connector for the microstrip feeding is a *50Ω* gold plated female SMA printed circuit board launcher.

An Ansoft HFSS drawing of the structure is shown in Figure 64. Photographs of the manufactured omni-directional antenna, see section 3.4, is shown in Figure 65. For complete drawings and dimensions, see the Appendix.

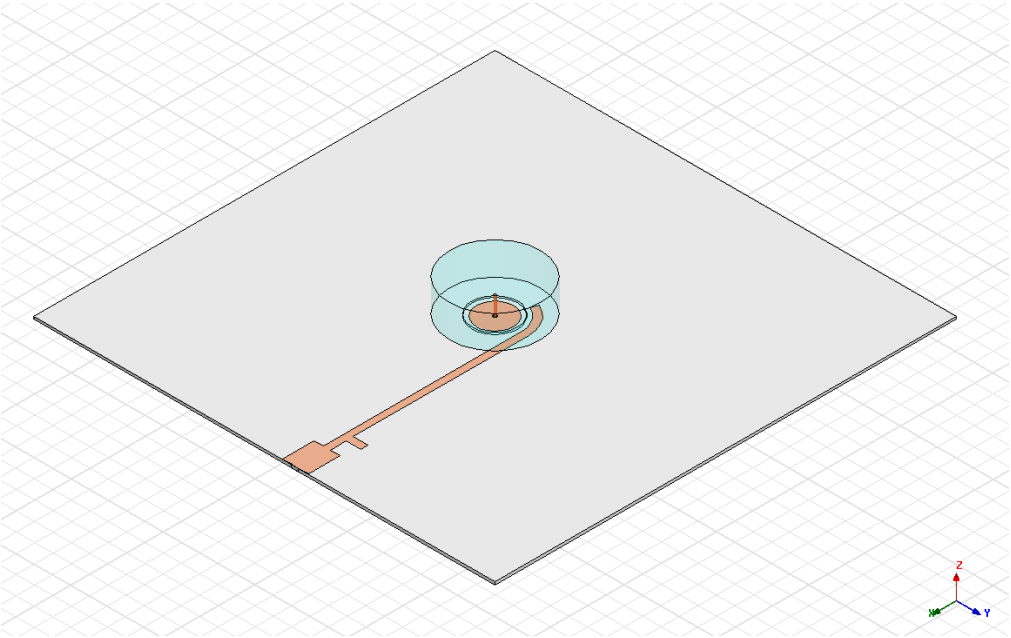

Figure 64: Final design of the omni-directional dielectric resonator antenna. The drawing is made in Ansoft HFSS.

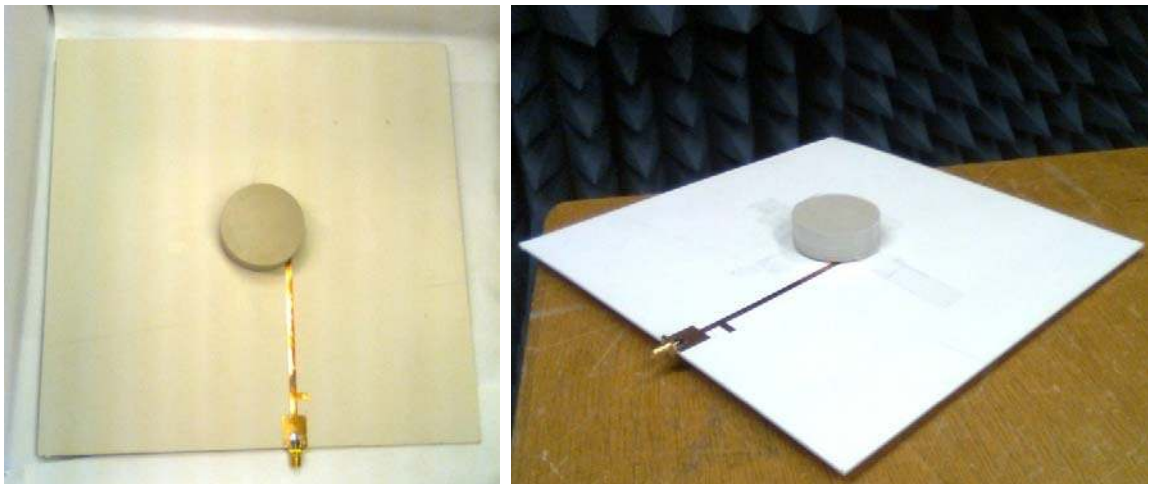

Figure 65: Photographs of the manufactured omni-directional dielectric resonator antenna.

3.3 Broadside Array Antenna Design

The broadside 4x1 array antenna is to be designed for macro base transceiver systems for MIMO applications for mobile communication. The frequency range of operation is between *3.8GHz* and *4.2GHz*. The requirement for the 4x1 array antenna is given below in Table 3.2.

Parameter	Requirement
Frequency	3800 – 4200 MHz
Return loss	> 15 dB
Antenna port isolation	> 15 dB
Efficiency	> 90 % (> -0.45 dB)
Connector	SMA (female)

Table 0.2: Parameters of the performance characteristics for the broadside antenna.

3.3.1 Excitation Technique

Off-center probe excitation is commonly used and the lowest order hybrid HE_{11} mode is achieved by using this method. In order to match the probe with the dielectric resonator antenna a hole is drilled at the edge of the each element of 4x1 array antenna. This insertion of the probe inside the element helps in improving the return loss and thereby also the bandwidth. The height and location of the probe are carefully selected. If the height or the location of the probe is not properly placed then it will affect the matching and resonant frequency respectively. There are two probes used in one element of the 4x1 dielectric resonator antenna which are orthogonal to each other in order to get dual polarization. The length of the probe inserted inside the dielectric resonator antenna is *5mm*. Figure 66 is showing the position of the probe in dielectric resonator antenna.

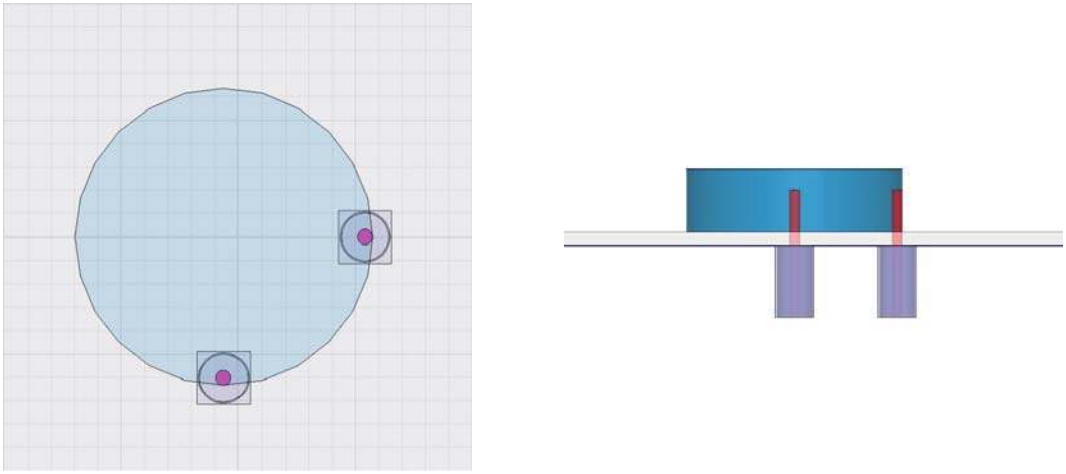

Figure 66: Position of the probes in a cylindrical dielectric resonator. Top view (left) side view (right).

3.3.2 Choosing Parameters

The program FOAM© is used to estimate the size of each element of the 4x1 dielectric resonator antenna at the desired resonant frequency of *4GHz*. The resonant frequency calculated by FOAM© is *4.074GHz* with both radius and height *12.7mm*. This is shown in Figure 67.

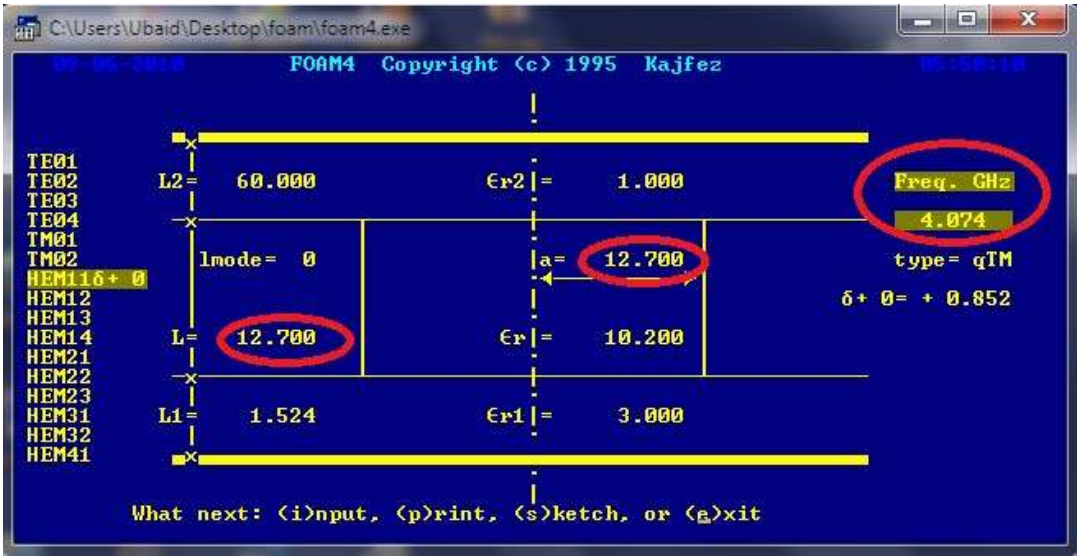

Figure 67: Prediction of resonant frequency of the broadside HE_{11} mode in FOAM© [23].

When these dimensions are simulated in Ansoft HFSS the resonant frequency is above *4GHz*. According to the theory, the height of the elements is reduced from *12.7mm* to *7.5mm* and the simulation results show that the resonating frequency is at *4GHz*. The simulated and measured results are shown and discussed in Chapter 3 below.

The array is arranged in such a way that four resonating broadside elements are placed on equal distances from one another. The spacing between the elements is recommended to be between $0.5\lambda_0$ and $0.67\lambda_0$. The shorter the internal spacing between the elements is, the wider is the main lobe and the angle of the first null in the radiation pattern is larger. This comes from:

$$d \cdot \sin(\alpha) = n \cdot \lambda_0/2 \tag{3.2}$$

Here, d is the center distance between the resonators and α is the 90-degree complement of the elevation angle θ, see Figure 68.

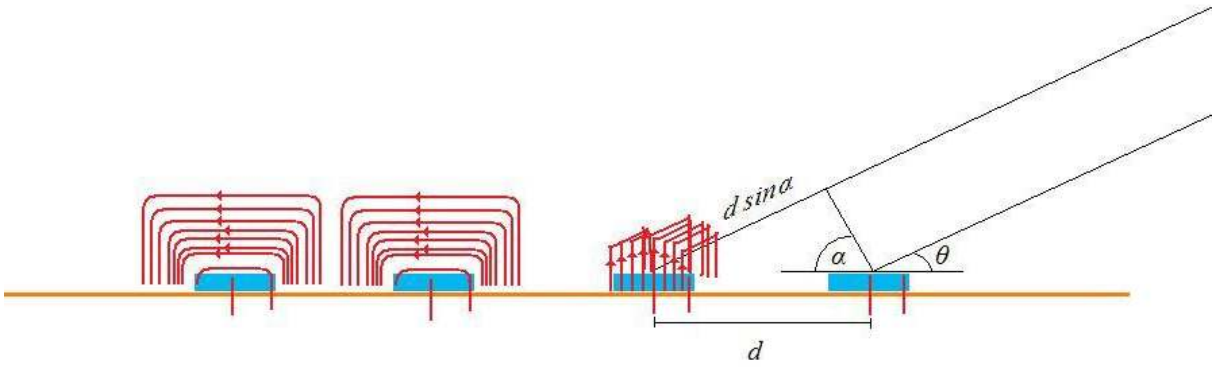

Figure 68: A four-element linear array (side view). The internal distance between two adjacent elements is *d* and the first null comes when *n* in equation 3.2 is equal to *1*.

When is $n=1$ and d is the distance between two adjacent elements, the first null in the radiation pattern appears and this decides the beam-width of the main lobe. The free space wavelength is fixed, so the higher-order nulls come from $n>1$ and when d represents the spacing between elements that are not adjacent. In this context, a wide beam comes from maintaining a low d and compensating by a high $sin(\alpha)$, i.e. when α is close to 90 degrees. However, what Figure 68 also illustrates, the closeness of the resonators affects the cross coupling. The two left elements have field lines for the polarization of the probes located on the edge of the resonator along the horizontal axis. The field lines go along the array axis and the coupling is stronger than the one belonging to the orthogonal polarization, whose field lines are shown on the third resonator from the left. These field lines are parallel for two adjacent resonators and are orthogonal to the array axis.

The distance between the resonators is thus decided by a parametric investigation from $0.5\lambda_0$. It turns out that the transmission parameters for the odd excitations (on the axis), e.g. S13 and S31 (see the Results for the numbering of ports) are below -15*dB* in the frequency range for a distance d which is *52.5mm*. This center-to-center distance is in terms of wavelength $0.7\lambda_0$, fairly close to the recommended upper limit.

3.3.3 Matching

The matching is done by choosing a 6.524*mm* length of the probe which is inserted in the substrate and each element of the 4x1 array antenna. The Smith Chart shown below in Figure 69 shows that the matching of the probe and dielectric resonator antenna is well tuned to 50Ω.

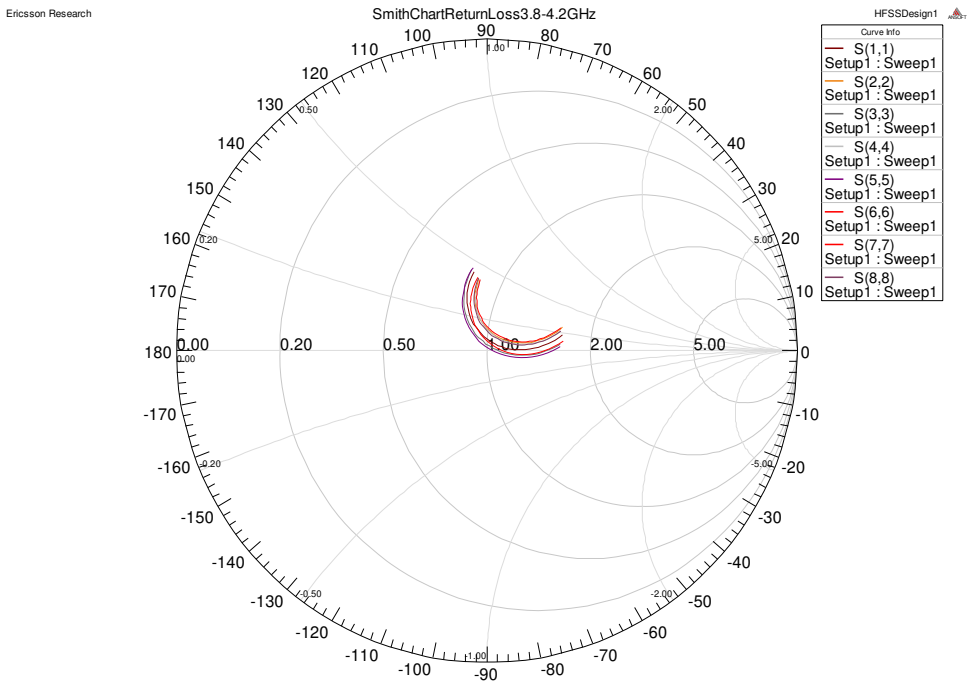

Figure 69: Smith Chart showing the matching of *S11, S22, S33, S44, S55, S66, S77* and *S88* (two ports on each element).

3.3.4 Outcome

The simple cylindrical shape makes the broadside antenna easier to manufacture than the omni-directional antenna. The simple structure is important for the dielectric material used since this material is a flexible and soft plastic.

The broadside-radiating element is a cylindrical dielectric resonator of radius *12.7mm* and height *7.5mm*. The resonator material is Rogers RT/duroid 6010™. The resonator is placed on a Rogers RO3003™ dielectric substrate of dimensions *210* x *210mm*^{2} below which is a *35μm* copper layer. The resonator is fed by two coaxial probes penetrating 6.*524mm* into the resonator from the substrate and the probe radius is *0.64mm*. The probes are to be connected to *50Ω* gold plated female SMA connectors. The outer radius of the connectors is *2.03mm*, which is the radius of the hole in the copper ground, to which the dielectric cladding from the connectors is attached. The location of the probes is on the outermost quadrant of the cross section of each resonator element and they are located at an angle of 90 degrees with respect to each other.

The linear 4x1 array consists of four resonators of the same properties, placed on a substrate and ground plane of dimensions *332.9x175.4mm*^{2}. The center-to-center distance between the resonating elements is *52.5mm*, corresponding to 70% of the free space wavelength. The distance from one edge resonator to the edges of the ground plane is one free space wavelength at the center frequency, i.e. *75mm*.

Drawings of the single element dielectric resonator antenna and the 4x1 array antenna are shown in Figures 70. Photographs of the same are found in Figure 71.

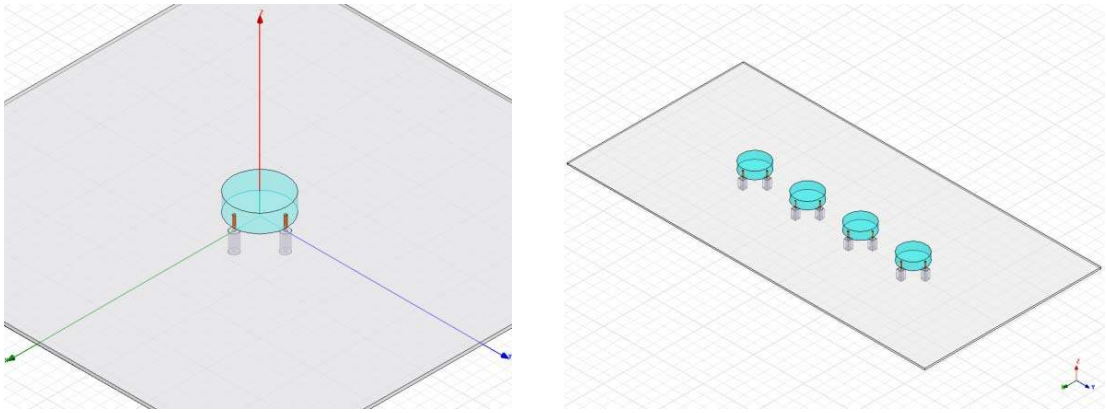

Figure 70: Single element of a broadside DRA (left) and 4x1 DRA array (right). The drawings are from Ansoft HFSS.

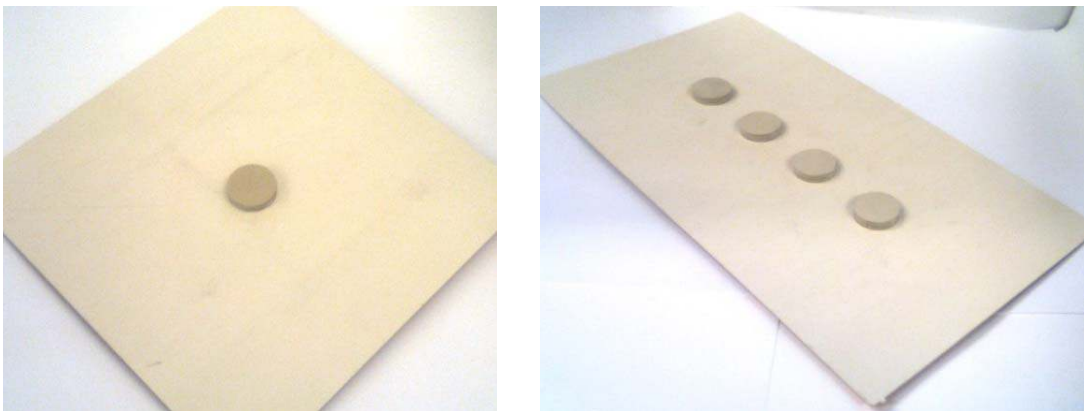

Figure 71: Photograph of the manufactured broadside DRA (left) and the manufactured broadside 4x1 DRA array (right).

3.4 Fabrication

After the adjustments of the dimensions, the available material sizes are investigated. There are two Rogers layers of permittivity *10.2*. Modeling is made with Rogers RO3010^{TM} laminate from the RO3000^{TM} series and availability conditions imply the use of Rogers RT/duroid 6010^{TM}. This material is a combination of PTFE and ceramic and gives an impression of softness compared to the plastic impression which is given by the RO3000^{TM} series. The standard sheet sizes available are from *1.27mm* up to *2.5mm* thickness with a panel size of *10*x*10* inch (*254*x*254mm*^{2}). The upper cylinder of height *18mm* is thus simulated with height *17.5mm* (i.e. seven sheets exactly). The simulation results are affected in the sense that the TE_{01} mode shifts to lower frequencies. This is compensated by a stepwise decrease of the radius from one inch to *24.6mm*. With this configuration the return loss of the microstrip feed is precisely within the range *2.4GHz-2.46GHz* at *-10dB* reflection coefficient. For the lower cylinder the ideal height would thus be *1.27mm* (one layer thickness), but simulations show that the microstrip reflection coefficient would be too high and this height is thus kept as *1mm*. The challenge is then to grind one sheet to the desired

thickness. For the coaxial probe length, a length of *8.5mm* or *11mm* would be suitable for the penetration into the dielectric resonator. This would require an even number of sheets and no partly drilled sheet in the resonator. To this length should be added the thickness of the Rogers RO3003^{TM} substrate which is *1.524mm*. A minimum length for the probe was stated as *11.524mm*, see section 3.2.4 about matching, so one sheet needs to be partly drilled. Simulations with *8.5mm* probe penetration length showed on a coupling not completely in the frequency range for *-10dB* and the same for probes longer than *11.524mm*. This was resolved by the ordering of Rosenberger 32K722-500E3 gold plated female SMA connectors (for a specification, please see the Appendix), from which the dielectric coating is removed and the original length of *17.9mm* is cut and polished to the desired length of *11.524mm*.

For the broadside *3.8GHz-4.2GHz* elements, the height of *7.5mm* is suitable since it requires exactly three sheets of thickness *2.5mm*. The probe length of *5mm* penetrating into the resonator is also suitable from this point of view. The connectors used in this case are Rosenberger 32K764-500N5 silver plated female SMA connectors (see the Appendix for a specification). The length of these probes is *7mm* which is close to the designated *6.524mm* simulated for the broadside antenna elements. The difficulties in the fabrication of these antennas are the holes to be drilled for the probes. These should go through two layers of the RT/duroid 6010^{TM} but be placed on the outermost edge on the quadrant of the circles that are base areas of the cylindrical layers. Drawings of the cylindrical layer elements are attached in the Appendix.

The RT/duroid 6010^{TM} sheets provided by the Rogers Corporation are shaped and drilled by the workshop unit of MAX-lab at their facilities in Lund, Sweden. This is also where the grinding for reduction of thickness of the omni-directional base cylinders is successfully performed. The cylinder layers of the Rogers RT/duroid 6010^{TM} are shown in Figure 72.

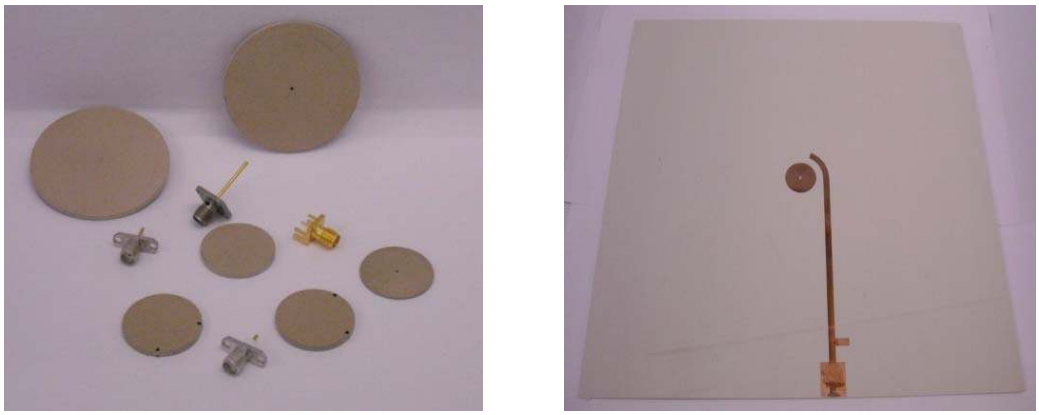

Figure 72: Sample layers for the omni-directional and the broadside array antenna with connectors (left) and omni-directional antenna substrate sheet with feeding network (right).

The substrates are based on Rogers RO3003^{TM} sheets with 35µm electrodeposited copper-foil on both surfaces. The sheet size is a standard 18x24 inches (*457*x*610mm*^{2}) panel which is processed and supplied by Cogra AB, Älvängen, Sweden. The processing includes etching of the upper copper surface into the desired microstrip feedline including transformer and matching stub

(omni-directional elements), the creation of a copper ring and the drilling of holes of radius *0.65mm* through the substrate as well as etching of holes of radius *2.03mm* on the bottom side for the coaxial Teflon-to-substrate transition. For the broadside array and single elements, one side is completely cleaned from copper cladding and the two types of holes are drilled and etched respectively. Two sheets are ordered, one containing two identical substrates for the omni-directional antenna (see Figure 72) and one containing three broadside antenna bases, one 4x1 array, one 8x1 array and one for a single broadside element. The drawings of the arrays placed on the sheets with dimensions are shown in the Appendix, where three-dimensional HFSS models of the two sheets also can be found.

3.5 Measurement Methodology

The manufactured dielectric resonator antennas are evaluated in terms of scattering parameter- and radiation pattern measurements.

3.5.1 Measurements of Scattering Parameters

Measurements of scattering parameters are performed on one omni-directional antenna, the single broadside element and the 4x1 broadside array antenna between September 14th and September 17th 2010 in the facilities of Ericsson AB, Lindholmen Gothenburg, Sweden. These measurements are performed on a HP85107A Vector Network Analyzer. The setup can be seen in Figure 73.

Figure 73: Two-port measurement of the 4x1 array antenna. The resonators are directed to an absorbing wall to avoid radiation scattering effects. The antenna is seen on face of the ground plane and the coaxial connectors (left); view of the resonator face with the network analyzer in the background (right).

The omni-directional antenna and the single broadside antenna element are measured by a two port measurement of the *S*-parameters. All four scattering parameters according to matrix 3.3 are measured in the two-port measurements and are presented in the Results.

$$\begin{pmatrix} \boldsymbol{S11} & \boldsymbol{S12} \\ \boldsymbol{S21} & \boldsymbol{S22} \end{pmatrix} \tag{3.3}$$

The 4x1 array antenna has eight ports, and the isolation between all these ports is measured in a series of two-port measurements (all other ports terminated with 50Ω loads) according to the sketch in Figure 74. The isolation between two ports needs to be measured internally for one element, between two adjacent elements and between ports of the same polarization. The elements that are obtained from these measurements are marked in the 8x8 *S*-matrix below.

$$\begin{pmatrix} \boldsymbol{S11} & \boldsymbol{S12} & \boldsymbol{S13} & \boldsymbol{S14} & \boldsymbol{S15} & S16 & \boldsymbol{S17} & S18 \\ \boldsymbol{S21} & \boldsymbol{S22} & \boldsymbol{S23} & \boldsymbol{S24} & S25 & \boldsymbol{S26} & S27 & \boldsymbol{S28} \\ \boldsymbol{S31} & \boldsymbol{S32} & \boldsymbol{S33} & \boldsymbol{S34} & \boldsymbol{S35} & \boldsymbol{S36} & \boldsymbol{S37} & S38 \\ \boldsymbol{S41} & \boldsymbol{S42} & \boldsymbol{S43} & \boldsymbol{S44} & \boldsymbol{S45} & \boldsymbol{S46} & S47 & \boldsymbol{S48} \\ \boldsymbol{S51} & S52 & \boldsymbol{S53} & \boldsymbol{S54} & \boldsymbol{S55} & \boldsymbol{S56} & \boldsymbol{S57} & S58 \\ S61 & \boldsymbol{S62} & \boldsymbol{S63} & \boldsymbol{S64} & \boldsymbol{S65} & \boldsymbol{S66} & S67 & \boldsymbol{S68} \\ \boldsymbol{S71} & S72 & \boldsymbol{S73} & S74 & \boldsymbol{S75} & S76 & \boldsymbol{S77} & \boldsymbol{S78} \\ S81 & \boldsymbol{S82} & S83 & \boldsymbol{S84} & S85 & \boldsymbol{S86} & \boldsymbol{S87} & \boldsymbol{S88} \end{pmatrix} \tag{3.3}$$

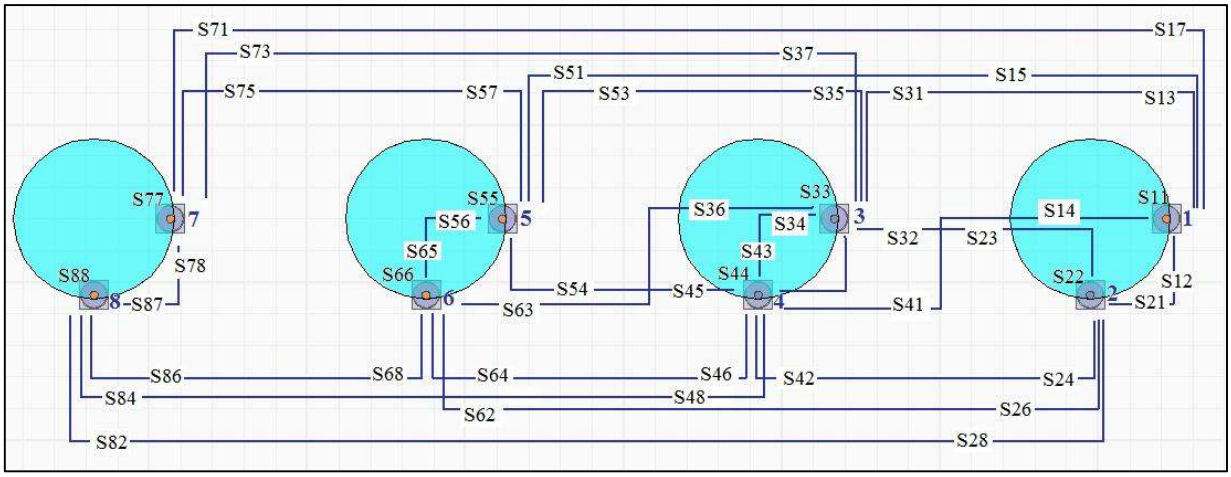

Figure 74: Measurements of reflection and isolation of the broadside *4x1* array antenna. The cross coupling between two adjacent edge elements and the two center elements as well as between ports of the same polarization is measured. This requires 20 two-port measurements in total.

As will be seen in the Results, the measured results of the broadside antennas do deviate from the simulated results in terms of resonant frequency (the center frequencies in the reflection coefficient curves are lower than the simulated center frequency). However, by a small revision of the dimensions, where the total height of the cylinders is decreased from *7.5mm* to *6mm* by grinding of the uppermost sheet of each resonator, the measured center frequency is shifted closer to *4GHz*.

3.5.2 Measurements of Radiation Pattern

Measurements of radiation patterns for the single element broadside antenna, the 4x1 broadside array antenna and the omni-directional antenna are performed on September 23rd at the antenna

measurement range of the department of Signals and Systems at Chalmers University. The antenna is mounted on a receiving pole in the test range. One of the ports is connected to port 1 of a network analyzer. A transmitting pole is connected to port 2 of this network analyzer. The *S12* scattering parameter is then obtained in the network analyzer and displayed in computer software. The software is also controlling the network analyzer and the electric motors of the mounting board and transmitter in the test range.

The pole with the mounting board is the rotated from -180 degrees to +180 degrees with respect to the line of sight to the transmitter. The antennas are mounted in such a way that the angular sweep is with respect to the elevation angle θ. This procedure is repeated for a different cut of the azimuth angle φ by a 90-degree rotation of the antenna including substrate and ground plane. For the omni-directional antenna, a mounting enabling a sweep over the azimuth angle φ is also necessary. The cuts that are measured are the *E*-plane and *H*-plane for each polarization. For every cut and polarization (excitation), the co-polar and cross-polar radiation pattern is measured. For the single broadside antenna and the omni-directional antenna this implies four scans of the elevation angle θ. For the broadside array antenna, the first four ports (see Figure 74 for port numbering) are measured individually. The remaining ports in the two other resonators are assumed to be similar due to symmetry. The two different polarizations are then measured with excitations on all ports of the same polarization. This means that 24 elevation angle sweeps are performed for the array in total.

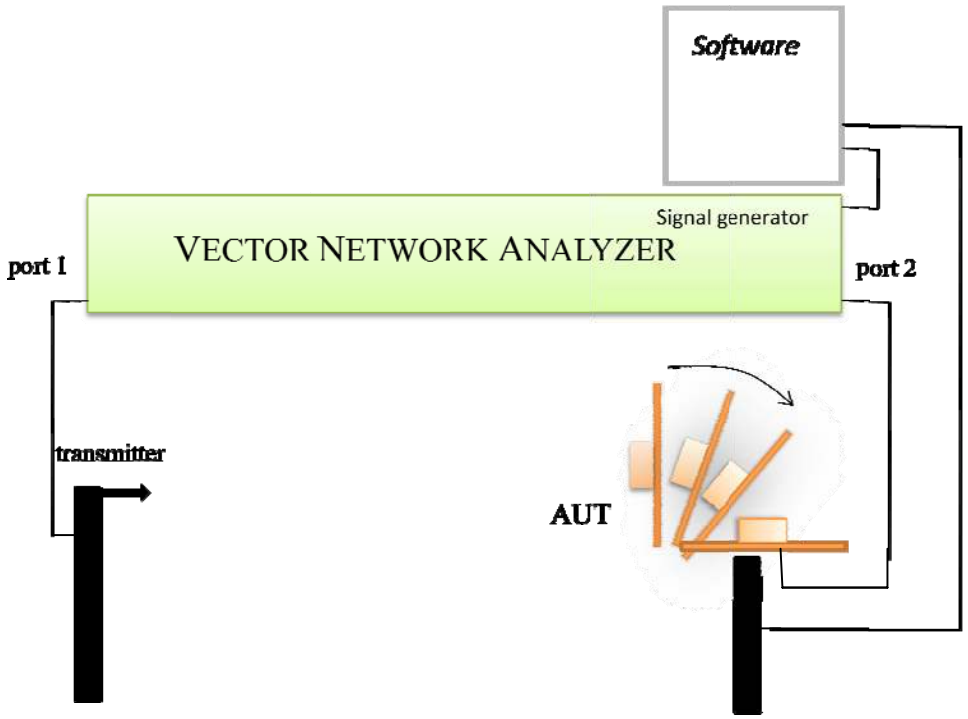

Figure 75: Setup of radiation pattern measurements. The Antenna Under Test (AUT) is placed on a rotating pole. Depending on what plane needs to be scanned the antenna can be mounted vertically or horizontally. A network analyzer processes the input and received signals. The rotational engines of the chamber and the network analyzer are controlled by software.

The single broadside element is measured at three frequency points determined from the reflection coefficient measurements. These points are *4GHz*, *4.2GHz* and *4.4GHz*. The array formation of this element, i.e. the 4x1 array antenna is measured at one frequency point only, *4.2GHz*, for verification of its properties. The omni-directional antenna is measured at the TE_{01} reflection coefficient dips at *2.45GHz* with $\pm$ *25MHz* and *2.60GHz* with $\pm$ *25MHz*, i.e. at six frequency points.

The omni-directional antenna is measured with a sweep in an elevation plane (*H*-plane) and in the azimuth plane (the *E* plane for both the TE_{01} and the TM_{01} mode). A sketch of the radiation pattern measurements is shown above in Figure 75.

3.5.3 Measurement of Efficiency

Measurements of efficiency for the single element broadside antenna and the omni-directional antenna are performed in a reverberation chamber at Bluetest AB, Göteborg.

The artificial multipath environment is generated in a reverberation chamber which provides us to measure the efficiency test in a laboratory-produced environment. The procedure for measuring the efficiency of the antenna in a reverberation chamber is described as follows. The omni-directional antenna is placed inside the reverberation chamber in such a way that it is half to one wavelength away form the walls and the mechanical stirrers. For reference level adjustment a single antenna with known radiation efficiency is placed far away from the antenna to avoid direct coupling. Then one port of the omni-directional antenna is connected to a network analyzer where the other port and the reference antenna are terminated with *50*Ω. Now, the S-parameter is calculated between the ports and the three wall mounted antennas which are used for polarization stirring for all frequency points and for all the positions inside the chamber. This procedure is repeated for each port of the omni-directional antenna one by one by having the same settings and position which produces the same environment for the measurement [31].

The reflection coefficients S_{11} of each wall antenna and S_{22} of the omni-directional antenna port, with the transmission coefficients S_{21} between the two connected ports and the three wall mounted antennas values are stored at every stirrer position and frequency point respectively. The reference antenna is now connected to the network analyzer and the measurements are done for omni-directional antenna. It is important to note that while taking the reference measurement both ports of the omni-directional antenna must be terminated by *50*Ω inside the chamber. In this way the transmission coefficient S_{21} samples are corrected with mismatch factor due to S_{11} and S_{22} before the frequency stirrer and are normalized to 100 percent radiation efficiency [31].

The same procedure is repeated for single element broadside antenna to measure the efficiency.

CHAPTER 4

RESULTS

4.1 Scattering Parameters

Below will follow results from the simulations and measurements of the scattering parameters.

4.1.1 Omni-directional Antenna

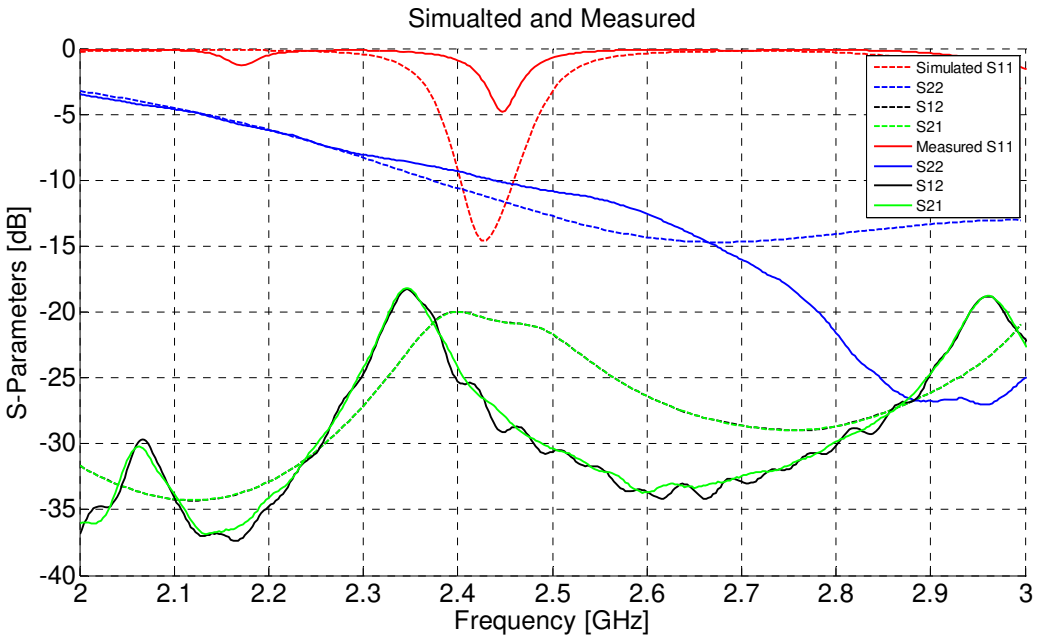

Figure 76: Measured and simulated S-Parameters of the omni-directional antenna.

4.1.2 Broadside Single Element Antenna

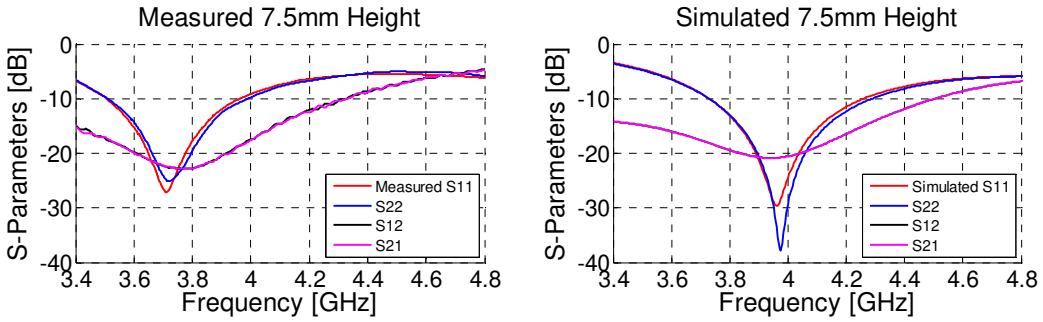

Figure 77: measured and simulated S-parameters of the broadside single element antenna of radius *12.7mm* and height *7.5mm*.

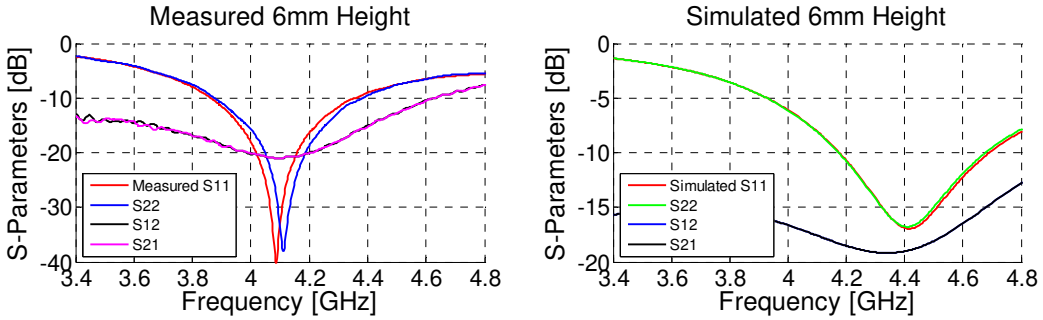

Figure 78: Measured and simulated S-parameters of the broadside single element antenna of radius *12.7mm* and height *6mm*.

4.1.3 Broadside 4x1 Array Antenna

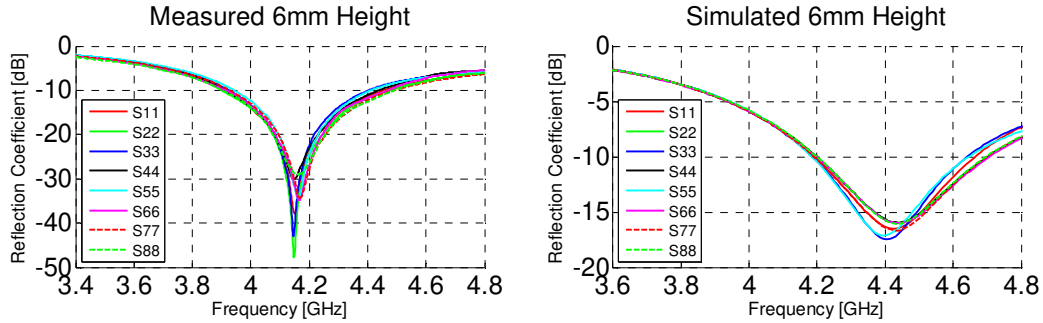

Figure 79: Measured and simulated reflection coefficient of the 4x1 array antenna with radius *12.7mm* and height *6mm*.

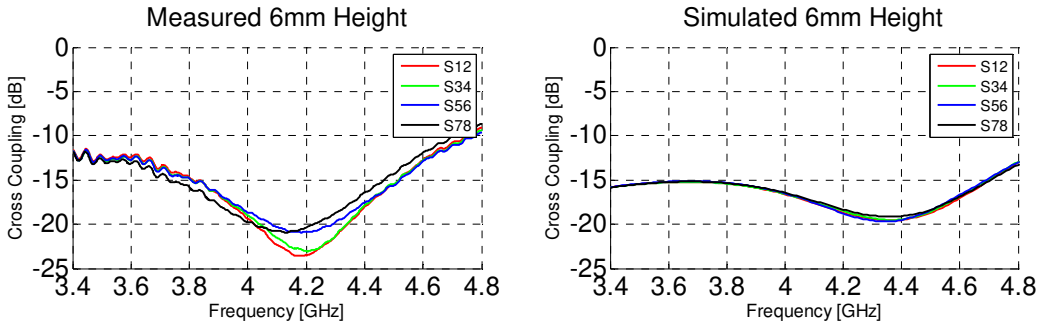

Figure 80: Measured and simulated cross coupling of the 4x1 array antenna with radius *12.7mm* and height *6mm*.

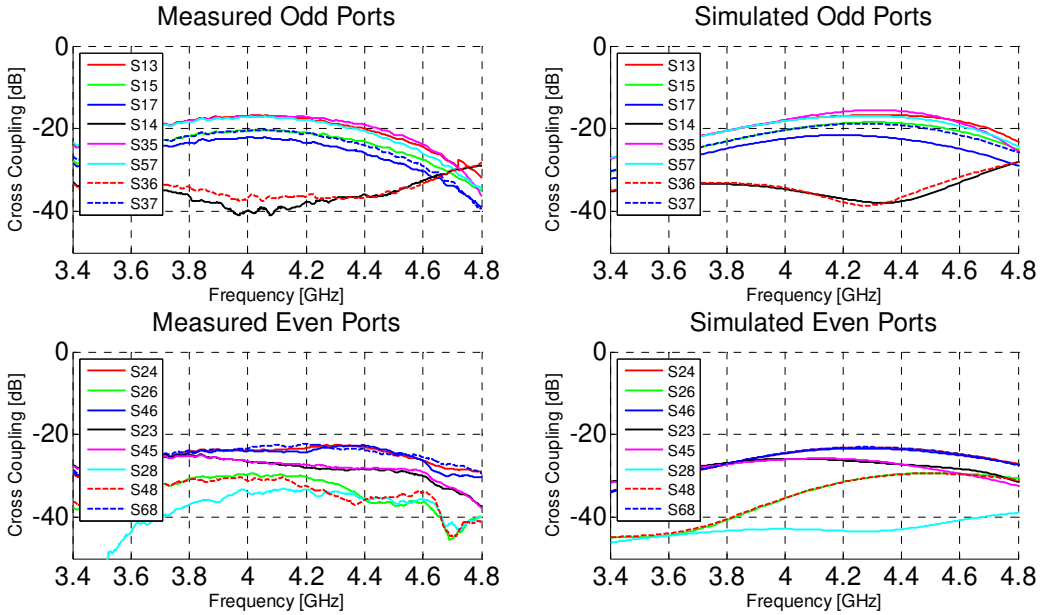

Figure 81: Measured and simulated cross coupling of odd and even ports of the 4x1 array antenna with radius *12.7mm* and height *6mm*.

4.2 Radiation Pattern

Here will be presented the measured radiation patterns of the antennas that were obtained from the antenna test range at Chalmers University. For visualization of the different cuts in the three dimensional radiation pattern, consult Figures 82 and 85 for the omni-directional antenna, Figure 88 for the broadside single element antenna and Figures 93 and 96 for the broadside array antenna.

4.2.1 Omni-directional Antenna

H-plane
(elevation)

E-plane
(azimuth)

Figure 82: Far field radiation pattern of the TE_{01} mode and illustration of *E*- and *H*-planes.

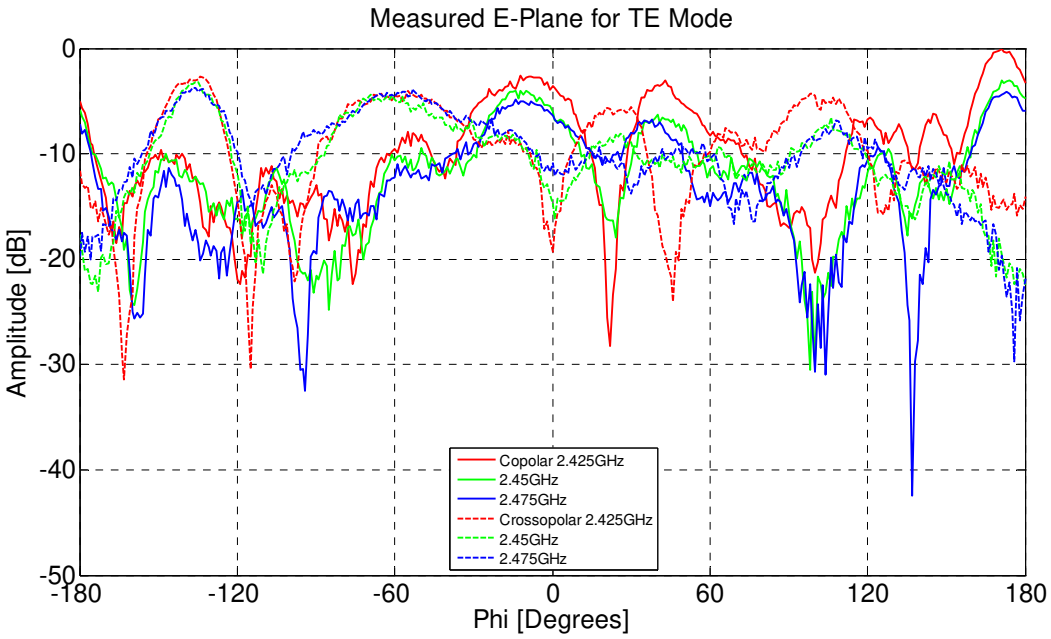

Figure 83: Measured co-polar and cross-polar radiation levels in the *E*-plane for the TE_{01} mode of the Omni-directional antenna.

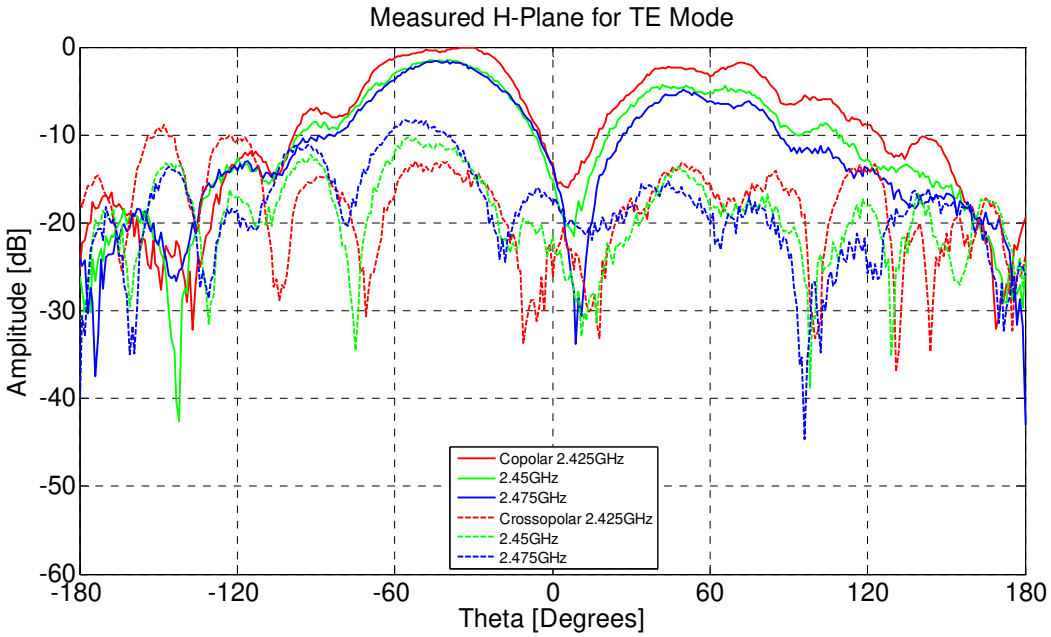

Figure 84: Measured co-polar and cross-polar radiation levels in the *H*-plane for the TE_{01} mode of the Omni-directional antenna.

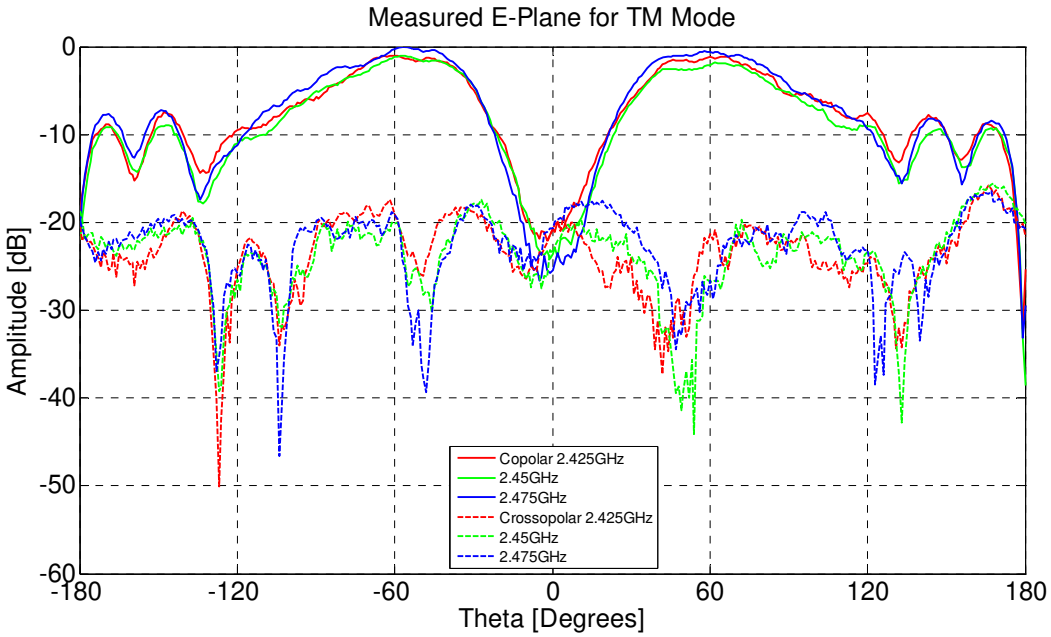

Figure 85: Measured co-polar and cross-polar radiation levels in the *E*-plane for the TM_{01} mode of the Omni-directional antenna.

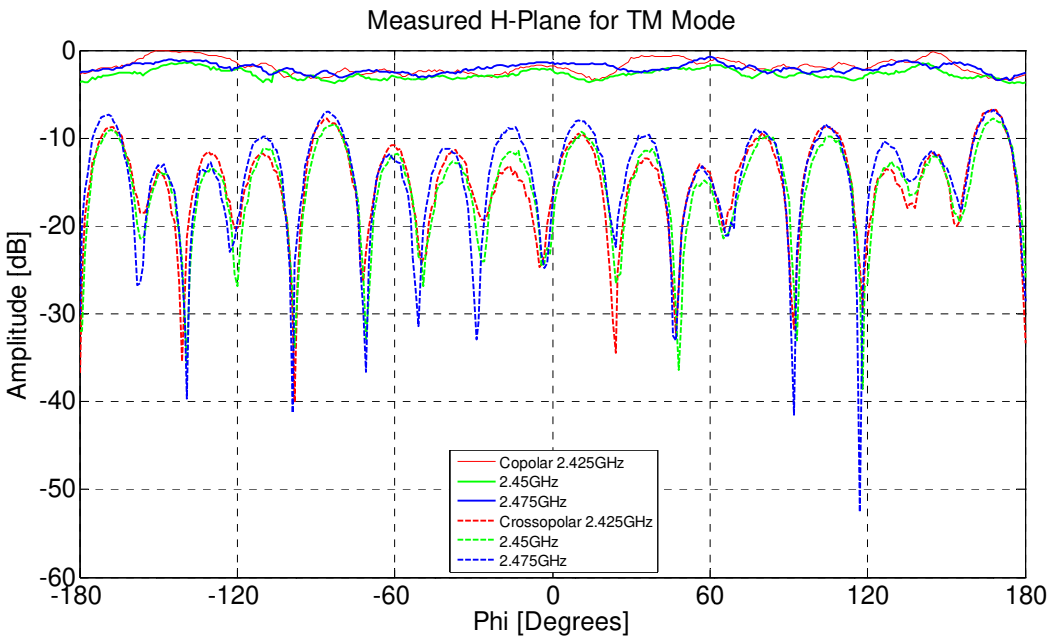

Figure 86: Measured co-polar and cross-polar radiation levels in the *H*-plane for the TM_{01} mode of the Omni-directional antenna.

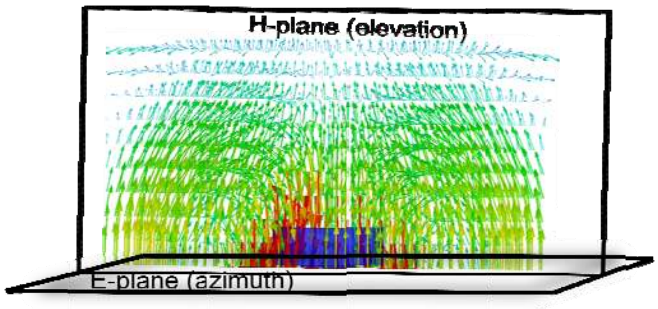

Figure 87: Far field radiation pattern of the TM_{01} mode and illustration of *E*- and *H*-planes.

4.2.2 Broadside Single Element Antenna

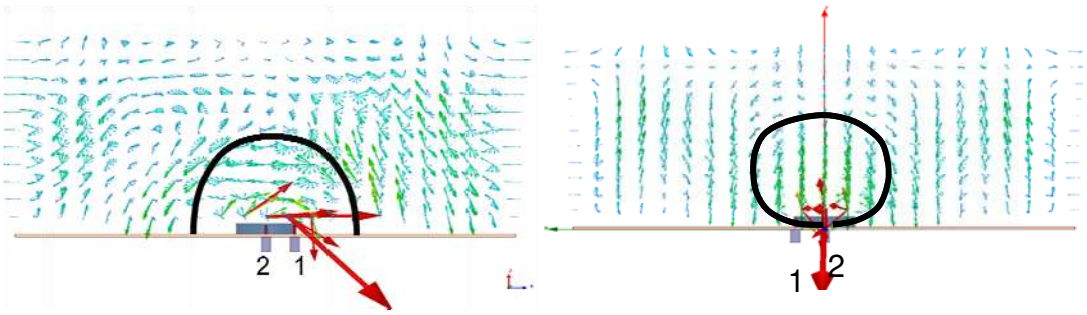

Figure 88: Illustration of the *E*-plane (left) and *H*-plane (right) for port 1 of the broadside single element antenna. The solid balck line marks the beamwidth. The same figure holds for port 2 if the *E* and *H*-plane cuts are interchanged.

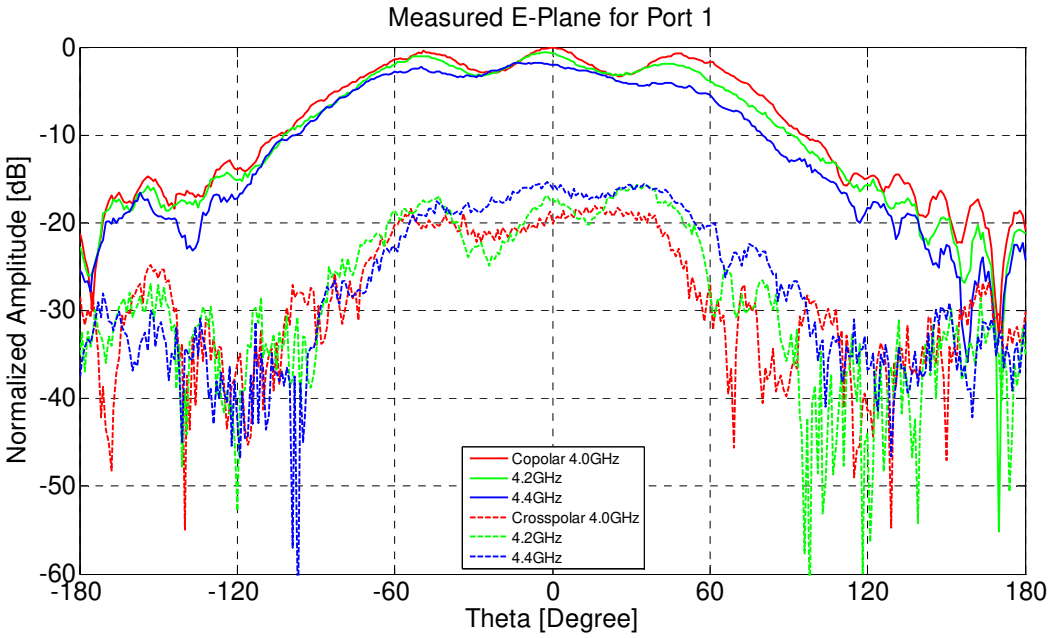

Figure 89: Measured co-polar and cross-polar radiation levels in the *E*-plane for the HE_{11} mode port 1 of the broadside single element antenna.

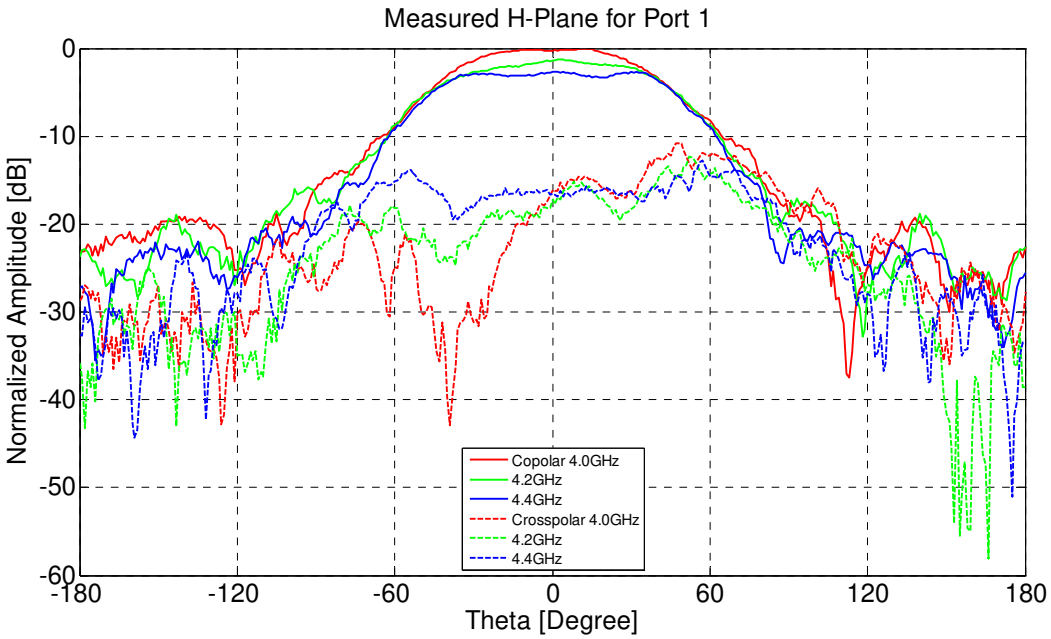

Figure 90: Measured co-polar and cross-polar radiation levels in the *H*-plane for the HE_{11} mode port 1 of the broadside single element antenna.

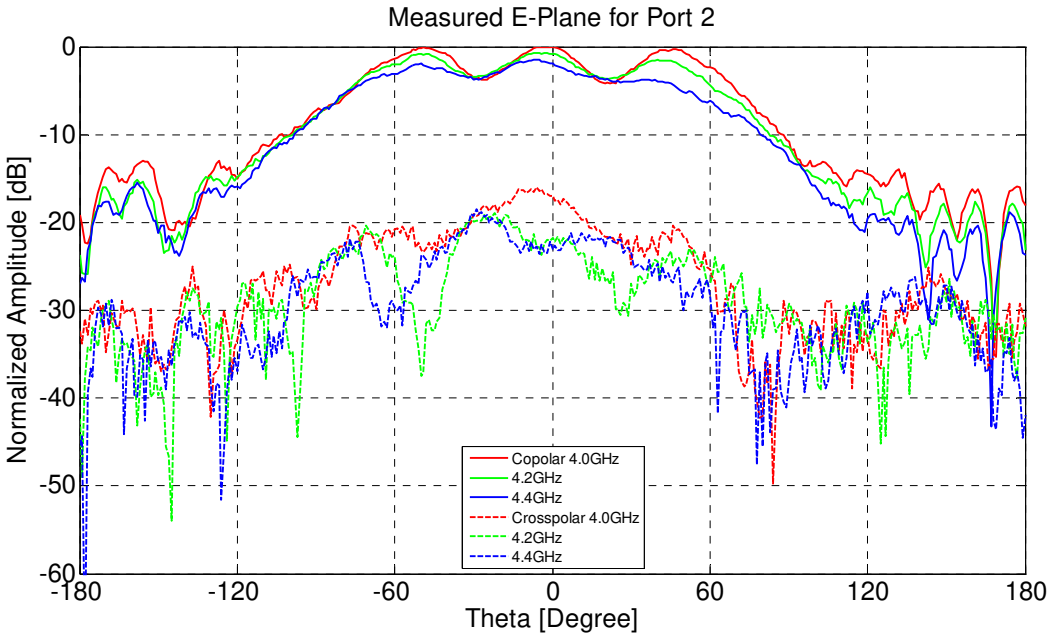

Figure 91: Measured co-polar and cross-polar radiation levels in the *E*-plane for the HE_{11} mode port 2 of the broadside single element antenna.

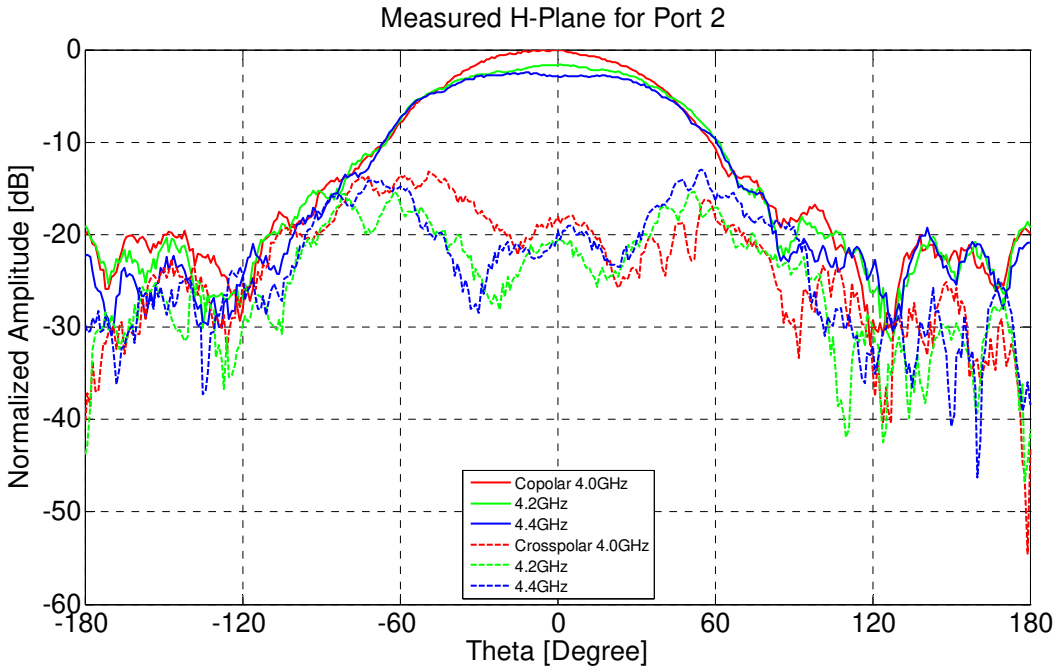

Figure 92: Measured co-polar and cross-polar radiation levels in the *H*-plane for the HE_{11} mode port 2 of the broadside single element antenna.

4.2.3 4x1 Array Antenna

Please refer to the Appendix for the numbering of the array ports.

Figure 93: Illustration of the *E*-plane (left) and the *H*-plane(right) for the array anteena ecited on odd ports. The solid line marks the beamwidth.

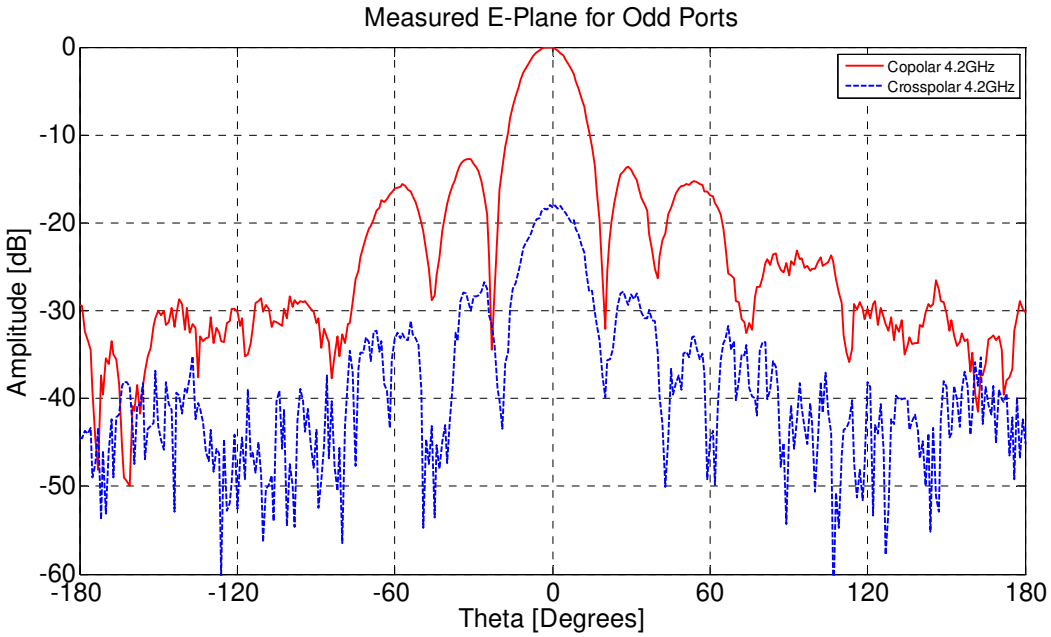

Figure 94: Measured co-polar and cross-polar radiation levels in the *E*-plane for the HE_{11} mode of odd ports of the broadside array antenna at *4.2GHz*.

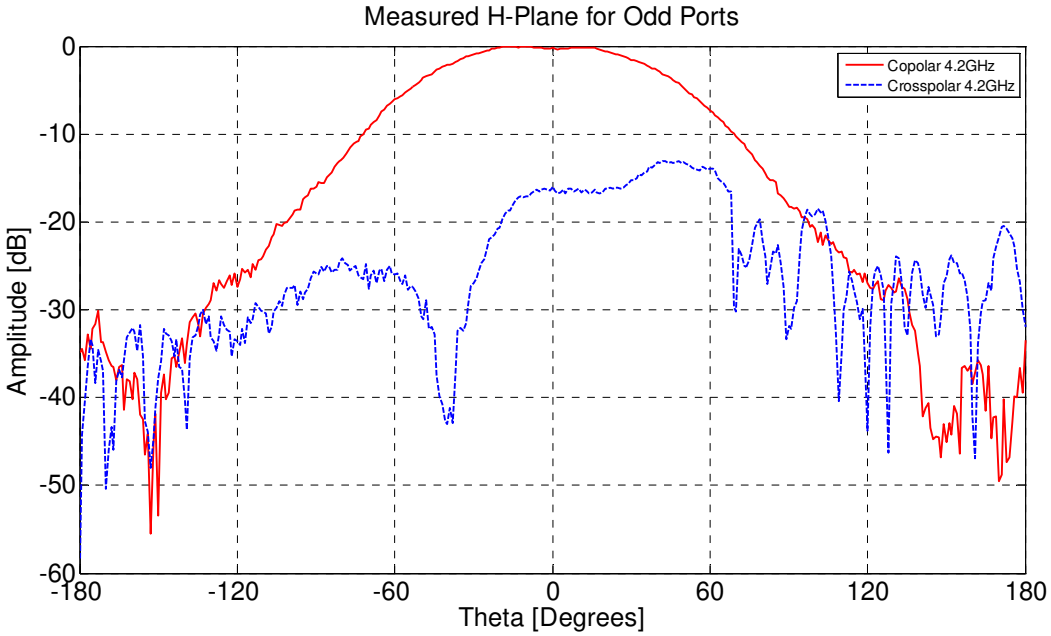

Figure 95: Measured co-polar and cross-polar radiation levels in the *H*-plane for the HE_{11} mode of odd ports of the broadside array antenna at *4.2GHz*.

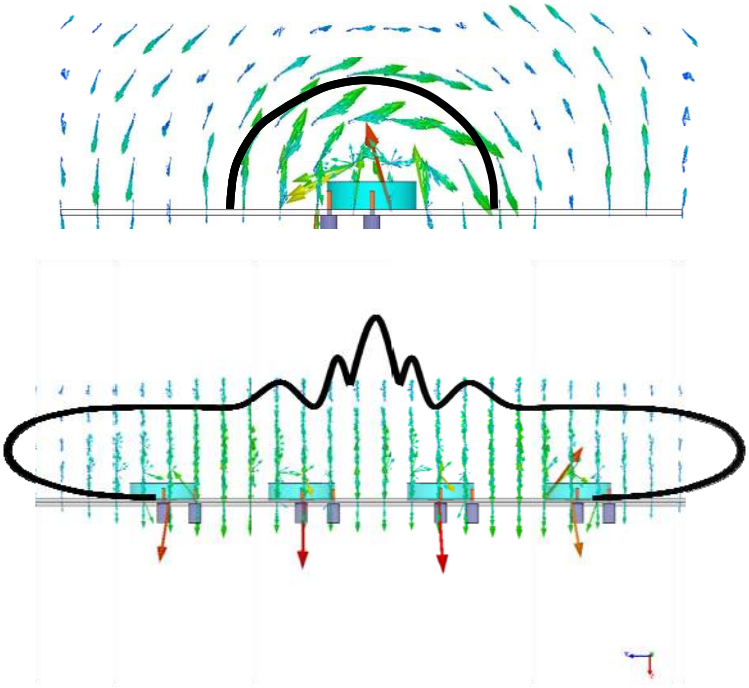

Figure 96: Illustration of the *E*-plane (top) and *H*-plane (bottom) for the array antenna excited on even ports. The solid line marks the beamwidth.

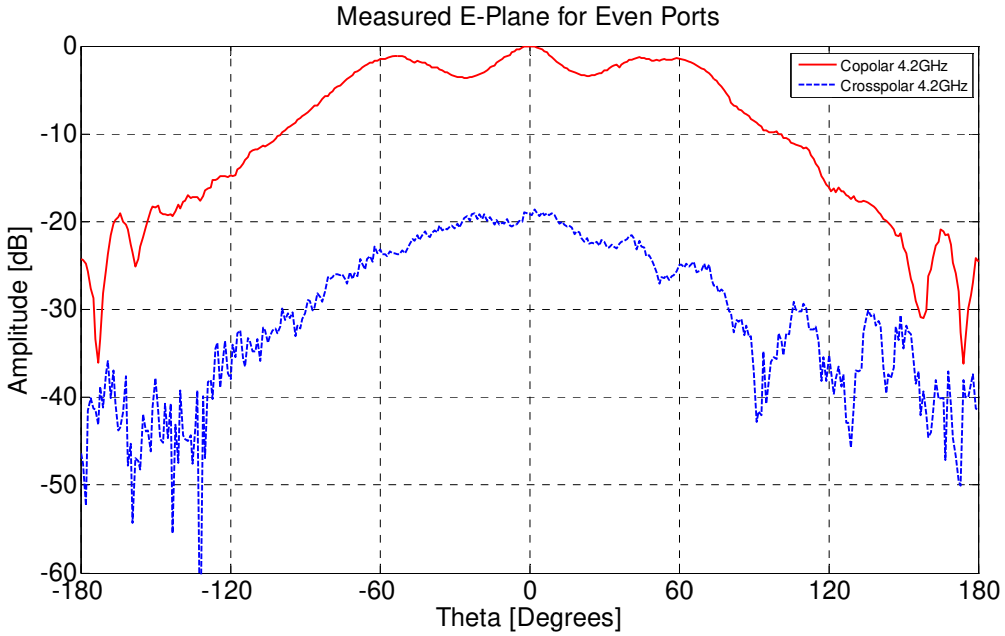

Figure 97: Measured co-polar and cross-polar radiation levels in the *E*-plane for the HE_{11} mode of even ports of the broadside array antenna at *4.2GHz*.

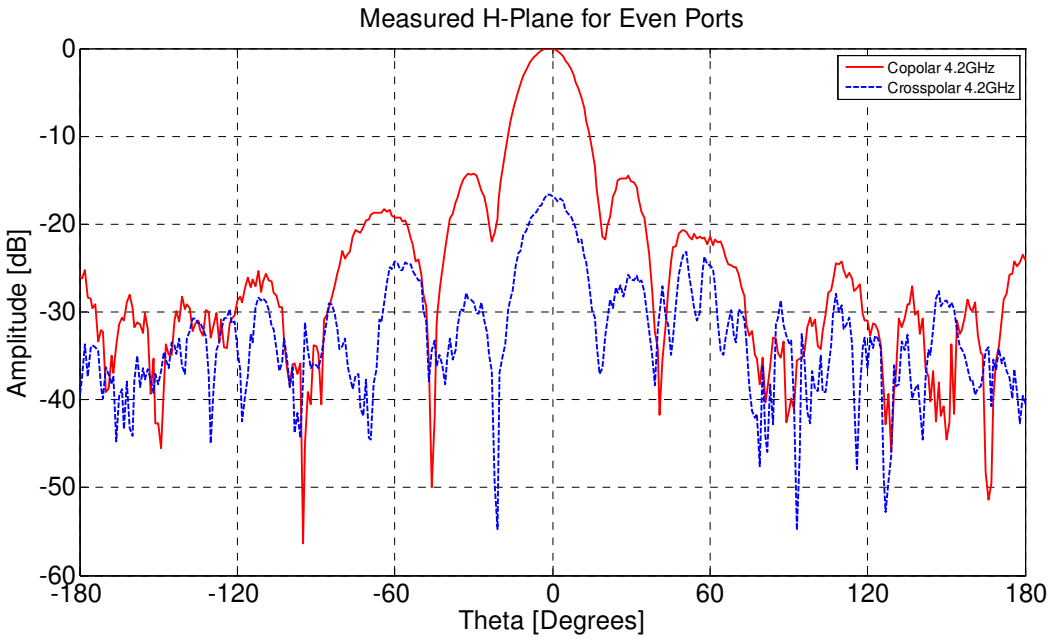

Figure 98: Measured co-polar and cross-polar radiation levels in the *H*-plane for the HE_{11} mode of even ports of the broadside array antenna at *4.2GHz*.

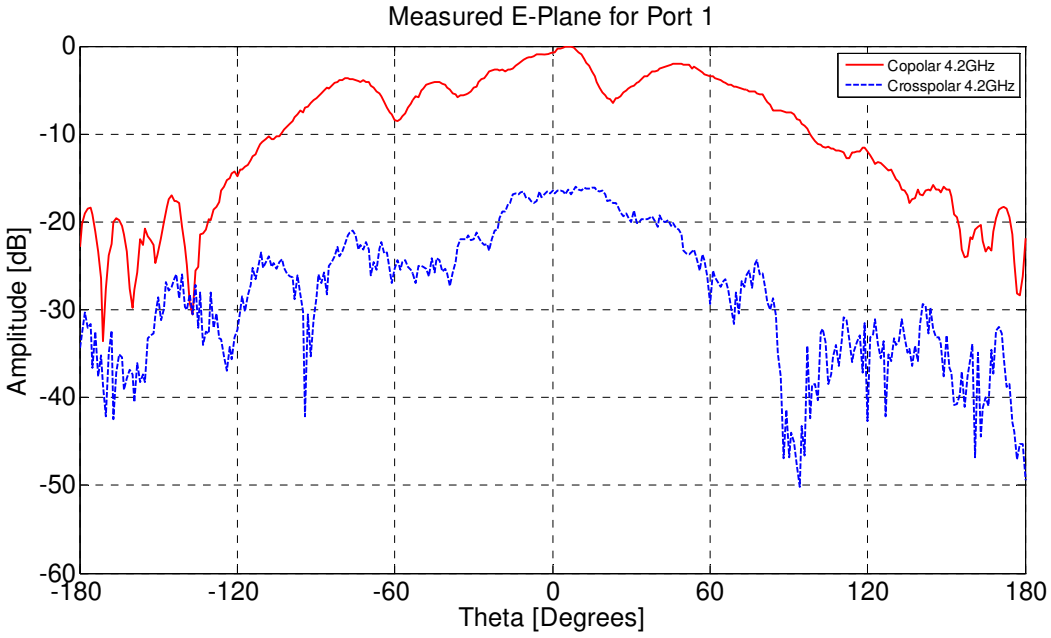

Figure 99: Measured co-polar and cross-polar radiation levels in the *E*-plane for the HE_{11} mode of port 1 of the broadside array antenna at *4.2GHz*.

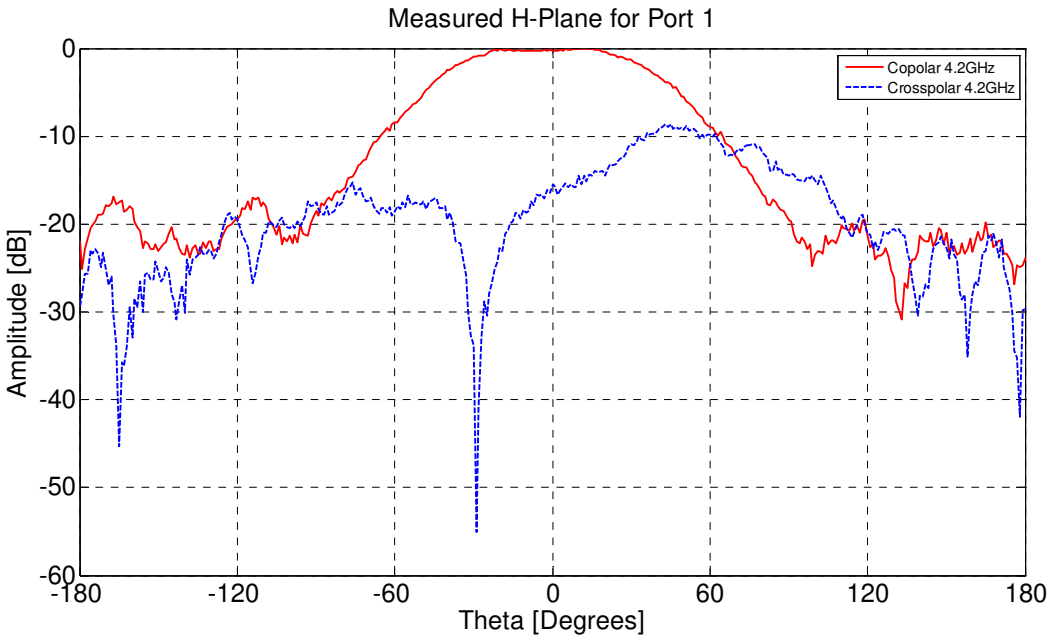

Figure 100: Measured co-polar and cross-polar radiation levels in the *H*-plane for the HE_{11} mode of port 1 of the broadside array antenna at *4.2GHz*.

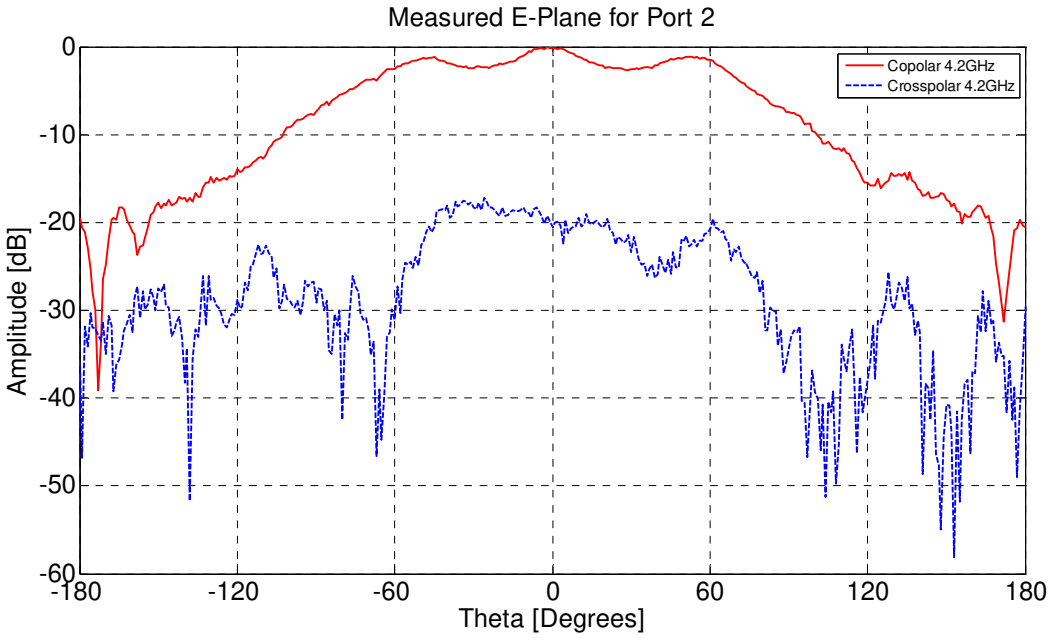

Figure 101: Measured co-polar and cross-polar radiation levels in the *E*-plane for the HE_{11} mode of port 2 of the broadside array antenna at *4.2GHz*.

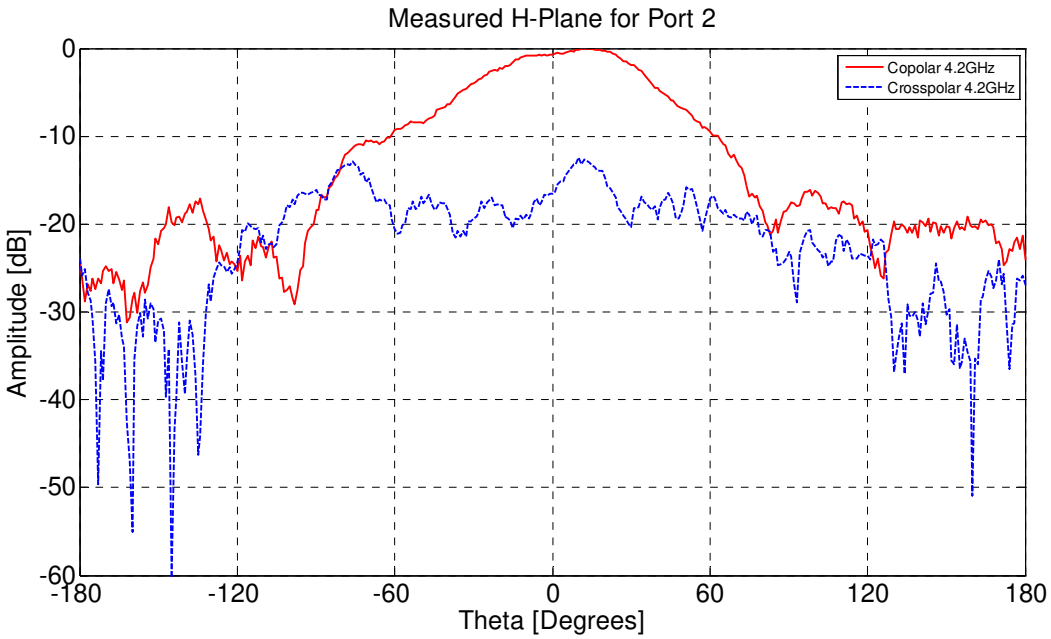

Figure 102: Measured co-polar and cross-polar radiation levels in the *H*-plane for the HE_{11} mode of port 2 of the broadside array antenna at *4.2GHz*.

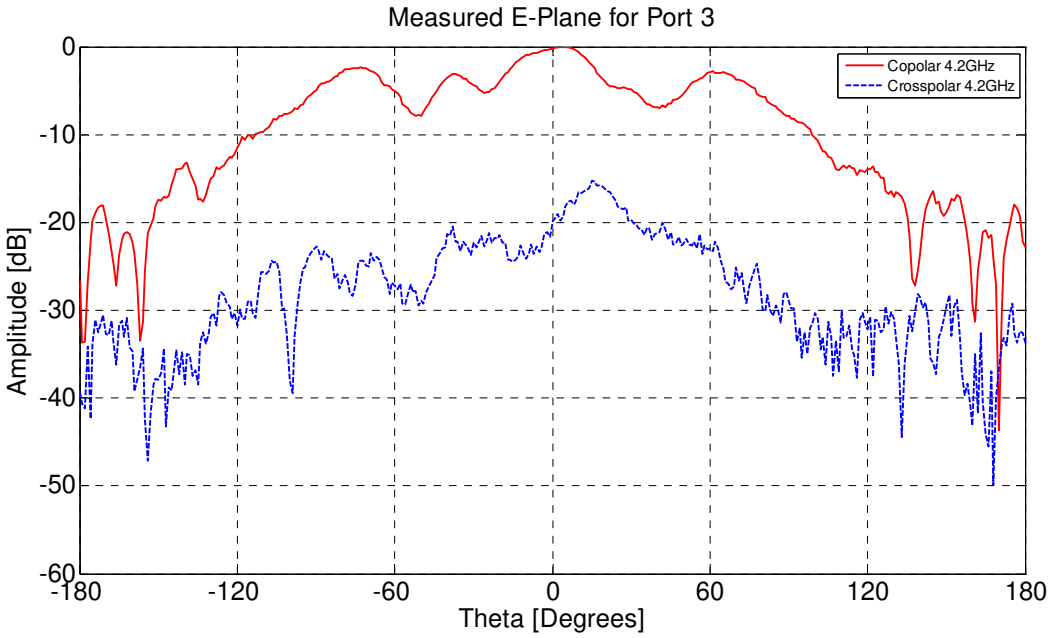

Figure 103: Measured co-polar and cross-polar radiation levels in the *E*-plane for the HE_{11} mode of port 3 of the broadside array antenna at *4.2GHz*.

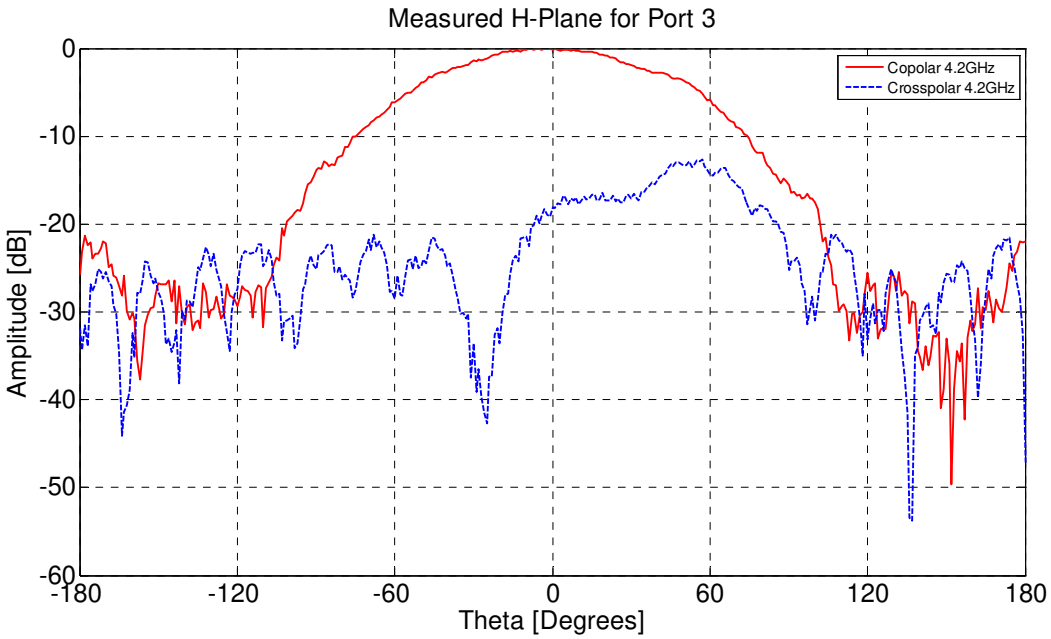

Figure 104: Measured co-polar and cross-polar radiation levels in the *H*-plane for the HE_{11} mode of port 3 of the broadside array antenna at *4.2GHz*.

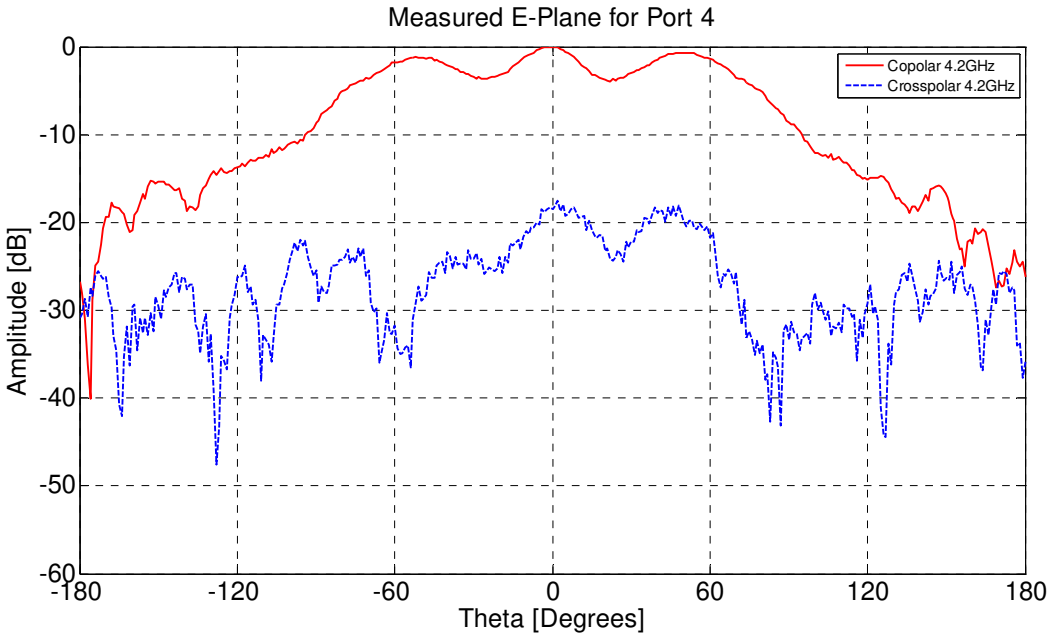

Figure 105: Measured co-polar and cross-polar radiation levels in the *E*-plane for the HE_{11} mode of port 4 of the broadside array antenna at *4.2GHz*.

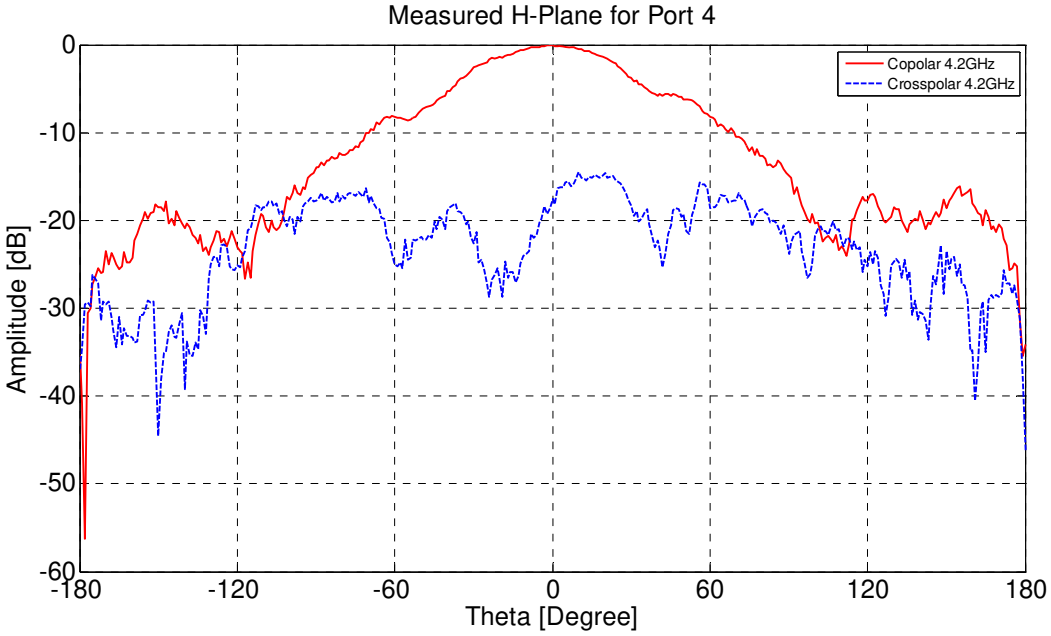

Figure 106: Measured co-polar and cross-polar radiation levels in the *H*-plane for the HE_{11} mode of port 4 of the broadside array antenna at *4.2GHz*.

4.3 Efficiency and Gain

In Table 4.1, the simulated radiation efficiencies and peak gains simualted in Ansoft HFSS for the different modes are shown. The values are calculated mean values over the operating frequency intervals, *2.4-2.7GHz* for the omni-directional antenna and *3.8-4.2GHz* for the broadside radiating antennas.

Antenna/Polarization	*Mean radiation efficiency*	*Mean peak gain*
Omni-directional with airgaps/TE	83.9%	1.57 dB
Omni-directional with airgaps/TM	98.6%	4.35 dB
Omni-directional /TE	83.9%	2.51 dB
Omni-directional /TM	98.4%	4.70 dB
Broadside single element 6mm/port1	98.4%	4.70 dB
Broadside single element 6mm/port2	98.4%	4.70 dB
Broadside 4x1 array/Odd ports	99.1%	13.18 dB
Broadside 4x1 array/Even ports	100.8%	11.39 dB

Table 4.1: Simulated efficiency and peak gain (directivity) of the antennas.

In Table 4.2, the measured radiation efficiency for different modes is shown. The values are calculated over the operating frequency intervals, *2.4-2.7GHz* for the omni-directional antenna and *3.8-4.2GHz* for the single element broadside radiating antenna.

Antenna/Polarization	*Radiated efficiency*
Omni-directional/TE	-0.2895 dB
Omni-directional/TM	0.2238 dB
Broadside single element 6mm/port1	0.1880 dB
Broadside single element 6mm/port2	0.2206 dB

Table 4.2: Measured radiated efficiency of the antennas.

The efficiency of the omni directional antenna is shown below in figure 107. The TE_{01} mode efficiency is low approximately 50% because of the losses due to the microstrip line. Where the efficiency of the TM_{01} mode is above 95% and it is high because there are no ohmic losses as it is in TE_{01} mode. The rapid variation from the smooth curves gives an idea of the errors in the measurement. The ripples occur in the radiated efficiency with respect to the frequency could be because of the multipath interference. There is always a chance of *1dB* error in the measurement and that could be the reason that the efficiency is a little above *100%.*

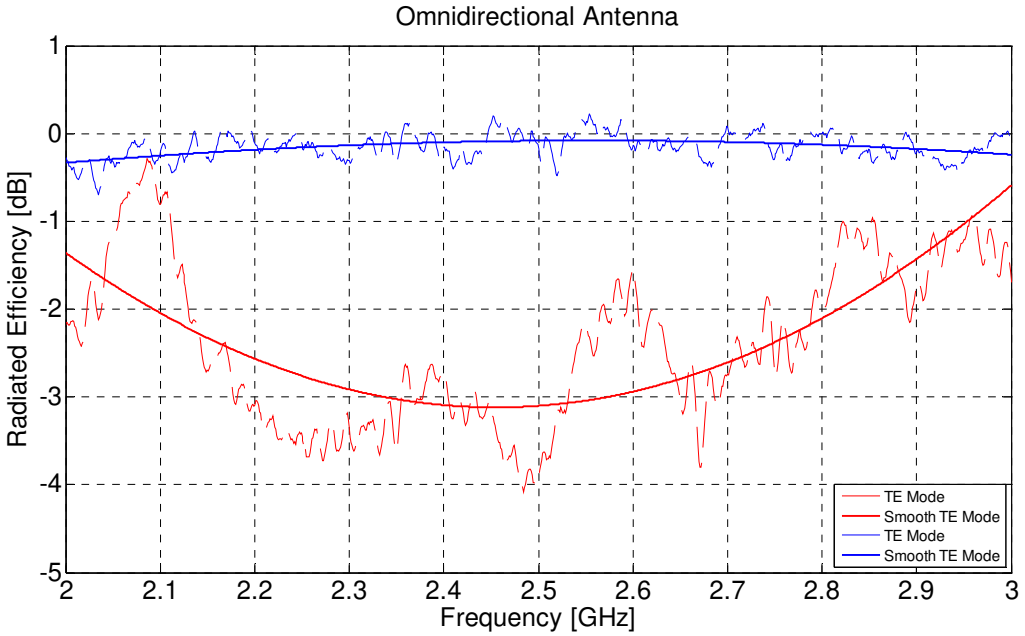

Figure 107: Measured radiated efficiency of Omni-directional Antenna. The *TE* mode has bad efficiency compare to the *TM* mode because of the losses in microstrip. The rapid variation from the smooth curves gives an idea of the errors in the measurements.

The efficiency of the single element for 4x1 array antenna is shown above in figure 108. The efficiency of the HE_{11} mode is above 90%. The rapid variation from the smooth curves gives an idea of the errors in the measurement. The ripples occur in the radiated efficiency with respect to the frequency could be because of the multipath interference.

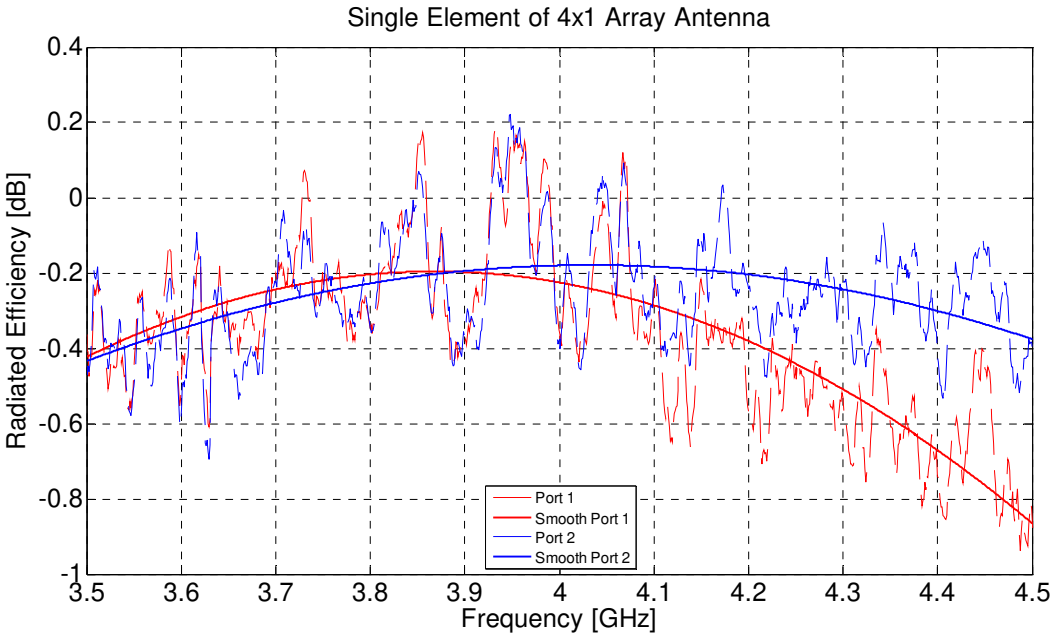

Figure 108: Measure radiated efficiency of Single Element for broadside array Antenna. The rapid variation from the smooth curves gives an idea of the errors in the measurements.

CHAPTER 5

SUMMARY

The characteristics of the manufactured Omni-directional and broadside 4x1 array antennas are shown in Tables 5.1 and 5.2, respectively. The properties that could not be measured are shown as simulated values.

Parameter	***Requirement***
10dB Bandwidth	1000 MHz (TM) N/A (TE)
Antenna port isolation	> 20 dB (2.4-2.7)
Cross Polarization	> 15 dB
Efficiency Simulated	>80% (TE) >98% (TM)
Polarization	Dual Polarized

Table 5.1: Characteristics of the Omni-directional antenna.

Parameter	***Requirement***
10db Bandwidth	450 MHz (HE)
Antenna port isolation	> 15 dB
Cross Polarization	> 20 dB
Efficiency Simulated	>99%
3dB Beamwidth	36 degrees (Even ports) 24 degrees (Odd ports).
Polarization	Dual Polarized
Peak Gain	12.5-13.5 dB (odd) 10.8-12.1 dB (even)

Table 5.2: Characteristics of the broadside 4x1 array antenna.

5.1 Omni-directional Antenna

From the measurements of the scattering parameters, it is seen that for the omni-directional antenna, the return loss resonances appear at *2.45GHz* and *2.4-3.4GHz* (10dB return loss) for the TE_{01} and TM_{01} modes, respectively. The TM_{01} mode is excited by a coaxial probe which is wideband and has a radiation pattern like a dipole antenna as expected.

The coupling to the TE_{01} mode is, in terms of return loss could not be achieved. If however, the antenna is modified so that the microstrip feed touches the resonator bottom, thus coupling is improved. However, the source of error in this excitation is assumed to be the matching network.

The measurements of the *E*-plane of the TE_{01} mode in the omni-directional antenna shows azimuth (horizontal) components on the same level as the cross polar components (vertical). The radiation pattern might be correct, but measurements further up from the ground plane level, at an elevation angle of *45 degrees* (see the simulated gain plots in Results), might be more accurate since the antenna is placed where the co-polar component is the strongest. This conical measurement of the azimuthal field component is thus recommended for this mode. A source of error in this case is nevertheless the unsymmetrical feeding from a microstrip. Perhaps the far field radiation pattern is not azimuthally symmetrical, something that needs further measurements for confirmation.

Another source of error for the omni-directional antenna is the disc surrounding the center probe. This can radiate like the TM_{01} mode and might have a resonance that disturbs the TE_{01} mode. A symmetrical feeding to the TE_{01} mode will improve the antenna radiation symmetry and reduce the coupling between the modes.

5.2 Broadside Antennas

Regarding the broadside single antenna, the *E*-plane radiation pattern for both ports have ripples at elevation angle of 8-16 degrees. This is due to the edges of the ground plane. The edge is *210mm*, which is for the center wavelength of *75mm* gives a null for an elevation angle of *10 degrees*.

The same can be said for the *E*-plane radiation pattern for even ports of the broadside array. The length of the ground plane in this plane is *175.4mm* which for the same calculations as above gives a null around *12 degrees*. In the case with the array, there is also a null from waves belonging to two elements with another element in between, e.g. for elements 1 and 3. This null appears at an elevation angle of *21 degrees* for the center wavelength in the *E*-plane of the odd ports, i.e. at the azimuth cut of φ=0 degrees (parallel to the array axis).

For the broadside antennas, measurements of scattering parameters of the resonator elements with the original height of *7.5mm* showed a too low resonant frequency centered around *3.75GHz*.

This height was modified by using a thinner top sheet on the resonator, thus reducing the height to *6mm*. The resulting resonances then came around *4.1GHz*, which can be expected since the size of the resonating wave is decreased. It was this size that was used in the radiation pattern measurements, see the Results.

The isolation levels of the array antenna are higher than *14dB* in the frequency band of interest (*3.8GHz* to *4.2GHz*). The probe length is critical. A long probe inserted in the resonator gives better coupling to the own mode, but also to the other probe. The length is thus a trade-off. The position of the probe is for mode purity good to have far out on the edge in order not to excite the TM_{01} mode. In this design the probes where *90 degrees* offset with respect to each other, but a larger distance would decrease the cross coupling. The cross polarization levels would increase, however. A symmetrical feeding will improve the antenna radiation symmetry and reduce the coupling between the modes.

As can be seen in Table 4.1, the simulated efficiency of the array antenna can exceed 100%. This puts the validity of the other simulated efficiency values in question and requires verification by measurements. In measurement of the efficiency the array antenna was exceeding 100% but that could be the uncertainty in the anechoic chamber as shown in Table 4.2.

The conclusion for both the omni-directional antenna and the broadside antenna simulations is that the simulations bring one close to the result, but there is an error in the solution. Perhaps in this project, the extensive use of dielectric materials made the error bigger than what e.g. the use of metallic materials would give. If there is access to the materials and the proper machinery for changing the shapes, a couple of iterations could be needed in the practical realization. But the main purpose of this work is achieved as it has been demonstrated that the dielectric resonator is possible candidate for the base station antenna applications.

Regarding the machining of materials, it can be said that the dielectric material did not imply problems when machined. The material is soft and, as was seen, it can be drilled on the exact tangent edge of the circular cross section. If the proper machinery is used in this drilling process, it is not a problem to stack several drilled cylinders on top of each other with perfect overlapping of holes. Also, the material is not visibly torn by the insertion of probes. These properties may not be valid for the harder ceramic materials of higher permittivity.

CHAPTER 6

DISCUSSION

6.1 Narrowband Omni-directional TE_{01} mode

The Omni-directional radiation pattern requires a mode that is symmetrical in the azimuth planes, i.e. the mode needs to be azimuthally invariant. The only modes with this symmetry property are the TE_{0x} and TM_{0x} modes, where x denotes an arbitrary (low) integer. In this project the modes used are the two lowest transverse modes. It has been seen that the TE_{01} mode is narrowband and it has traditionally been used as a filtering mode in microwave circuit components [12]. With a certain implementation of matching this mode can be narrower and thus serve as the filtering mode in integrated antenna-filter resonators. If the desired far field radiation is a broadside beam, a possible implementation could be to use the TE_{01} mode with a resonant frequency below the signal frequency for filtering, modulation and etcetera.

If however, a dual polarized Omni-directional antenna is desired, an improvement of the TE_{01} mode bandwidth needs to be done. If size is not critical, the permittivity could be decreased, since the bandwidth is inversely proportional to the permittivity. Higher bandwidth could also be accomplished by the implementation of a more sophisticated matching network over a whole frequency band, see Figure 109.

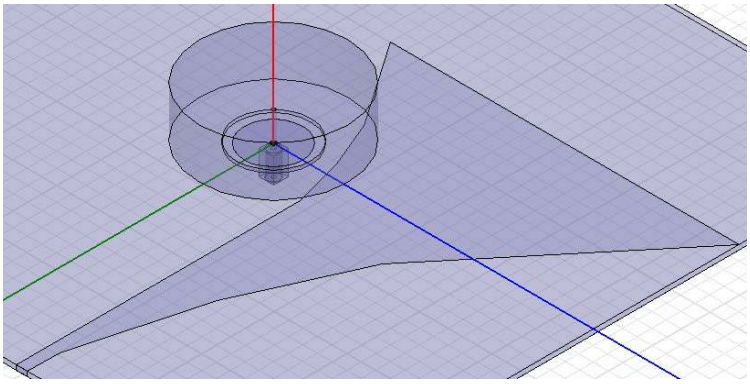

Figure 109: An early attempt to match the resonator by a microstrip was made with a continuous change of the characteristic impedance of the microstrip since the input impedance at the substrate edge showed a low resistive part in the Smith Chart. Some matching network valid over a frequency band would most likely improve the coupling to the TE_{01} mode and thereby the bandwidth as well.

The other polarization is realized by the use of the sufficiently wideband TM_{01} mode which easily can have a *-10dB* return loss bandwidth of *1000MHz*. An alternative to the TE_{01} mode could perhaps be some TE_{0x} mode if these modes have higher bandwidths. In the literature, practical methods for exciting the TE_{02} mode with high mode purity in waveguides do exist [32].

An attempt to excite the TE_{02} mode in a Rogers dielectric resonator of permittivity *10.2* has been made with Ansoft HFSS. The mode is for a cylindrical resonator of radius *24.6mm* and height *12mm* predicted to be at *4.61GHz*. In Figure 110, the field distribution in the resonator at this frequency is illustrated.

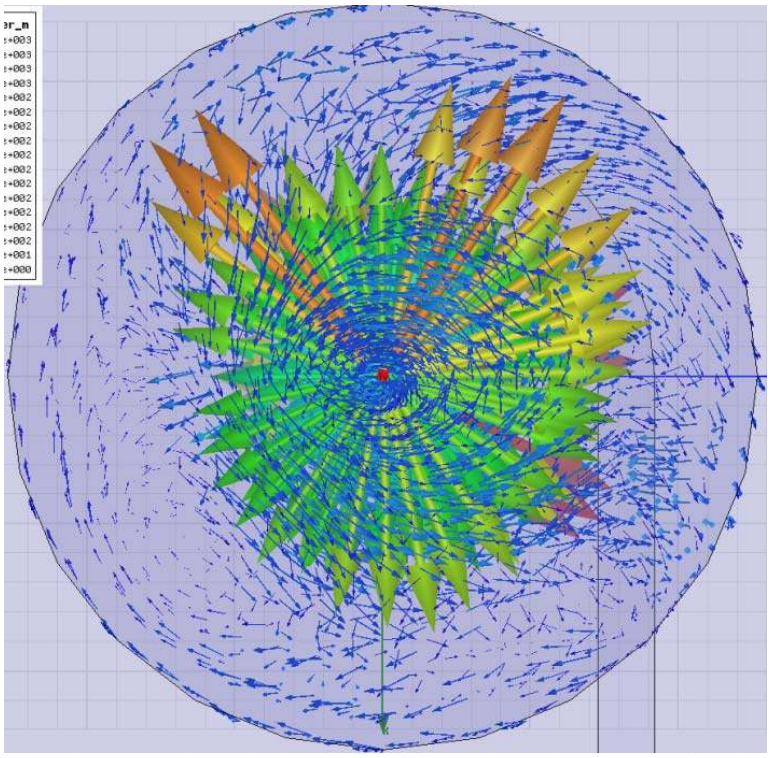

Figure 110: The TE_{02} mode excited by a microstrip line in a cylindrical dielectric resonator of radius *24.6mm* and height *12mm* at around *4.5GHz*.

The reason why the TE_{01} mode and *TE* modes in general have a smaller bandwidth than the *TM* modes has to do with the boundary conditions between a dielectric and metallic surface.

The boundary condition states that the tangential component of the electric field is continuous over a boundary surface. Since the electric field in the conducting ground plane is zero, the electric field is normal to the ground plane. For a *TM* field distribution this is the case. For a TE field distribution, the resonance in the resonator implies a field distribution tangential to the boundary surface and the boundary conditions have to fight the resonance. The point is now that an electric field normal to the ground plane has a tangential magnetic field which is proportional to the surface currents on the ground plane. The *TM* modes have stronger tangential magnetic fields, while the TE modes have to overcome a resonance in the resonator in order to have tangential magnetic fields. The surface currents also radiate and contribute to the bandwidth of the whole structure. The ground plane simply contributes more for *TM* modes; it is not only the resonator that creates the radiation. The phenomenon is illustrated in Figures 111 and 112. For the *TM* modes and the HE_{11} mode, the substrate could be omitted, especially since it is not used for any feeding structure.

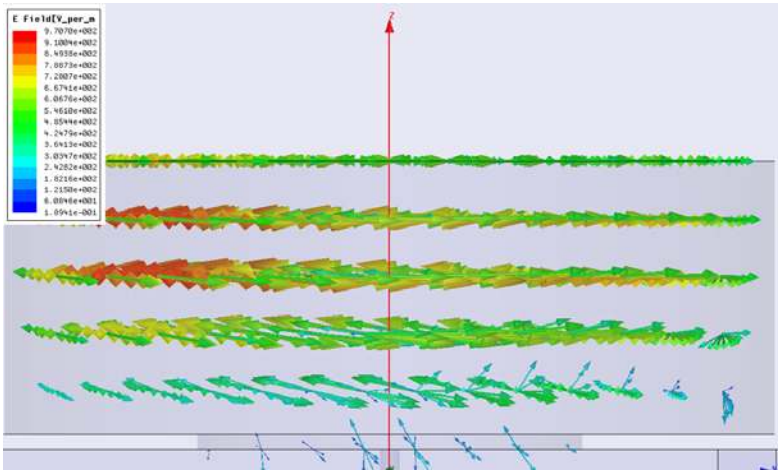

Figure 111: Electric field distribution for the TE_{01} mode in a double-cylinder dielectric resonator above a substrate and a ground plane. It is in the substrate that the field builds up its component normal to the metallic boundary surface without fighting the resonance.

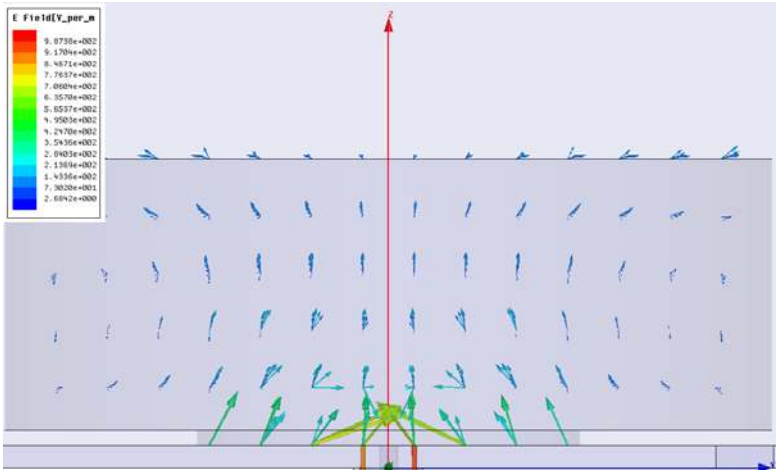

Figure 112: Magnetic field distribution for the TM_{01} mode in a double-cylinder dielectric resonator above a substrate and a ground plane. There is no conflict between resonance and boundary condition on the bottom end of the resonator and the whole field component

As has been seen in the method, the use of very low aspect ratio may contain simultaneous resonance for a cylinder for the TE_{01} and TM_{01} modes. The permittivity may need to be high since the radii become large.

6.2 Alternative shapes

An alternative way of achieving a wideband Omni-directional radiation pattern with the TE_{01} mode is to use the split-cylinder dielectric structure shown in Figure 113.

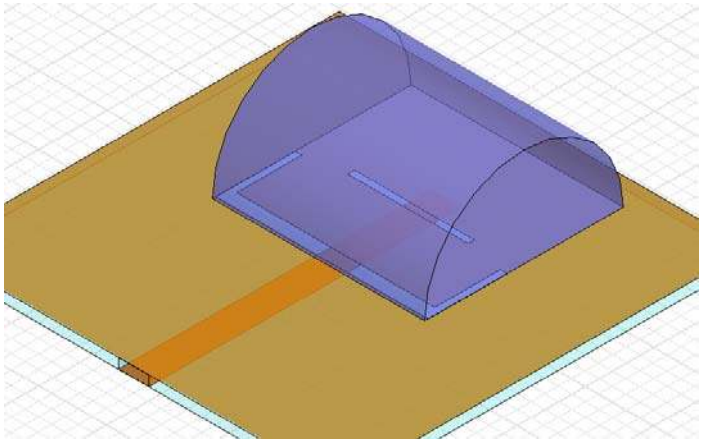

Figure 113: A split-cylinder dielectric resonator on a ground plane excited by slots that are fed from a microstrip [26].

This structure is excited by narrow slots on a ground plane. The possibilities to position the slots and shape them give many opportunities to tune the impedance matching. Also, since the slot radiates like a magnetic dipole, the bandwidth can be extended by making the slot resonance be close to the TE_{01} resonance, which also radiates like a magnetic dipole. In this way, several dips can appear in the reflection coefficient curve [26]. Since there is a ground plane, the split-cylinder is, due to image theory, a whole cylinder in terms of shape, size and field distributions. If an electric current can be led near the longitudinal axis, so that the TM_{01} mode is excited, a dual polarization can be accomplished. In [26], for a relative permittivity of *10.2*, a diameter of *15mm* and a height of *15mm*, the magnetic dipole radiation pattern is for *5-6GHz*.

6.3 Consistency between Simulated and Measured Performance

The simulations of the Omni-directional antenna are quite unstable in the sense that a small change of the geometry, especially the micro stripline, gives significant change of the solution in terms of return loss. If simulations are ran with airgaps between the layers of resonator material in the resonator mushroom cylinder, the reflection coefficient is larger by *2-3dB* for airgaps around *100μm*. Regarding the airgaps, the same can be said for the broadside radiating resonators. In reality, however, even with simple assembly and approximate lengths of the probes, the measured scattering parameters correspond well with the simulations in terms of coupling. The airgaps between the layers are definitely present, but not ruining the return loss. However the size of the dielectric is not the same in the world of simulations as in reality. In the measurements, the HE_{11} resonance dips came around 3.7GHz instead of 4GHz and the size had to be changed. For the TE_{01} and TM_{01} modes, the resonances were not different from the simulations, but the coupling to the TE_{01} was worse, which is assumed to depend on inconsistencies regarding the matching microstrip network.

6.4 Dielectric Properties

The dielectric loss tangent is what determines the efficiency of this kind of antennas since the metallic surfaces are few. For practical applications such as outdoor mounting, the materials need to guarantee quality requirements such as stable values of the relative permittivity and dielectric loss tangent. The stability should hold for variation in samples and variations in temperature. Figure 114 below shows one such diagram for the permittivity versus temperature variation of a dielectric material from Rogers [18].

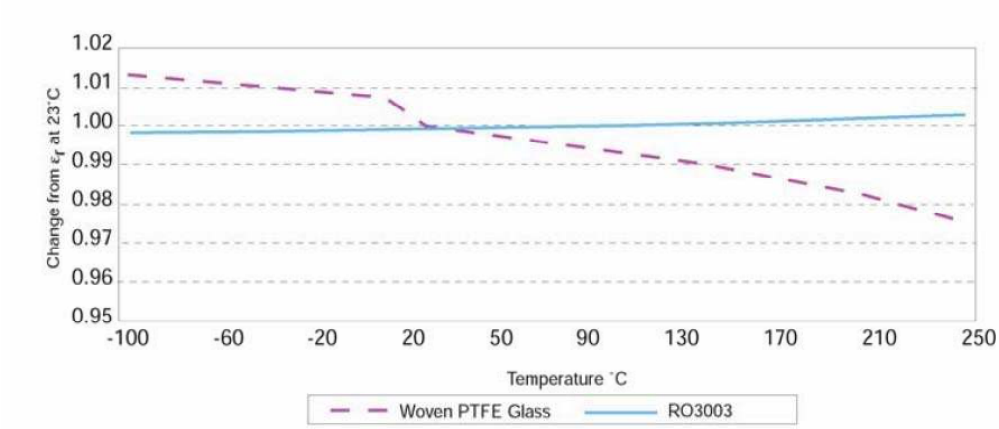

Figure 114: Variation of permittivity as a function of temperature of a Rogers sheet with relative permittivity 3.

REFERENCES

[1] A. Karlsson and G. Kristensson: *compendium Microwave Theory*, Department of Electrical and Information Technology, Faculty of Engineering, LTH, Lund University, Lund, Sweden; October 2009.

[2] R. D. Richtmeyer: *Dielectric Resonators*, Journal of Applied Physics, Vol. 10, pp. 391-398; 1939.

[3] A. A. Kishk and Y. M. M. Antar: *Dielectric Resonator Antennas*, from J. L. Volakis: *Antenna Engineering Handbook*, Chapter 17, 4th ed., McGraw-Hill, USA; 2007.

[4] D.J. Masse, R. A. Purcel, D. W. Ready, E. A. Maguire and C. D. Hartwig: *A New Low Loss High K Temperature Compensated Dielectric for Microwave Applications*, Proceedings IEEE, Vol. 59, pp. 1628-1629; 1971.

[5] J. van Bladel: *On the Resonances of a Dielectric Resonator of Very High Permittivity*, IEEE Transactions on Microwave Theory and Techniques, Vol. MTT-23, pp. 199-208; February 1975.

[6] E. M. O'Connor and S. A. Long: *The History of the Development of the Dielectric Resonator Antenna*, ICEAA International Conference on Electromagnetics in Advanced Applications, Turin, Italy, pp. 872-875; September 17th-21st, 2007.

[7] S. A. Long, M. W. McAllister and L.C. Shen: *The Resonant Cylindrical Dielectric Cavity Antenna*, IEEE Transactions on Antennas and Propagation, Vol. AP-31, pp. 406-412; May 1983.

[8] G. L. Conway, S. A. Long and M. W. McAllister: *Rectangular Dielectric Resonator Antenna*, IET Electronics Letters, Vol. 19, pp. 218-219; March 1983.

[9] S. A. Long and M.W. McAllister: *Resonant Hemispherical Dielectric Antenna*, IET Electronics Letters, Vol. 20, pp. 657-659; August 1984.

[10] M. Haneishi, H. Takazawa, and T. Aoki: *Planar Array Composed of Dielectric Resonator Antennas*, Transactions of the Institute of Electronics and Communication Engineers of Japan, Vol. J67B, pp. 1486-1487; December 1984.

[11] A. Petosa: *Dielectric Resonator Antenna Handbook*, Artech House, Norwood, Massachusetts, USA; 2007.

[12] L. K. Hady, D. Kajfez and A. A. Kishk: *Triple Mode Use of a Single Dielectric Resonator*, IEEE Transactions on Antennas and Propagation, Vol. 57, pp. 1325-1335; May 2009.

[13] M. T. Sebastian: *Dielectric Materials for Wireless Communication*, Elsevier, United Kingdom; 2008.

[14] G. Kristensson: *Spridningsteori*, Department of Electrical and Information Technology, Faculty of Engineering, LTH, Lund University, Lund, Sweden; 2008.

[15] Z. Peng, H. Wang and X. Yao: *Dielectric Resonator Antennas using High Permittivity Ceramics*, Ceramics International, Vol. 30, No. 7, pp. 1211-1214; 2004.

[16] Trans Tech Incorporated. *Dielectric Materials Overview*. http://www.trans-techinc.com/products_detail.asp?ID=2 (accessed September 2010).

[17] Cumming Microwave. *Dielectric Materials Overview*. http://www.cumingmw.com/Product%20Applications/dielectric_materials.html (accessed June 2010).

[18] Rogers Corporation. *Product Overview*. http://www.rogerscorp.com/pages/overview/products.aspx (accessed September 2010).

[19] D. Kajfez and A. A. Kishk: *Dielectric Resonator Antenna – Possible Candidate for Adaptive Antenna Arrays,* Department of Electrical Engineering, University of Mississippi, Oxford, Mississippi, USA.

[20] A. A. Kishk: *Body of Revolution (BOR) Analysis of Cylindrical Dielectric Resonator Antenna,* from K.W. Leung and K. M. Luk: *Dielectric Resonator Antennas*, Chapter 4, Research Published Press Ltd, United Kingdom; 2002.

[21] D. M. Pozar: *Microwave Engineering*, 2nd Edition, John Wiley & Sons, USA; 1998.

[22] A. W. Glisson, G. P. Junker and A. A. Kishk: *Bandwidth Enhancement for Split Cylindrical Dielectric Resonator Antennas*, Progress in Electromagnetic Research PIER, Vol. 33, pp. 97-118; 2001.

[23] D. Kajfez: *FOAM*© software, provided by A. A. Kishk, guest professor at Chalmers University during the spring of 2010; 1986.

[24] T. Itoh and R. Rudokas: *New Method for Computing the Resonant Frequencies of Dielectric Resonators*, 6th European Microwave Conference EuMC, Rome, Italy, pp. 702-706; September 14th-17th 1976.

[25] P. Guillon and D. Kajfez: *Dielectric Resonators*, 2nd ed., Noble Publishing Corp., Atlanta, Georgia, USA; 1998.

[26] A. Abumazwed, O. Ahmed and A. R. Sebak: *Broadband Half-Cylindrical DRA for Future WLAN Applications*, 3rd European Conference on Antennas and Propagation, EuCAP, pp. 389-392; 2009.

[27] J. D. Kraus and R. J. Marhefka: *Antennas For All Applications*, 3rd ed., McGraw-Hill higher education, New York, New York, USA; 2002.

[28] L. K. Hady, D. Kajfez and A. A. Kishk: *Dual Function of a Dielectric Resonator: a High-Q Resonator and a Low-Q Radiator,* Microwave Symposium Digest, IEEE MTT-S International, pp. 1011-1014; June 2008.

[29] Siemens Discrete & RF Semiconductors: *Simple Microstrip Matching for all impedances*, Siemens AG München; © 1996.

[30] Department of Physics and Astronomy - University of Hawaii: *Polarization*, chapter from Military Handbook, Manoa, Hawaii, USA. http://www.phys.hawaii.edu/~anita/web/paperwork/currently%20organizing/Military%20EW%20%20Handbook%20Excerpt/polariza.pdf (accessed September 2010).

[31] P.-S. Kildal and K. Rosengren, "*Correlation and capacity of MIMO systems and mutual coupling, radiation efficiency and diversity gain of their antennas: Simulations and measurements in reverberation chamber*", IEEE Communications Magazine, vol. 42, no. 12, pp. 102-112, Dec. 2004.

[32] T.S. Bigelow, T. L. White and H. D. Kimrey: *Pure Mode Swept Frequency TE_{02} Measurement in 6.35cm Circular Waveguide*, CONF-8511131—2; December 1986

[33] *Formelsamling i fysik*, Institutionen för teorerisk fysik, KTH, Stockholm, Sweden; 2006.

[34] E.W. Weisstein: *Bessel Function Zeros*, from MathWorld – A Wolfram Web Resource. http://mathworld.wolfram.com/BesselFunctionZeros.html (accessed September 2010).

APPENDIX

Appendix A

Bessel Functions

The Bessel functions of the first kind are the solutions to the differential equation

$$\frac{d^2u}{dz^2} + \frac{1}{z}\frac{du}{dz} + \left(1 - \frac{v^2}{z^2}\right) = 0 \text{(A.1)}$$

They are given by

$$J_v(z) = \left(\frac{z}{2}\right)^v \sum_{m=0}^{\infty} \frac{(-1)^m}{m!\Gamma(v+m+1)} \left(\frac{z}{2}\right)^{2m} \text{(A.2)}$$

Where *v* and *z* can be complex valued. If *v* is an integer, then

$$J_{-n}(z) = (-1)^n J_n(z) \text{(A.3)}$$

A plot of the first three orders Bessel functions is in Figure A.1 below.

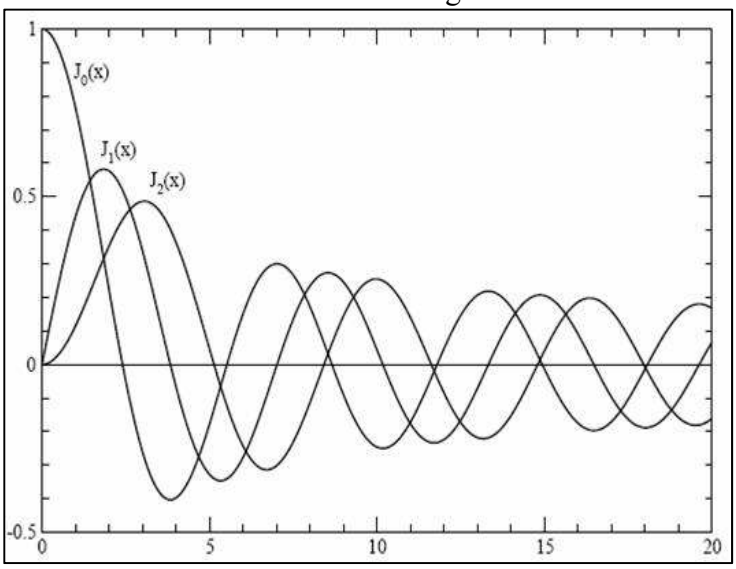

Figure A1: The three lowest orders of Bessel functions of the first kind for values on the positive real axis. The picture is from [33].

In Figure A.2, the Bessel functions of the lowest orders are plotted over the negative real axis:

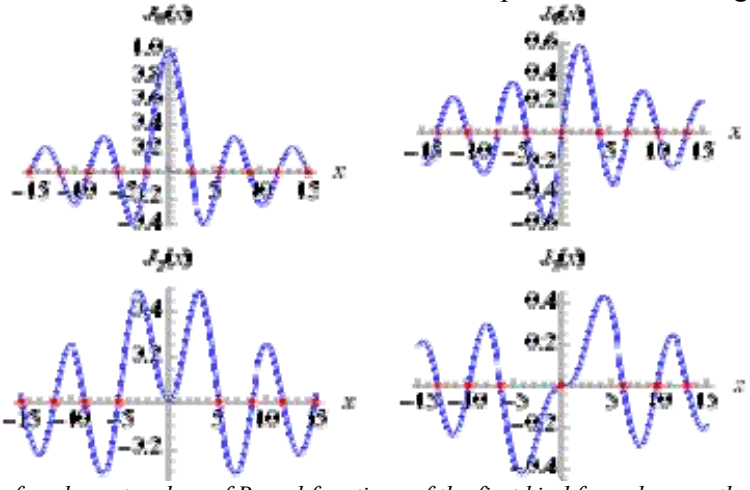

Figure A2: The four lowest orders of Bessel functions of the first kind for values on the real axis [34].

In Tables A.1 and A.2 are the lowest zeros of the lowest Bessel functions and their derivatives, respectively. These are frequently used for determining the *TM* and *TE* mode characteristics respectively in waveguides and resonance cavities.

k	$J_o(x)$	$J_1(x)$	$J_2(x)$	$J_3(x)$	$J_4(x)$	$J_5(x)$
1	2.4048	3.8317	5.1356	6.3802	7.5883	8.7715
2	5.5201	7.0156	8.4172	9.7610	11.0647	12.3386
3	8.6537	10.1735	11.6198	13.0152	14.3725	15.7002
4	11.7915	13.3237	14.7960	16.2235	17.6160	18.9801
5	14.9309	16.4706	17.9598	19.4094	20.8269	22.2178

Table A1: The five lowest zeros of the six lowest Bessel functions of the first kind. Table taken from [34].

k	$J_o(x)$	$J_1(x)$	$J_2(x)$	$J_3(x)$	$J_4(x)$	$J_5(x)$
1	3.8317	1.8412	3.0542	4.2012	5.3175	6.4156
2	7.0156	5.3314	6.7061	8.0152	9.2824	10.5199
3	10.1735	8.5363	9.9695	11.3459	12.6819	13.9872
4	13.3237	11.7060	13.1704	14.5858	15.9641	17.3128
5	16.4706	14.8636	16.3475	17.7887	19.1960	20.5755

Table A2: The five lowest zeros of the derivatives of the six lowest Bessel functions of the first kind. Table taken from [34].

Appendix B

Tables of Simulated Efficiency and Peak gain over the Frequency Bands

OMNIDIRECTIONAL ANTENNA with 100μm airgaps.

TE mode Frequency [GHz]	Radiation Efficiency [%]	Peak gain [dB]
2.4	88.9	2.4606
2.5	87.5	2.1394
2.6	80.6	1.0384
2.7	78.7	0.6258

Table B.1: Simulated radiation efficiency in Ansoft HFSS for the omnidirectional antenna with consideration of airgaps between the cylinder sheets of thickness 1mm and 2.5mm, respectively. The assumed airgap thickness is 100μm. The polarization considered is the TE_{01} mode (microstrip).

OMNIDIRECTIONAL ANTENNA with 100μm airgaps.

TM mode Frequency [GHz]	Radiation Efficiency [%]	Peak gain [dB]
2.4	98.3	3.8434
2.5	98.5	4.2496
2.6	98.7	4.5443
2.7	98.8	4.7744

Table B.2: Simulated radiation efficiency in Ansoft HFSS for the omnidirectional antenna with consideration of airgaps between the cylinder sheets of thickness 1mm and 2.5mm, respectively. The assumed airgap thickness is 100μm. The polarization considered is the TM_{01} mode (coaxial probe).

OMNIDIRECTIONAL ANTENNA solid cylinder

TE mode Frequency [GHz]	Radiation Efficiency [%]	Peak gain [dB]
2.4	87.9	3.3832
2.5	87.4	3.1338
2.6	80.3	2.1437
2.7	80.1	1.3634

Table B.3: Simulated radiation efficiency in Ansoft HFSS for the omnidirectional antenna without consideration of airgaps between the cylinder sheets of thickness 1mm and 2.5mm, respectively. The polarization considered is the TE_{01} mode (microstrip).

OMNIDIRECTIONAL ANTENNA solid cylinder

TM mode Frequency [GHz]	Radiation Efficiency [%]	Peak gain [dB]
2.4	98.3	4.2050
2.5	98.4	4.6154
2.6	98.5	4.8871
2.7	98.5	5.0637

Table B.4: Simulated radiation efficiency in Ansoft HFSS for the omnidirectional antenna without consideration of airgaps between the cylinder sheets of thickness 1mm and 2.5mm, respectively. The polarization considered is the TM_{01} mode (coaxial probe).

SINGLE ELEMENT BROADSIDE ANTENNA solid cylinder

HE mode port-1 Frequency [GHz]	Radiation Efficiency [%]	Peak gain [dB]
3.8	93	9.4622
3.9	94.9	9.3086
4.0	98.9	9.2919
4.1	99.99	9.2430
4.2	101	9.8409

Table B.5: Simulated radiation efficiency in Ansoft HFSS for the broadside single element antenna without consideration of airgaps between the cylinder sheets of 2.5mm thickness. The polarization considered is the HE_{11} mode (probe 1) along the x-axis (see above).

SINGLE ELEMENT BROADSIDE ANTENNA solid cylinder

HE mode port2 Frequency [GHz]	Radiation Efficiency [%]	Peak gain [dB]
3.8	93	9.4622
3.9	94.9	9.3086
4.0	98.9	9.2919
4.1	99.99	9.2430
4.2	101	9.8409

Table B.6. Simulated radiation efficiency in Ansoft HFSS for the broadside single element antenna without consideration of airgaps between the cylinder sheets of 2.5mm thickness. The polarization considered is the HE_{11} mode (probe 2) along the y-axis (see above).

BROADSIDE 4x1 ARRAY ANTENNA solid cylinders

HE mode Odd Ports Frequency [GHz]	Radiation Efficiency [%]	Peak gain [dB]
3.8	98.3	12.5840
3.9	99.2	12.9350
4.0	99.6	13.2168
4.1	99.5	13.6133
4.2	99.1	13.5470

Table B.7: Simulated radiation efficiency in Ansoft HFSS for the broadside array antenna without consideration of airgaps between the cylinder sheets of 2.5mm thickness. The polarization considered is the HE_{11} mode (odd ports along the y-axis, see above).

BROADSIDE 4x1 ARRAY ANTENNA solid cylinders

HE mode Even Ports Frequency [GHz]	Radiation Efficiency [%]	Peak gain [dB]
3.8	100.1	10.7751
3.9	100.7	11.0326
4.0	101.0	11.3558
4.1	101.2	11.7167
4.2	101.1	12.1010

Table B.8: Simulated radiation efficiency in Ansoft HFSS for the broadside array antenna without consideration of airgaps between the cylinder sheets of 2.5mm thickness. The polarization considered is the HE_{11} mode (even ports along the y-axis, see above).

Appendix C

MATLAB codes

```
%% Prediction of the resonant frequency of the DRA from FOAM©
close all;
clear all,
clc;

%% Read Data

TE6 = [10.343 9.580 8.972 8.471 8.055 7.699 7.394 7.130 6.894 6.687 6.503
6.340 6.189 6.051 5.925 5.811 5.708 5.613 5.526 5.446 5.370 5.294 5.224]';
TM6 = [15.323 14.166 13.157 12.287 11.540 10.899 10.348 9.873 9.461 9.102
8.787 8.511 8.267 8.051 7.857 7.684 7.529 7.389 7.263 7.148 7.042 6.946
6.858]';
TE10 = [8.031 7.439 6.967 6.578 6.255 5.978 5.742 5.536 5.363 5.192 5.050
4.923 4.806 4.698 4.601 4.513 4.432 4.358 4.291 4.228 4.170 4.111 4.057]';
TM10 = [11.898 11 10.216 9.541 8.961 8.463 8.035 7.666 7.346 7.067 6.823 6.609
6.419 6.251 6.101 5.967 5.846 5.738 5.640 5.551 5.468 5.394 5.325]';
TE20 = [5.736 5.312 4.975 4.697 4.467 4.269 4.100 3.954 3.823 3.708 3.606
3.516 3.432 3.355 3.286 3.223 3.165 3.112 3.064 3.020 2.978 2.936 2.897]';
TM20 = [8.497 7.855 7.296 6.813 6.399 6.044 5.738 5.475 5.246 5.047 4.873
4.720 4.584 4.464 4.357 4.261 4.175 4.097 4.028 3.964 3.905 3.852 3.803]';
TE25 = [5.130 4.752 4.450 4.201 3.995 3.818 3.667 3.536 3.419 3.317 3.226
3.145 3.070 3.001 2.939 2.882 2.831 2.784 2.741 2.701 2.663 2.626 2.591]';
TM25 = [7.600 7.026 6.526 6.094 5.724 5.406 5.133 4.897 4.692 4.514 4.358
4.221 4.100 3.993 3.897 3.811 3.734 3.665 3.602 3.545 3.493 3.445 3.401]';
TE30 = [4.683 4.338 4.062 3.835 3.647 3.486 3.348 3.228 3.121 3.028 2.945
2.871 2.802 2.740 2.683 2.631 2.584 2.541 2.502 2.466 2.431 2.397 2.365]';
TM30 = [6.938 6.414 5.957 5.563 5.225 4.935 4.685 4.470 4.283 4.121 3.979
3.854 3.743 3.645 3.557 3.479 3.409 3.346 3.289 3.236 3.189 3.145 3.105]';
TE40 = [4.056 3.756 3.518 3.322 3.159 3.019 2.899 2.796 2.703 2.622 2.550
2.486 2.427 2.372 2.323 2.279 2.238 2.201 2.167 2.135 2.106 2.076 2.048]';
TM40 = [6.008 5.554 5.159 4.818 4.525 4.274 4.058 3.871 3.710 3.567 3.446
3.337 3.242 3.157 3.081 3.013 2.952 2.897 2.848 2.803 2.761 2.724 2.689]';

H = 3:0.5:14;
%% Figure for Prediction of TE01 mode Resonant Frequency
figure (1);
hold on;
grid on;
plot(H,TE6,'--r*');
plot(H,TE10,'--b');
plot(H,TE20,'-gd');
plot(H,TE25,'-k+');
plot(H,TE30,'c');
plot(H,TE40,'-ms');
set(gca,'fontsize',14);
legend('er=6.15','er=10.2','er=20','er=25','er=30','er=40');
xlabel('Height of the Cylinder [mm]');
ylabel('Resonant Frequency [GHz]');
axis([3 12 2 11]);
set(gca,'fontsize',18);
```

```
title('FOAM Prediction for the TE01 Resonant Frequency of a dielectric
cylinder without Metal Shielding');
%% Figure for Prediction of TE01 mode Resonant Frequency
figure (2);
hold on;
grid on;
plot(H,TM6,'--r*');
plot(H,TM10,'--b');
plot(H,TM20,'-gd');
plot(H,TM25,'-k+');
plot(H,TM30,'c');
plot(H,TM40,'-ms');
set(gca,'fontsize',14);
legend('er=6.15','er=10.2','er=20','er=25','er=30','er=40');
xlabel('Height of the Cylinder [mm]');
ylabel('Resonant Frequency [GHz]');
axis([3 12 2 16]);
set(gca,'fontsize',18);
title('FOAM Prediction for the TM01 Resonant Frequency of a dielectric
cylinder without Metal Shielding');
```

```
%% Q-Factor of TE01 Mode
close all;
clear all;
clc

%% Read Data

x=0.5:0.1:5;
Q=zeros(12,46);
er=[10 15 20 25 30 40 50];

i=6;
Q=0.078192*((er(i))^(1.27))*(1+17.31*(1./x)-
21.57*((1./x).^2)+10.86*((1./x).^3)-1.98*((1./x).^4));
i=5;
R=0.078192*((er(i))^(1.27))*(1+17.31*(1./x)-
21.57*((1./x).^2)+10.86*((1./x).^3)-1.98*((1./x).^4));
i=4;
S=0.078192*((er(i))^(1.27))*(1+17.31*(1./x)-
21.57*((1./x).^2)+10.86*((1./x).^3)-1.98*((1./x).^4));
i=3;
T=0.078192*((er(i))^(1.27))*(1+17.31*(1./x)-
21.57*((1./x).^2)+10.86*((1./x).^3)-1.98*((1./x).^4));
i=2;
U=0.078192*((er(i))^(1.27))*(1+17.31*(1./x)-
21.57*((1./x).^2)+10.86*((1./x).^3)-1.98*((1./x).^4));
i=1;
V=0.078192*((er(i))^(1.27))*(1+17.31*(1./x)-
21.57*((1./x).^2)+10.86*((1./x).^3)-1.98*((1./x).^4));

%% Figure for Q-Factor of the TE01 Mode for Various Permittivies
figure (1);
```

```
hold on;
grid;
plot(x, Q, '--r*');
plot(x, R, '--bd');
plot(x, S, '--g*');
plot(x, T, '-k+');
plot(x, U, 'c');
plot(x, V, '-ms');

set(gca,'fontsize',18);
title('Q-Factor of the TE01 Mode for Various Permittivies');
xlabel('Aspect Ratio (radius/height)');
ylabel('Q-Factor');
legend('er=50','40','30','20','10','5');
```

```
%% For Omni Directional Antenna
%% % % % % % % Kishk Chapter 17 TE, TM and HE Mode equations used for
intersection curves in Method% % % % % % %
close all;
clear all;
clc;

c=299792458;     % Speed of light
er=[6.15 10.2 15 20 25 30 40]; % Permitivity
a=19.22;         % Radius of the cylinder
h=1:0.001:10;    % Height of the cylinder
x=a./(2*h);      % Aspect ratio

fTE01=zeros(7,length(h));
fTM01=zeros(7,length(h));
%% % % % % TE01 Mode % % % % %
for i=1:7
% fTE01(i,:)=(2.921*c*er(i)^(-0.465)/(2*pi*a)*(0.691+0.319.*x-0.035.*x.^2));
QTE01(i,:)=(0.021*er(i)^1.2076*(5.270.*x+1106.188.*x.^0.625.*exp(-
1.0272.*x)));
%% % % % TM01 Mode % % % % %

% fTM01(i,:)=(2.933*c*er(i)^(-0.468)/(2*pi*a))*(1-(0.075-0.05*x)*(er(i)-
10)/28).*(1.048+0.377*x-0.071*x.^2);
QTM01(i,:)=(0.009*er(i)^0.888*exp(0.040*er(i))).*(1-((0.3-0.2.*x).*(38-
er(i))/28)).*(9.498.*x+2058.33.*x.^4.322.*exp(-3.501.*x));
%% % % % HE01 Mode % % % % %

% fHE01=(2.735*c*er(i)^-0.436/(2*pi*a))*(0.543+0.589.*x-0.050.*x.^2);
QHE01=(0.013*er(i)^1.202)*(2.135.*x+228.043.*x.*exp(-2.046.*x+0.111.*x.^2));
end
%% Q-Factor TE01 mode for different Heights and Permitivity
figure(1);
grid;
hold on;

plot(h,QTE01(1,:),'r');
plot(h,QTE01(2,:),'g');
plot(h,QTE01(3,:),'b');
```

```
plot(h,QTE01(4,:),'k');
plot(h,QTE01(5,:),'c');
plot(h,QTE01(6,:),'m');
plot(h,QTE01(7,:),'k');
set(gca,'fontsize',18);
set(gca,'xtick',[1:10]);
xlabel('Height of the cylinder [mm]');
ylabel('Q-Factor');
title('Q-Factor TE01 mode for different heights and permitivity with radius
19.22mm');
legend('er=40','30','25','20','15','10.2','6.15','location','northwest');
%% Q-Factor TM01 mode for different Heights and Permitivity
figure(2);
grid;
hold on;

plot(h,QTM01(1,:),'r');
plot(h,QTM01(2,:),'g');
plot(h,QTM01(3,:),'b');
plot(h,QTM01(4,:),'k');
plot(h,QTM01(5,:),'c');
plot(h,QTM01(6,:),'m');
plot(h,QTM01(7,:),'k--');

set(gca,'fontsize',18);
set(gca,'xtick',[1:10]);
xlabel('Height of the cylinder [mm]');
ylabel('Q-Factor');
title('Q-Factor TM01 mode for different heights and permitivity with radius
19.22mm');
legend('er=40','30','25','20','15','10.2','6.15','location','northwest');
```

```
%% Numerical Formula for calculating the Shape of DRA
%% % % % % Kishk Chapter 17 TE, TM and HE Mode equations % % % % % % %
close all;
clear all;
clc;

%% Read Data

c=299792458000;      % Speed of light
er=[6.15 10.2 20 25 30 40]; % Permitivity
a=13.22;             % Radius of the cylinder
h=7:0.01:14;         % Height of the cylinder
x=a./(2.*h);         % Aspect ratio

fTE01=zeros(length(er), length(h));
QTE01=zeros(length(er), length(h));
fTM01=zeros(length(er), length(h));
QTM01=zeros(length(er), length(h));
fHE11=zeros(length(er), length(h));
QHE11=zeros(length(er), length(h));

for i=1:length(er)
%% % % % % TE01 Mode % % % % %
```

```
fTE01(i,:)=2.921*c*er(i)^(-0.465)/(2*pi*a)*(0.691+0.319.*x-0.035.*x.^2);
QTE01(i,:)=(0.021*er(i)^1.2076*(5.270.*x+1106.188.*x.^0.625.*exp(-
1.0272.*x)));
%% % % % TM01 Mode % % % % %

fTM01(i,:)=(2.933*c*er(i)^(-0.468)/(2*pi*a))*(1-(0.075-0.05*x)*(er(i)-
10)/28).*(1.048+0.377*x-0.071*x.^2);
QTM01(i,:)=(0.009*er(i)^0.888*exp(0.040*er(i))).*(1-((0.3-0.2.*x).*(38-
er(i))/28)).*(9.498.*x+2058.33.*x.^4.322.*exp(-3.501.*x));
%% % % % HE11 Mode % % % % %

fHE11(i,:)=(2.735*c*er(i)^-0.436/(2*pi*a))*(0.543+0.589.*x-0.050.*x.^2);
QHE11(i,:)=(0.013*er(i)^1.202)*(2.135.*x+228.043.*x.*exp(-
2.046.*x+0.111.*x.^2));
%%
end
%% Resonant Frequency from Numerical formula for the TE01 mode
figure(1);
grid;
hold on;

plot(h,fTE01(1,:)./(1e9),'r');
plot(h,fTE01(2,:)./(1e9),'b');
plot(h,fTE01(3,:)./(1e9),'g');
plot(h,fTE01(4,:)./(1e9),'k');
plot(h,fTE01(5,:)./(1e9),'c');
plot(h,fTE01(6,:)./(1e9),'m');

set(gca,'fontsize',18);
title('Resonant Frequency from Numerical formula (2.19) for the TE01 mode for
different Permitivities');
xlabel('Height of the cylinder [mm]');
ylabel('Resonant Frequency [GHz]');
legend('er=6.15','er=10.2','er=20','er=25','er=30','er=40');
%% Resonant Frequency from Numerical formula for the TM01 mode
figure(2);
grid;
hold on;

plot(h,fTM01(1,:)./(1e9),'r');
plot(h,fTM01(2,:)./(1e9),'b');
plot(h,fTM01(3,:)./(1e9),'g');
plot(h,fTM01(4,:)./(1e9),'k');
plot(h,fTM01(5,:)./(1e9),'c');
plot(h,fTM01(6,:)./(1e9),'m');

set(gca,'fontsize',18);
title('Resonant Frequency from Numerical formula (2.21) for the TM01 mode for
different Permitivities');
xlabel('Height of the cylinder [mm]');
ylabel('Resonant Frequency [GHz]');
legend('er=6.15','er=10.2','er=20','er=25','er=30','er=40');
%% Resonant Frequency from Numerical formula for the HE11 mode
figure (3);
grid;
```

```
hold on;

plot(h,fHE11(1,:)./(1e9),'r');
plot(h,fHE11(2,:)./(1e9),'b');
plot(h,fHE11(3,:)./(1e9),'g');
plot(h,fHE11(4,:)./(1e9),'k');
plot(h,fHE11(5,:)./(1e9),'c');
plot(h,fHE11(6,:)./(1e9),'m');

set(gca,'fontsize',18);
title('Resonant Frequency from Numerical formula (2.19) for the HEM11 mode for
different Permitivities');
xlabel('Height of the cylinder [mm]');
ylabel('Resonant Frequency [GHz]');
legend('er=6.15','er=10.2','er=20','er=25','er=30','er=40');
```

```
%%%code for plotting exported gain or radiation curves to xls files from
HFSS%%%%%%%
a=xlsread('GainTotalTE','A2:A362');  %read first column, i.e. angle
gTEfi0=xlsread('GainTotalTE','B2:B362');%read second column, i.e. gain at phi
90
gTEfi90=xlsread('GainTotalTE','C2:C362'); %read third column, i.e. gain at phi
90
gTMfi0=xlsread('GainTotalTM','B2:B362');
gTMfi90=xlsread('GainTotalTE','C2:C362');
gArOddfi0=xlsread('OddExciteTotal','B2:B362');
gArOddfi90=xlsread('OddExciteTotal','C2:C362');
gArEven90=xlsread('evenexciteTotal','C2:C362');
gArEven0=xlsread('evenexciteTotal','B2:B362');

figure(1)
subplot(2,1,1)
set(gca,'fontsize',20)
grid on;

plot(a,gTEfi0,'r');
hold on;
plot(a,gTEfi90,'b');
grid on;
title('Gain for the TE01 mode w.r.t. elevation at azimuth 0 and 90 degrees')
axis([-180 180 0 3]);
set(gca,'xtick',[-180:40:180]);

subplot(2,1,2)
set(gca,'fontsize',20)

plot(a,gTMfi0,'r');
hold on;
plot(a,gTMfi90,'b');
grid on;
title('Gain for the TM01 mode w.r.t. elevation at azimuth 0 and 90 degrees')
axis([-180 180 0 3]);
set(gca,'xtick',[-180:40:180]);
```

```
figure(2)
subplot(2,1,1)
set(gca,'fontsize',20)

plot(a,gArOddfi0,'r');
hold on;
plot(a,gArOddfi90,'b');
grid on;
title('Array Gain for Odd ports mode w.r.t. elevation at azimuth 0 and 90
degrees')
axis([-180 180 0 25]);
set(gca,'xtick',[-180:40:180]);

subplot(2,1,2)
set(gca,'fontsize',20)

plot(a,gArEven0,'r');
hold on;
plot(a,gArEven90,'b');
grid on;
title('Array Gain for Even ports mode w.r.t. elevation at azimuth 0 and 90
degrees')
axis([-180 180 0 20]);
set(gca,'xtick',[-180:40:180]);
```